

© Copyright 2021

Michael Z. McIntire

On the kinematic and dynamic evolution of a magma mush: from liquidus to solidus

Michael Z. McIntire

A dissertation

submitted in partial fulfillment of the
requirements for the degree of

Doctor of Philosophy

University of Washington

2021

Reading Committee:

George Bergantz, Chair

Cailey Condit

Michael Brown

Program Authorized to Offer Degree:

Earth and Space Sciences

University of Washington

Abstract

On the kinematic and dynamic evolution of magma mush: from liquidus to solidus

Michael Z. McIntire

Chair of the Supervisory Committee:
Dr. George Bergantz
Department of Earth and Space Sciences

Magmas are dynamic hydrogranular systems where the interactions between the melt and the residing crystals influences the eruptive behavior of volcanoes, the concentration of economic metals, and the stratification of the Earth's crust. Despite the importance of the interaction between these phases, little is known about the mechanics of these systems. The purpose of this dissertation is to investigate the interactions of the melt and crystals of magma from the formation of the crystal-rich mush to the expulsion of the melt from its interstitial spaces. I first examine the dilute case where suspended crystals are coupled to the fluid. I employed a combination of discrete element computational fluid dynamic (DEM-CFD) numerical simulations, field observations, and electron backscatter diffraction (EBSD) analyses to explore the mechanics of the interactions between the crystals and the melt of magmas. The

formation of crystal clusters was explored using Voronoi tessellations in both a settling only model at a solid volume percent of 9 and an open system models (where a magma like fluid is injected into the accumulating mush) with solid volume percents of 1, 9, and 20. I find that there is statistically no difference in the distribution of clustering between the two systems and that clusters are just as likely as a random distribution. Indicating that abundant crystal clusters found in sampled magmatic systems are likely from a disaggregated magma mush. Next, I examined the crystal-rich state where the formation of granular flows transfer momentum to the resident fluid. I employed a DEM-CFD numerical dam break model of a polydisperse particle column to explore the kinematics of the collapse and runout of the particle column. The column develops two collapse regimes a toppling collapse, and a sliding collapse, which transition into three kinematic runout regimes, gravity current, heap flow, and a quasi-static region. Both a force and contact fabric develop in the heap flow where the particles have enduring contacts. The difference in anisotropy between the normal force and contact fabrics illustrates the non-affine nature of granular material and the issue with applying the concepts of continuum modelling to hydrogranular systems. The first two chapters were based on numerical models analyses to create an idealized framework of knowledge on hydrogranular systems. The final chapter builds on geological observations and fieldwork with a goal of determining the mechanisms of pore space reduction in a crystal-rich magma mush. I collected 12 samples from the mafic complex of Sierra Valle Fértil from which I conducted EBSD analyses to quantify the crystallographic preferred orientation (CPO) and the internal lattice distortions. I considered the evidence for tectonic filter pressing, mechanical compaction, and viscous compaction. The internal lattice distortions have a similar distribution across plagioclase, hornblende, and quartz. This suggests the crystal deformation happened subsolidus and was not caused by either viscous compaction or

tectonic filter pressing, and that a mechanical compaction process was responsible for pore space reduction. Future work should focus on the physics of hydrogranular systems with non-spherical particles employing analogue and numerical models to better capture natural systems.

TABLE OF CONTENTS

List of Figures	ix
List of Tables	xv
Chapter 1. Introduction	1
Chapter 2. On the hydrodynamics of crystal clustering.....	5
2.1 Introduction and background	5
2.1.1 introduction.....	5
2.1.2 Geologic observations and motivations	6
2.1.3 Theoretical overview	6
2.1.4 Objectives of the study.....	11
2.2 Methods.....	11
2.2.1 DEM-CFD simulations of an open-system intrusion into an olivine bearing magma chamber.....	11
2.3 Measures of clustering	14
2.3.1 Bulk clustering measures, R, Ripley’s K(r), L(r), and g(r) functions.....	15
2.3.2 Voronoi tessellation as a measure of clustering.....	23
2.4 Discussion and Conclusions	29
Chapter 3. On the dynamics of magmatic gravity currents	33
3.1 Introduction.....	33
3.2 The ‘dam break’ scenario as a proxy system for magmatic density currents	36
3.2.1 Theory.....	37

3.2.2	Simulation parameters	39
3.2.3	Scaling.....	40
3.3	Micro and mesoscale descriptions of gravity currents.....	42
3.3.1	Force chains and microstructures.....	42
3.3.2	Column collapse and runout	44
3.3.3	Gravity current	46
3.3.4	Plastic flow in the heap	47
3.3.5	Quasi-static regime	48
3.4	Microstructure analysis.....	48
3.4.1	Velocity and Kinetic energy	48
3.4.2	Force and contact anisotropy	50
3.5	Summary	53
Chapter 4. On the expulsion of melt from the interstitial spaces of a magma mush by pore space reduction		
		56
4.1	Introduction.....	56
4.2	Melt extraction features in crystallizing systems.....	58
4.3	Mechanisms of melt extraction from cumulates	61
4.3.1	Shearing of non-spherical particles.....	61
4.3.2	Accumulation and primary fabric formation	62
4.3.3	Filter pressing.....	63
4.3.4	Compaction.....	66
4.3.5	Summary	69
4.4	Geologic setting: the Famatinian magmatic arc.....	70

4.5	Methods.....	74
4.5.1	Electron Backscatter Diffraction (EBSD).....	74
4.5.2	Quantitative evaluation of minerals by scanning electron microscopy (QEMScan)	75
4.6	Petrology.....	75
4.6.1	FA10-03m.....	78
4.6.2	FA18-01a	80
4.6.3	FA18-03	83
4.6.4	Summary	84
4.7	Fabric Quantification	84
4.7.1	FA10-03m.....	85
4.7.2	FA18-01a	87
4.7.3	FA18-03	90
4.8	Discussion.....	93
4.8.1	Crystallization, accumulation, and igneous fabric formation	93
4.8.2	The origin of plastic deformation in the cumulate crystals.....	94
4.8.3	The mechanisms of melt extraction	97
4.9	Conclusion	98
	Bibliography	100

LIST OF FIGURES

- Figure 2.1. Three steps, $\tau=0,0.5,1.1$, from the initially 9% solid volume fraction of olivine open system model (OSM). The top row shows the changes in the temperature of the multiphase system between the initial temperature of 1290° and the temperature of the new intruding basalt of 1340°. The bottom three panels show the particles (olivine crystals) as black points and the background color is the change in MgO wt% between the initial value of 10.76 and the new intruding value of 12.94. Variations between these reflect mixing of the resident and incoming magma. A yellow line is drawn at the shock front that separates the settling particles and the region of the domain that no longer has particles. 15
- Figure 2.2. Three time steps, $\tau=0,0.5,1.1$, from three open system models (OSM) which differ by solid volume per cent. From left to right the solid volume fractions are, 1%, 9% and 20%. The three times correspond to those in text. A yellow line is drawn at the shock front between the settling particles and the region of the domain that no longer has particles in the lower half of figures (b) and (c). The reader is directed to the movie OSM-1.mp4 in the electronic Supplementary material..... 18
- Figure 2.3. R index vs solid volume per cent, ϕ_s . The black line is the Random Sphere Distribution Line (RSDL) from Jerram et al., (1996). The points shown are from $\tau = 0, 0.5$, and 1.1 of the 9% solid volume per cent settling model (SM) and the solid volume per cent of 1%, 9% and 20% open system models (OSM)..... 19
- Figure 2.4. Ripley's L value(a-c) and pair correlation (d-f) functions and for both the open system model (OSM) and settling model (SM) at 9% crystal volume per cent. The results for the OSM and SM were similar for $\tau = 0$ and 0.5 so only the curve of the SM is shown. For $\tau = 1.1$ the maroon line indicates the OSM simulations and the cyan line indicates the SM simulation. The black line represents a random distribution; points above the black line are clustered and points below are ordered. The vertical scale varies between figures..... 21
- Figure 2.5. Ripley's L value (a-c) and pair correlation (d-f) functions of the open system models (OSM) for a solid volume fraction of 1% and 20%. The one percent OSM is represented by

the red lines and the 20% OSM is represented by the blue lines. The vertical scale varies between figures. 22

Figure 2.6. Open system model for $\tau = 0.3$ and Voronoi tessellation for two regions of the settling particles. (a) Snapshot of OSM $\tau = 0.3$ with regions A and B highlighted. (b) Voronoi tessellation for region A. This region was chosen above the new fluid injection site but near the shock front. (c) Region B covers the new fluid injection site. The Voronoi polygons are colored by polygon area normalized to the mean Voronoi polygon area of a random distribution. An area of 1 indicates a random Voronoi polygon size, areas larger than 1 indicate ordering, and areas smaller than 1 indicate clustering. 24

Figure 2.7. Voronoi polygon area histogram for the settling model (SM) (a,b) and the open system model (OSM) (c,d) at 9% particle volume fraction. The area of each polygon is normalized to the mean area of Voronoi polygons for a continuous uniform random particle distribution. The black chain line shows the ideal random distribution as set forth by Ferenc and Néda (2007), the blue line is the histogram from $\tau = 0$ of the SM and the black vertical line indicates unity. The vertical scale varies between figures. 27

Figure 2.8. Voronoi region aspect ratio for the settling model (SM) (a,b) and the open system model (OSM) (c,d) at 9% particle volume fraction. The blue histogram is the aspect ratio histogram for $\tau = 0$ of the SM and the orange line is the named system. The rose diagram imbedded in the right corner of each plot shows the orientation of the long axis of the aspect ratio. The green bins are above the mean height of the bins and the blue bins are below the mean height. The rose diagram for $\tau = 0$ has the orientations displayed as well as the value of the inner black circle. Vertical scale for the probability density functions varies between figures..... 28

Figure 3.1. Initial condition of the dam break scenario before the domain is tilted. The red particles simulate plagioclase, the blue particle simulate olivine/pyroxene, and the yellow particles simulate magnetite. See table 3.1 for particle properties..... 39

Figure 3.2. Four timesteps from the 0.1 friction coefficient dam break scenario. The domain is rotated 16 degrees. The black fluid has the same properties as the resident white fluid and is used as a tracer. The white box follows the center of mass. (A) is the initial condition of the system after 16 degree rotation. (B)The two collapse regimes, toppling collapse in the upper

right corner of the column and sliding collapse (white line). (C) The fossil Kelvin-Helmholtz billow is the only remaining portion of the gravity current still in motion. Surface undulations of the heap flow are highlighted in white. (D) The particles have settled out of the Kelvin-Helmholtz billow and the heap flow continues to advance. 45

Figure 3.3. Velocity and kinetic energy for the particle friction coefficient of 0.58 simulation. Scaled time that are depicted in figure 3.2, $\tau=0.16$ and $\tau=0.42$ are highlighted, while $\tau=0$ and $\tau=0.83$ are the start and termination points on the axes. The line labeled RO indicates the time where the floor parallel velocity becomes dominant. 49

Figure 3.4. Force and contact anisotropy for particle friction coefficient 0.58. (a) The initial condition ($\tau=0$), (b) during the collapse ($\tau=0.16$), the transition from collapse to run-out ($\tau=0.42$), approaching the angle of repose ($\tau=0.83$). 51

Figure 3.5. Contact anisotropy and coordination number for particle friction 0.58. The position of $\tau=0.16$ and $\tau=0.42$ on the x axis are indicated, while the positions for $\tau=0$ and $\tau=0.83$ are the start and termination points of the x axis. 52

Figure 3.6. Contact and force fabric coaxiality for particle friction coefficient 0.58. The position of $\tau=0.16$ and $\tau=0.42$ on the x axis are indicated, while the positions for $\tau=0$ and $\tau=0.83$ are the start and termination points of the x axis. 53

Figure 4.1. Geologic map of the Sierra Valle Fértil modified from Otamendi, Vujovich, et al. (2009); Tibaldi et al. (2013); Walker et al. (2015) and geologic cross section with temperatures and pressures modified from Tibaldi et al. (2013); Walker et al. (2015). 71

Figure 4.2. Expressions of tonalitic melt extracted from amphibole gabbro cumulate preserved in the mafic complex of Valle Fertil. (a) Patches of in situ nonfoliated tonalitic melt separated from the mafic cumulate. (b) channels and veins of tonalitic melt in a gabbro cumulate host. (c) a variety of expressions where tonalitic melt is segregating from the gabbroic cumulate. See text for details. (d) Tonalite surrounding blocks of cumulate. 73

Figure 4.3. Hand samples a) FA10-03m, b) FA18-01, and c) FA18-03. Thin section images for the respective hand samples d) FA10-03, e) FA18-01a, and f) FA18-03. Each scale bar in the thin section image represents 10 mm. 76

Figure 4.4 QEMScan Ca maps of samples (a) FA18-01a and (b) FA18-03. (a) Arrows point to examples of higher Ca content on plagioclase rims. (b) Has no identifiable Ca zoning. This lack of zoning is the dominant result from the samples analyzed. 77

Figure 4.5. Photomicrographs of Famatinian samples. Only frame e is under plane polarized light. The others are under crossed polarized light. the scale bar is 0.5 mm in all subfigures. (a) shows a cluster of plagioclases (plag) whose grains continued to grow into melt filled pores after agglomerating from sample FA18-01a. Some textural equilibration of the smaller grains is present at triple junctions and in rounded convex grain boundaries. (b) Sample FA18-03 with plagioclase showing faceted grain boundaries that transition into irregular grain boundaries. Arrows show the location of the transition. Interstitial hornblende (Hb) is also present. Pyroxenes show alteration (Alt). (c) Sample FA18-03 with examples of the types of twins found in plagioclase. Arrows from top to bottom show growth twins, bent twins, and tapering twins. (d) Sample FA18-03 showing hornblende growing on the rims of and consuming clinopyroxene (cpx). We also see examples of faceted grain boundaries between pyroxene-pyroxene contacts, hornblende-hornblende, and some pyroxene-hornblende contacts (arrowed). (e) In this image of sample FA18-03 we see an example of some of the interconnected yet discrete grained hornblende networks. Image is in plane polarized light to highlight the interconnected hornblende network. Hornblende is seen as an interstitial phase and growing on the rims of clinopyroxene and orthopyroxene (opx). (f) Example of a quartz grain displaying mild subgrains with undulating extinction from sample FA18-01a. 79

Figure 4.6. Electron Backscatter Diffraction (EBSD) orientation results for sample FA10-03m. a) Phase map of the EBSD scanned area. b) Lower hemisphere equal-area projections of plagioclase [100] axis, and (010) and (001) poles to planes. c) Plagioclase misorientation axis and shape preferred orientation rose diagram. d) Lower hemisphere equal-area projection of hornblende (100) and (010) poles to planes, and [001] axis. e) Hornblende misorientation axis and shape preferred orientation rose diagram. Blue lines intersecting the orientation reference indicate the foliation direction. 86

Figure 4.7. Electron Backscatter Diffraction (EBSD) orientation results for sample FA18-01a dark band. a) Phase map of the EBSD scanned area. b) Lower hemisphere equal-area

projections of plagioclase [100] axis, and (010) and (001) poles to planes. c) Plagioclase shape preferred orientation rose diagram. d) Lower hemisphere equal-area projection of hornblende (100) and (010) poles to planes, and [001] axis. e) Hornblende shape preferred orientation rose diagram. Blue lines intersecting the orientation reference indicate the foliation direction. 88

Figure 4.8. Electron Backscatter Diffraction (EBSD) orientation results for sample FA18-01a

light band. a) Phase map of the EBSD scanned area. b) Lower hemisphere equal-area projections of plagioclase [100] axis, and (010) and (001) poles to planes. c) Plagioclase shape preferred orientation rose diagram. d) Lower hemisphere equal-area projection of hornblende (100) and (010) poles to planes, and [001] axis. e) Hornblende shape preferred orientation rose diagram. Blue lines intersecting the orientation reference indicate the foliation direction. 89

Figure 4.9. Plagioclase (a) and hornblende (b) misorientation axes for sample FA18-01a. The analyses of misorientation axes are not segregated into the distinct composition bands.

..... 90

Figure 4.10. Electron Backscatter Diffraction (EBSD) orientation results for sample FA18-03. a)

Phase map of the EBSD scanned area. b) Lower hemisphere equal-area projections of plagioclase [100] axis, and (010) and (001) poles to planes. c) Plagioclase misorientation axis and shape preferred orientation rose diagram. d) Lower hemisphere equal-area projection of hornblende (100) and (010) poles to planes, and [001] axis. e) Hornblende misorientation axis and shape preferred orientation rose diagram. Blue lines intersecting the orientation reference indicate the foliation direction based on the girdles found for the [100] and [001] axes for plagioclase and hornblende respectively. 91

Figure 4.11. Pole figures for individual plagioclase grains from each sample. The grain maps are

colored to the inverse pole figure (IPF) key which is referenced to the mean orientation of the grain. The color scale, located at the bottom right of each grain map, is adjusted so that light grey is 0° and dark grey is 10° or more of misorientation. Sharp boundaries between colors in the grain maps indicate internal lattice distortions. a) FA10-03 shows a minor amounts of internal lattice distortion. The corresponding pole figures show a minor amount of dispersion of poles in [100] and (001), with a pole of rotation at (010). b) Grain from

FA18-01a dark band shows little to no internal lattice distortions in the grain map and minor amounts of dispersion of poles in the (010) and (001) pole figures with a pole of rotation at [100]. c) This grain from the light band of sample FA18-01a shows several sharp color transitions indicating internal lattice distortions, however, total misorientation remains below 10°. Pole figures show dispersion of poles in (010) and (001), with a pole to rotation in [100]. d) This plagioclase from sample FA18-03 displays several transitions of colors across sharp boundaries indicating minor amounts of internal lattice distortions. There seems to be a small amount of dispersion of poles in [100] and (001) with a pole of rotation at (010). 92

Figure 4.12. Misorientation figures colored to inverse pole figure (IPF) key for hornblende and quartz and are referenced to the mean orientation of each grain. The color scale, located at the bottom right of the hornblende grain for all hornblende in a) and to the bottom right of the quartz grain for all quartz in b), is adjusted so that light grey is 0° and dark grey is 10°. Sharp boundary between colors indicate crystal lattice distortions in the form of dislocations. Boxes with red lines indicate either that quartz was not analyzed (FA18-03) or that quartz was too small to get a proper misorientation figure (FA10-03). a) Sample FA10-03 hornblende shows minor amounts of misorientation with a good alignment of dislocations. b) Sample FA18-01a light band hornblende shows minor misorientation and quartz show misorientations with some alignment of dislocations. c) Sample FA18-01a dark band both hornblende and quartz show minor amounts of misorientation with good alignment of dislocations. d) Sample FA18-03 hornblende shows minor amounts of misorientation..... 95

Figure 4.13. Kernel average misorientation (KAM) histograms for plagioclase, hornblende, and quartz. KAM provides the amount of misorientation associated with each dislocation. a) sample FA18-01a light band, b) sample FA18-01a dark band, c) sample FA18-03, and d) sample FA10-03. The peaks for all four histograms are around 1° of misorientation.96

LIST OF TABLES

Table 3.1. Particle properties	40
Table 4.1. Composition of selected samples.....	78
Table 4.2. Grain size and aspect ratio of the main silicate phases from the selected samples.	81
Table 4.3. Textural parameters for selected samples	85

ACKNOWLEDGEMENTS

There are many people whose support throughout my time in graduate school I am grateful for. First and foremost, I want to thank George Bergantz, my adviser, for his support and encouragement. You helped me regain my focus when I was going through a hard time. We also had some great times while doing field work.

I also want to thank my committee, Mike Brown, Cailey Condit, David Schmidt, and Michelle DiBenedetto. Our discussions and your comments and questions helped me to progress on my research. Cailey, thank you so much for inviting me to participate in your group meetings.

I would not be where I am today without the help and support of Jill Schleicher. She introduced me to the department and was an instrumental part of my first two years of research. Her knowledge and understanding of computational fluid dynamics really helped to get me up to speed.

My final chapter would not have been possible without the support of Zoja Vukmanovic. I really appreciate all your help with the EBSD and the hours you spent discussing the science with me on Skype.

I found geology while enrolled at Illinois Central College. Ed Stermer and Cheryl Resnick, I appreciate your support and encouragement throughout the years. I am glad that we have stayed in contact, and I can call you friends.

To my partner, Virginia, I am so grateful for your support and encouragement throughout the years. I could not have done this at all without your support and love.

Finally, I would like to thank all my friends and family. There are too many people to name individually, but you all have helped to keep me sane throughout this process.

Chapter 1. INTRODUCTION

Magma supplies the material erupted from volcanoes, and the rheology of the magma is an important control on the eruption style. There exists a positive correlation between magma viscosity and explosivity, where the former increases with increased crystal cargo. Despite its importance to our understanding of eruption explosivity, there is a lack of insight into the mechanics of crystallizing magmatic systems. The inability to observe active magmatic systems is a major hindrance to learning about these complex systems. Petrologic, geochemical, and seismic analyses provide evidence that magmas are complex systems that exist as crystal-rich mushes for much of their entirety (Calvert, 2011; Calvert et al., 2008; Ducea et al., 2015; Jagoutz & Klein, 2018), but lack in explanation of the mechanics of the systems. In order to start rectifying this gap in knowledge, we need to first explore the qualities of melt-rich vs crystal-rich systems, the process of density-driven crystal settling, the interactions between melt and magma mush, and the possible modes of extracting interstitial melt from mushes.

Magma is a dynamic, heterogeneous hydrogranular system where the rheology of the crystallizing magma changes as it transitions from melt-rich to crystal-rich systems (Marsh, 1981). The change in rheology is largely a consequence of the number of interacting crystals (Bergantz et al., 2017). In a melt-rich system where crystals are suspended or settling from the melt, the interactions between crystals is minimal and thus the melt is free to flow unhindered by crystal interactions. Conversely, when crystallinity is high, crystals form a network of touching grains. These crystal interactions dominate the behavior of the magma and can impede magma movement via crystal jamming (Bergantz et al., 2017; Marsh, 1981). There is also an intermediate phase where both a crystal mush and a melt reservoir can exist simultaneously within a system.

Erupted volcanic material often includes an abundance of crystal clusters (Cooper, 2015; Cooper & Kent, 2014; Seaman, 2000). However, there is uncertainty as to whether these clusters are a product of disaggregation and eruption of portions of the crystal mush or result from the eruption of crystals clusters already in suspension in the melt. As crystals nucleate and grow, differences in density between the crystals and the melt cause relatively denser crystals to settle out. The settling crystals can either directly settle to the floor of the magma as individual crystals, or they may cluster while in the suspended regime to form glomerocrysts by a process termed synneusis (Vance, 1969), eventually settling as glomerocrysts. A mush formed by individually settled crystals exhibits tighter packing and a higher solid volume fraction compared to a mush consisting of settled glomerocrysts (Jerram, 2003). The degree of crystal packing may influence the remobilization of the mush with magma recharge and determines the mechanical response of a mush to shearing. Shearing a loosely packed mush will compact the mush body while shearing a tightly packed mush will dilate the mush body.

The interface between the crystal mush and the bulk magma is a dynamic region where granular flows along the interface can entrain melt from the bulk magma into the mush. Evidence for crystal-rich gravity currents exists in the trough bands of the Skaergaard layered mafic intrusion and the schlieren bound troughs of the Tuolumne Batholith (Paterson et al., 2008; Vukmanovic et al., 2018). Yet, little is known about the kinematics of particle-rich gravity currents that propagate in a viscous fluid. Analogue dam break experiments (Forien, Tremblay, Barnes, Burgisser, & Page, 2015), debris flow flume experiments (Iverson, 1997), photoelastic discs (Estep & Dufek, 2013), and numerical models of dam breaks in fluids with a similar viscosity to water (Topin et al., 2012) all provide insights into particle-rich gravity currents. However, analogue experiments fail to provide information on fluid flow pathways and the distribution of force and contacts between

granular material, while numerical models in fluids with viscosities similar to water fail to capture the kinematics of systems with a low Reynolds number.

The expulsion of interstitial melt from the crystal-mush is necessary to separate the liquid from the solid and fractionate the magma. The mechanisms that reduce pore spaces and extract melt from the interstice of crystals within cumulates are still highly debated topics in igneous petrology (Holness et al., 2017). An obstacle to understanding the melt extraction process is the inability to directly observe in situ crystal-rich magmas. Our current understanding of magmatic systems is that they exist mostly in a crystal-rich, near solidus state (Cooper & Kent, 2014; Ward et al., 2014). When crystallinity of the magma is greater than 50%, The magma is believed to become rheologically locked and unable to flow (Marsh, 1981; Tapster et al., 2016). This has led to viscous compaction (Mckenzie, 1984, 2011) being one of the most cited mechanisms for melt extraction (Bertolett et al., 2019; Cashman et al., 2017; Shirley, 1986). However, cumulates of the Skaergaard layered mafic intrusion have geochemical evidence of melt extraction and both shape preferred and crystallographic preferred orientations (SPO and CPO respectively) of plagioclase crystals with minimal deformation (Holness et al., 2017; Vukmanovic et al., 2018). The lack of plastic deformation indicates that viscous compaction could not be responsible for the extraction of melt from the Skaergaard cumulates, indicating that other mechanisms must be at work. The formation of both an SPO and CPO without deforming the crystals suggests that our understanding of the rheology of crystal-rich magmas is incomplete.

To address the different rheological regimes of magmatic systems, this dissertation is divided into three standalone chapters. Chapter 2 “On the hydrodynamics of crystal clustering” uses numerical models of both an open system that has crystal settling while new melt is intruded and a settling only system to investigate the formation of crystal clusters. Chapter 3 “On the

hydrogranular dynamics of magmatic gravity currents” employs numerical models of dam break scenarios in tilted domains to study the different kinematic regimes that can develop in the advancing gravity current. The final chapter “On the expulsion of melt from the interstitial spaces of a magma mush by pore space reduction” combines field-based sampling and observations with petrographic analyses to determine the mechanism of pore space reduction and melt extraction in a crystal mush.

Chapter 2. ON THE HYDRODYNAMICS OF CRYSTAL CLUSTERING

Originally published in Philosophical Transactions A

Co-authored by Michael Z. McIntire, George W. Bergantz, Jillian M. Schleicher

2.1 INTRODUCTION AND BACKGROUND

2.1.1 *introduction*

The clustering of particles in a moving fluid was first described in the 1940's in the context of industrial applications (Wilhelm, 1948), and has been subsequently described in sedimentology, volcanology, and atmospheric transport and has been of significant interest in the chemical processing industry (Cahyadi et al., 2017). Clustering is an emergent phenomenon in that it arises from the complex interplay between a hydrodynamic template and a dispersed phase, typically solids, and can manifest multiphase instabilities that have no counterpart in molecular fluids (Fullmer & Hrenya, 2017). Even the definition of a cluster will depend on the application; perhaps the most generic definition of a cluster might be that it is a region of elevated particle concentration relative to a random reference state, where particles move as an ensemble. It has been standard practice in material science to differentiate clusters, which result from hydrodynamic processes alone, from orthokinetic agglomerates, which are bonded, jammed or otherwise cohesive arrangements of particles in contact (Horio & Clift, 1992). Our objective here is to exemplify measures of particle clustering from hydrodynamic forces that might occur in magmas. A complete assessment of the formation of crystal agglomerates and their fragmentation (e.g. (Hansen et al., 1998; Wang et al., 2005)) will be the subject of a future communication. Below, we first describe the general emergence, kinematics and dynamics of clustering. We then describe specific

applications to magmatic processes, by consideration of simple examples involving crystal settling and open-system stirring in three idealized basaltic systems.

2.1.2 *Geologic observations and motivations*

There are numerous examples of crystal clustering in the volcanic and plutonic record, but the understanding of how they arise under dynamic conditions is incomplete. The proposition that the mechanical behaviour of magmas may be strongly influenced by crystal clusters (Jerram, 2003) and that magmas may often reside in a mushy or crystal-rich state (Bachmann & Bergantz, 2004), motivates renewed interest in understanding the origins of clustering. In particular the recognition that many of the "crystal clots" and glomerocrysts found in volcanic rocks may be samples of crystal mush (Beane & Wiebe, 2012; Ellis et al., 2014; Neave et al., 2013; Seaman, 2000; Sliwinski et al., 2015; Troch et al., 2017), while others may originate by hydrodynamic interaction under dilute conditions, commonly referred to as synneusis (Coetzee et al., 1995; Schwindinger & Anderson, 1989; Vance, 1969; Vogt, 1923). The textural analysis of plutonic rocks has also motivated an interest in crystal clusters in an effort to better understand cumulate formation, stress transmission and the corresponding magmatic fabric (Beane & Wiebe, 2012; Paterson et al., 2019).

One of the obstacles in the interpretation of complex crystal zoning in crystal clusters is the degree to which clusters originate by repeated magma stirring, and those which form while they reside in a static or near static crystal mush. Hence our goal is simply to explore how crystals clusters arise by stirring and sedimentation under plausible geological conditions.

2.1.3 *Theoretical overview*

In this study we consider the clustering that may occur as a result of two processes operating simultaneously: sedimentation from the steady acceleration due to gravity, and particle dispersion

from non-steady forces arising from fluid circulation caused by an open system intrusion of new magma. Non-cohesive particle clusters can form in either inertial (Monchaux et al., 2012) or viscous (Thøgersen et al., 2016; Wylie & Koch, 2000) dominated conditions, and by processes related to dissipation from inelastic particle-particle interactions (Hoomans et al., 1996; J. Li & Kuipers, 2007), hydrodynamic sorting as a function of particle Stokes number (defined below) (Bergantz & Ni, 1999; Burgisser & Bergantz, 2002; Crowe et al., 1988; Tang et al., 1992), and by particle-wake attraction producing KDT (kissing-drafting-tumbling) and clustering behaviour (Chen et al., 1991; El Yacoubi et al., 2012; Fortes et al., 2006; Fu et al., 2017; Jayaweera et al., 1964; Joseph et al., 1994; Nie et al., 2015; Schwindinger, 1999; Suckale et al., 2012; Wang et al., 2014; Wu & Manasseh, 1998). Individual particles can leave and join clusters intermittently, and clusters can form from systems with initially low particle volume fractions even under viscous conditions (Arbaret et al., 1996; Chen et al., 1991; Crowley, 2006; Huisman et al., 2016; Kawabata et al., 2013; Suckale et al., 2012). Particle clustering can give rise to what are termed mesoscale transient structures as manifested in both laboratory and numerical experiments (Tanaka et al., 2002; Tsuji et al., 2008; Tsukada et al., 1997).

A dilute multiphase system undergoing sedimentation in an otherwise quiescent fluid can manifest clustering. Strong clustering can arise from the progressive unsteadiness associated with the cycle of particle wake formation, asymmetry and shedding (Ern et al., 2012; Jenny et al., 2004; Kajishima, 2004; Parthasarathy & Faeth, 2006; Suckale et al., 2012). This in turn enhances sedimentation by a wake attraction effect that produces a reduction in drag of trailing particles, and an increase of sedimentation flux by up to an order of magnitude (Huisman et al., 2016; Uhlmann & Doychev, 2014). A freely sedimenting system is described by three degrees of freedom, the particle volume fraction, the particle-fluid density ratio and the Galileo number, Ga ,

$$Ga = \frac{U_g d}{\eta} \quad (2.1)$$

where d is the particle diameter, η the kinematic viscosity and U_g a scaled settling velocity,

$$U_g = \left[\left(\frac{\rho_p}{\rho_f} - 1 \right) g d \right]^{1/2} \quad (2.2)$$

The Galileo number as defined in (2.1) can be considered as a kind of Reynolds number based on the gravitational settling velocity; we retain the use of Galileo number here to be consistent with the use in Uhlmann and Doychev (2014). For an isolated particle it has been observed that a value of Ga equal to around 120 produces steady vertical motion with an axisymmetric wake, and a value of Ga equal to 178 produces steady oblique motion. The onset of strong clustering in a semi-dilute multi-particle system (volume fraction of $O(10^{-3})$) is associated with values of the Ga above 120, reinforcing the notion that non-steady wake behaviour and particle attraction can yield clustering.

Non-dilute sedimenting systems also manifest complex velocity fluctuations even under conditions of low particle Galileo (or Reynolds) numbers, where particle wakes produce fluid channelization and hence clustering (Crowley, 2006; Faroughi & Huber, 2015; Guazzelli & Hinch, 2011; Hoyal et al., 1999; Suckale et al., 2012). It has been difficult to experimentally resolve and generalize the stochastic nature of local many-body interactions, whether by collisions or by wake unsteadiness at high Ga , or from wake interference effects at low Ga . Significant progress has been made in describing the macroscopic average behaviour of particle sedimentation within the context of traditional notions of hindered settling particle flux (Faroughi & Huber, 2015; Suckale et al., 2012). Predicting clustering and the role of particle-local wake perturbations, relative to fluid reorganizations and particle crowding that occurs in non-dilute conditions at both high and low Ga , is not yet possible.

Sedimentation in an environment where there is fluid motion arising from far-field forces has also been studied, typically under conditions of near-laminar viscous flow (Lavorel & Le Bars, 2009; Marsh & Maxey, 1985; Verhoeven & Schmalzl, 2009; Weinstein et al., 1988) or chaotic and formally turbulent flow (Crowe et al., 1988; D. Martin & Nokes, 1988; J. E. Martin & Meiburg, 1994; Michaelides et al., 2017; Paiement-Paradis et al., 2003; Raju & Meiburg, 1995). One measure of particle interaction and hence the possibility of clustering, is called the dense-dilute threshold D_D (Crowe et al., 1998):

$$D_D = \frac{t_c f}{t_v}, t_c = \frac{1}{n\pi U_{rms} d^2}, t_v = \frac{(\rho_p - \rho_f) d^2}{18\mu} \quad (2.3)$$

where t_c is characteristic time between collisions, n the particle number density, μ is the dynamic viscosity, U_{rms} the root mean square of the particle speed and t_v is the particle velocity response time. The drag factor, f , is:

$$f = 1 + 0.15 Re_p^{0.687} + \frac{0.0175}{1 + 42500 Re_p^{-1.16}}, Re_p = \frac{U_g d}{\eta} \quad (2.4)$$

where Re_p is the particle Reynolds number based on U_g the terminal fall velocity with a kinematic viscosity η ; f approaches unity for small values of Re_p as might occur in magmatic conditions. If D_D is < 1 , particles do not have time to respond to the far field fluid dynamic forces before interacting with another particle, and the multiphase dynamics are dominated by particle-particle interactions. This distinction can be important in establishing regimes of clustering behaviour.

For conditions relevant to magmatic behaviour Burgisser et al. (2005) proposed two dimensionless groups to identify when the particle motion was dominated by the non-steady, far-

field fluid motion, or by the steady acceleration of gravity associated with sedimentation. The first is the Stokes number, S_T :

$$S_T = \frac{2}{3} t_v \frac{\Delta U}{\delta} \quad (2.5)$$

where ΔU is the characteristic speed change of the fluid over a length scale δ . Particles with a $S_T > 1$ are decoupled from the flow; buoyancy forces will dominate their behaviour and settling can be described as occurring in a still fluid. The importance of the steady acceleration of gravity relative to the background flow ΔU is given by:

$$\Sigma_g = \frac{gt_v}{\Delta U} \left(\frac{\rho_p - \rho_f}{\rho_p} \right) \quad (2.6)$$

where the sign of Σ_g indicates whether particles rise, sink or are neutrally buoyant. The magnitude is a measure of the time scale it takes a particle to settle a characteristic distance over the time scale the far field velocity has to transport the particle that characteristic distance. At vanishing S_T and Σ_g , the particles circulate as passive tracers.

The dimensionless groups described above give some guidance as to the conditions that might influence clustering. For magmas, the Galileo and Stokes numbers will typically be much less than unity (Burgisser et al., 2005), expressing the absence of particle inertia resulting from the control by viscosity. In the absence of fluid circulation and with low Ga , it is unlikely that KDT processes will produce significant clustering in an otherwise dilute fluid (Uhlmann & Doychev, 2014). And at low St , clustering is likely to result primarily from advective gathering of crystals, either in stagnation points, wall boundary layers or along horizons of particle sedimentation. The simulations described below are designed to include all these processes and quantify the resulting clustering.

2.1.4 *Objectives of the study*

The objectives of this study are to exemplify measures of clustering as might arise in both dilute and dense magmatic systems undergoing simultaneous sedimentation and circulation from open system input. Our focus is on the mobile portion of the multiphase mixture, hence we do not address clustering that occurs in the settled bed. We will consider bulk measures of clustering as discussed in (Jerram & Cheadle, 2000; Jerram et al., 1996; Rudge et al., 2008), as well as Voronoi tessellation, and demonstrate how they recover clustering scales and fabric. We will do this with multiphase, time dependent numerical simulations that track the trajectory of every particle (the terms crystal and particle are used interchangeably) and hence recover the entire distribution of all particles at every time step. This will allow for the examination of how clustering changes during on-going sedimentation and open-system circulation.

2.2 METHODS

2.2.1 *DEM-CFD simulations of an open-system intrusion into an olivine bearing magma chamber*

To develop and exemplify some relevant concepts of crystal clustering caused by hydrogranular processes, we employ the discrete element method combined with computational fluid dynamics (DEM-CFD), a framework we have previously employed and is well described elsewhere in the literature (Bergantz et al., 2015; Schleicher et al., 2016) (please see Supporting Information in (Bergantz et al., 2017; Schleicher & Bergantz, 2017) for a full elaboration of the theory and numerical implementation). Briefly, the DEM-CFD method combines a Eulerian representation of the conservation of mass and momentum balance for the fluid phase, and the motion of a particle of mass m , is explicitly solved as a Lagrangian quantity,

$$m \frac{d}{dt} \begin{pmatrix} \mathbf{v} \\ \boldsymbol{\omega} \end{pmatrix} = \sum \begin{pmatrix} \mathbf{F} \\ \boldsymbol{\Gamma} \end{pmatrix} \quad (2.7)$$

Where t is time and with translational velocity vector \mathbf{v} and rotational velocity vector $\boldsymbol{\omega}$ subject to force vector \mathbf{F} and torque vector $\boldsymbol{\Gamma}$. Our application of the DEM-CFD method explicitly resolves particle sustained frictional contact, collisions, buoyancy, hydrodynamic drag, interphase momentum transfer and implicitly treats lubrication; additional information regarding the governing equations, and the verification and validation procedures are can be found in (Bergantz et al., 2017; Garg et al., 2012a; Garg et al., 2012b; T. Li & Guenther, 2012). The fluid phase is modeled with the usual Navier-Stokes equation on a cell size that is approximately 2.5 particle diameters. One simplification we make is that the particles are spherical. This will clearly impact the styles of clustering (Bergantz et al., 2017; Rudge et al., 2008) and as most crystals only approximate spherical conditions, our results are not intended for direct comparison with geological examples. Nor do we model crystal transport from plumes that might originate at crystal-rich boundary layers (Bergantz & Ni, 1999; Jellinek & Kerr, 2001; Marsh, 1988). Rather our aim is to develop and demonstrate a framework for the quantification of clustering that can serve as a proof-of-concept, which can then be extended to the complexity of natural examples in subsequent work.

We present the results from four numerical models. All have the same size of 2.56 m by 1.28 m and initial fluid condition of a reservoir filled with basaltic melt at a temperature of 1290° and an MgO content of 10.76%. The melt phase has the properties of basalt with a viscosity of .2 Pa s that was held constant throughout the simulations. The first model is initialized with a continuous (pseudorandom) random distribution of olivine crystals with a uniform diameter of .004m that comprise nine volume percent, and this system is allowed to settle. This model is referred to the '*settling model*' and will be identified as 'SM' in the discussion below. The next three

models are initialized with a continuous pseudorandom distribution of, one, nine and twenty volume percent crystals. In these three models more primitive crystal-free basaltic magma is injected into the domain from the base with a velocity of .023 m/s with a temperature of 1340° and an MgO content of 12.94%. In these models crystals are redistributed by the complex interplay of both settling and fluid motion resulting from the new intrusion from below. We will refer to these three as '*open-system models*' or 'OSM' below. The reader is strongly encouraged to now view the three models designated OSM in the movie file OSM-1.mp4 in the supplemental information.

Figure 2.1 shows the initial nine volume percent crystals system at three time steps for dimensionless times of $\tau = 0, .5$ and 1.1. Dimensionless time τ is defined as,

$$\tau = \frac{t}{t^*} \quad (2.8)$$

where t is time and t^* is the time it takes a single particle to settle the vertical height of the domain under conditions of laminar Stokes settling. For our simulation parameters each increment of τ is 90.332 seconds of wall-clock time. In figure 2.1 one can see the progress of sedimentation and the fluid mixing that takes place as a result of the open system intrusion. As crystals accumulate on the floor a so-called 'mixing bowl' is formed where the incoming magma has fluidized crystals arriving from positions initially in the upper portions of the magma reservoir; see discussion in (Bergantz et al., 2015; Schleicher et al., 2016).

All three initial crystal fractions for the OSM are shown together in figure 2.2 for three time steps, $\tau = 0, .5$ and 1.1 (this is 0, 45.166 and 99.365 seconds of wall-clock time); See movie file OSM-1.mp4. Each time step has two rows, the upper row shows the melt temperature and the bottom row the position of the particles as well as the MgO compositional variation in the melt phase from mixing between the resident and in-coming more primitive basalt. As the simulation

proceeds for each case, the location of each crystal is tracked creating a time series with position, velocity, and local temperature and melt composition for the entire crystal population. In this study we are only interested in the dynamics of clustering, and do not consider the evolution of the scalar fields of temperature and composition further. We refer the interested reader to (Schleicher et al., 2016) for a discussion of time-dependent scalar field mixing and associated crystal reactions in open-system magmatic events.

2.3 MEASURES OF CLUSTERING

In order to discuss the processes that produce clustering in the mobile portion of magmatic systems there needs to be a means of quantifying the clustering. The domain area within which the mobile portion resides changes with time as particles exit to form a settled bed, and the upper boundary between the region of pure melt and that with settled particles moves downward with time. For example, the yellow horizontal line in figures 2.1 and 2.2 is the upper boundary (at those time steps) of the mobile domain, and the lower boundary is settled bed. So, the clustering statistics discussed below are applied within that region, which itself is becoming smaller as settling proceeds.

Several methods of cluster quantification are implemented in this study and discussed below. The first section introduces the R index and two correlation functions, Rippley's $L(r)$ and $g(r)$ functions. These methods have been used to describe the distribution of point arrays and have been used for textural analysis in metamorphic and igneous petrology (Hirsch et al., 2000; Jerram et al., 1996; Jerram et al., 2003; Rudge et al., 2008). The second section introduces the use of Voronoi tessellations for cluster analysis. The Voronoi tessellation has the ability to provide geometric data without predefining length scales (Uhlmann & Doychev, 2014). Below we

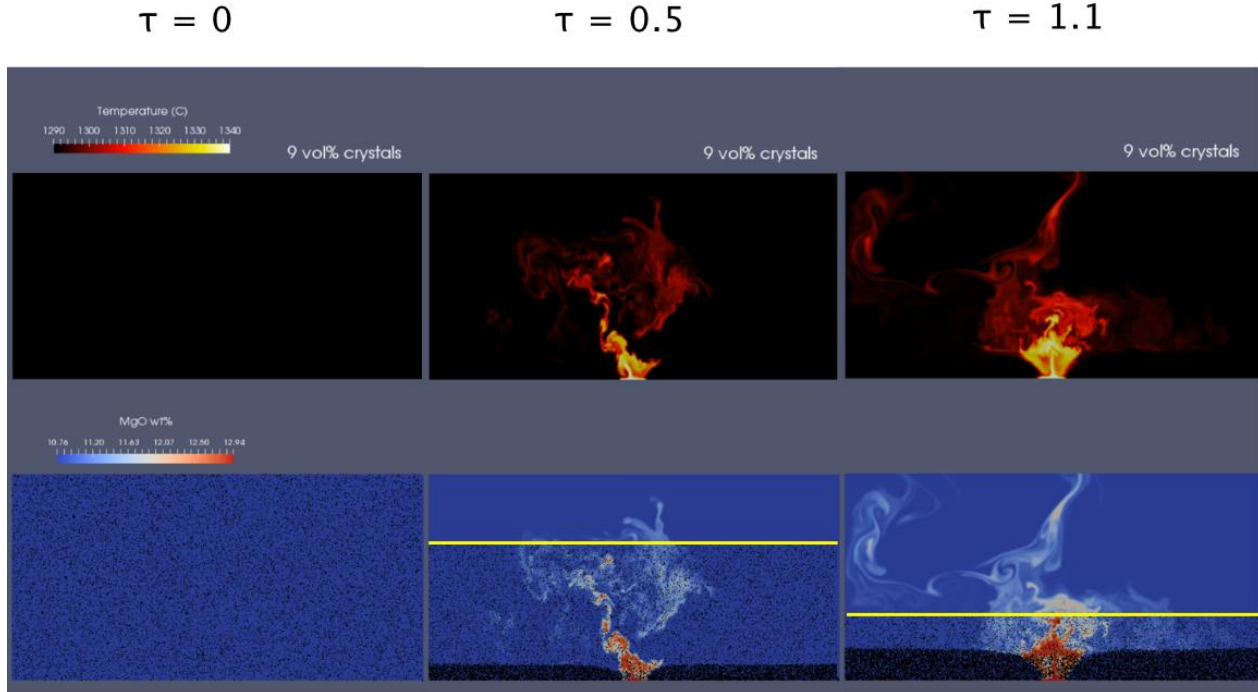


Figure 2.1. Three steps, $\tau=0,0.5,1.1$, from the initially 9% solid volume fraction of olivine open system model (OSM). The top row shows the changes in the temperature of the multiphase system between the initial temperature of 1290° and the temperature of the new intruding basalt of 1340° . The bottom three panels show the particles (olivine crystals) as black points and the background color is the change in MgO wt% between the initial value of 10.76 and the new intruding value of 12.94. Variations between these reflect mixing of the resident and incoming magma. A yellow line is drawn at the shock front that separates the settling particles and the region of the domain that no longer has particles.

apply these measures of clustering to the simulations described in section 2 and discuss the implications for geological applications in section 4.

2.3.1 Bulk clustering measures, R , Ripley's $K(r)$, $L(r)$, and $g(r)$ functions

One method that has been used for quantifying crystal clusters is the aggregation index, R (Clark & Evans, 1954; Jerram et al., 1996; Rudge et al., 2008)}. The R index is the ratio of the mean nearest neighbour distance over the expected value from a spatially continuous random distribution.

(2.1)

$$R = \frac{r_a}{r_E}$$

Here, r_a is the mean nearest neighbour distance, and r_E the expected value. The value of r_E is:

$$r_E = \frac{1}{2\sqrt{\lambda}} \quad (2.9)$$

where λ is the intensity or the total number of points over the total area. Jerram et al. (Jerram et al., 1996) demonstrate how the R value can provide criteria for a collection of objects to be described as ordered, random or clustered. For a system of points of vanishing volume that transition is indexed to a value R equal to unity. However as discussed in (Jerram et al., 1996) there is no single value of R that discriminates ordered from clustered states in natural materials with finite area. A random distribution of natural grains will always have an R value greater than unity. We have illustrated this in figure 2.3, which shows the random sphere distribution line or RDSL, that delimits the ordered from clustered states as a function of the solid volume per cent. The interested reader is directed to figure 2.5 of (Jerram et al., 1996) for the derivation of the RDSL as a function of solid volume per cent.

The R value of four simulations as a function of solid volume fraction is shown in figure 2.3, which is a plot of R as a function of solid volume fraction. The random sphere distribution line (RDSL), as developed in (Jerram et al., 1996), is shown dividing the clustered from ordered regions. A number of interesting features are apparent. Firstly, note that the $\tau = 0$ values for the four simulations increasingly departs from the expected ideal RDSL as the solid volume per cent increases. This is a consequence of the fact that our initialization of the domain, which is based on a thinned continuous pseudorandom algorithm, leads to an apparent ordering; that is an artefact.

This arises as the domain is progressively initialized with finite area particles; the remaining space induces a filtering such that a truly random choice is moderated by the available locations that can accommodate a particle. Secondly, it is interesting to note that for any individual simulation, there isn't a large change in the solid fraction of the mobile region as the simulation proceeds. This is due to the fact that the loss of particles to the settled bed, which should decrease solid per cent, is almost balanced by the reduction in the mobile volume that contains crystals. For example, in figures 2.1 and 2.2 the mobile volume is between the horizontal yellow line and the settled bed, and the solid volume per cent stays nearly constant in that region. The fact that the solid per cent does not change markedly as the simulations proceed suggests that there is a local self-similarity or qualitative stationary state in the average mass per cent.

The R value provides a global metric of the clustering in the system but does not provide information on cluster size when clustering is present. To obtain more information about the particle distributions we will use what are called Ripley's $K(r)$, $L(r)$, and $g(r)$ functions (Ripley, 1976, 1977), the reader is directed to (Rudge et al., 2008) for a more complete presentation. The $K(r)$ function is defined as:

$$K(r) = \frac{E}{\lambda} \quad (2.10)$$

where E is the number of particle centers in a given radial distance, r , from a randomly chosen particle center. The result of this equation is an area. The more points present within the boundary of the radial distance, the larger the area will be. If the area is larger than the area created by the area of a circle using the radial distance there is clustering, while a smaller area indicates ordering. A complete random spatial distribution of points within the radial distance will yield a K value of

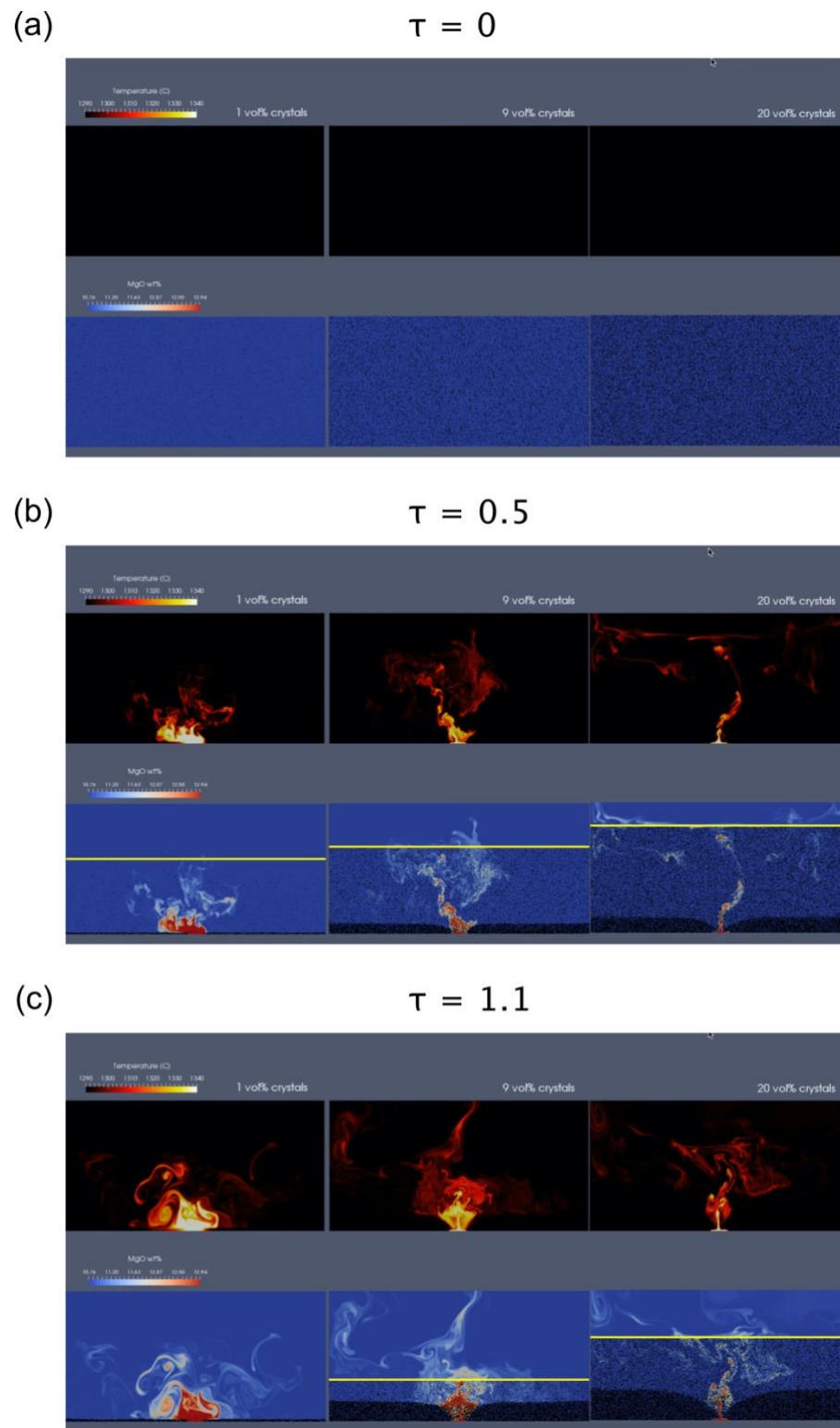


Figure 2.2. Three time steps, $\tau=0,0.5,1.1$, from three open system models (OSM) which differ by solid volume per cent. From left to right the solid volume fractions are, 1%, 9% and 20%. The

three times correspond to those in text. A yellow line is drawn at the shock front between the settling particles and the region of the domain that no longer has particles in the lower half of figures (b) and (c). The reader is directed to the movie OSM-1.mp4 in the electronic Supplementary material.

πr^2 . The $K(r)$ function is usually expressed in a more useable form as (Rudge et al., 2008):

$$L(r) = \sqrt{\frac{K(r)}{\pi}} \quad (2.11)$$

where a completely spatially random distribution would yield an $L(r)$ equal to r .

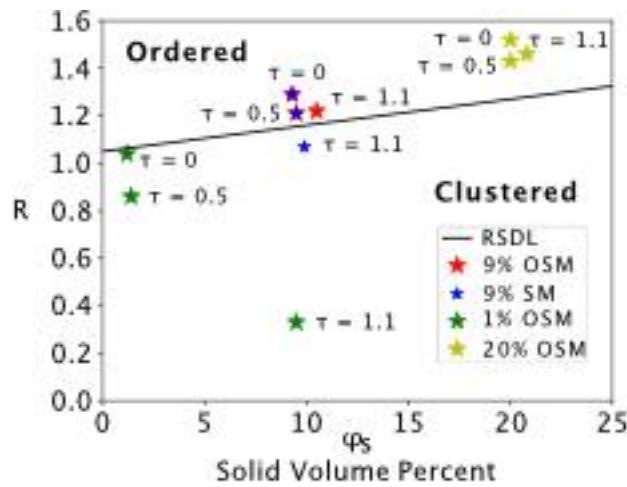


Figure 2.3. R index vs solid volume per cent, ϕ_s . The black line is the Random Sphere Distribution Line (RSDL) from Jerram et al., (1996). The points shown are from $\tau = 0, 0.5,$ and 1.1 of the 9% solid volume per cent settling model (SM) and the solid volume per cent of 1%, 9% and 20% open system models (OSM).

Figure 2.4 shows the $L(r)$ function for different radius values for the OSM and the SM for the initially 9%, and figure 2.5 shows the same for the OSM initially 1% and 20% systems. By selecting a random subset of particles from the system and obtaining their $L(r)$ values, one can potentially obtain insight into the particle distribution of the system. However, in this study we used the average $L(r)$ of all the particles in the system to obtain the average behaviour. We use the average because the system has over 10^5 particles in several different kinematic regimes. The

total number of particles needed to accurately display the particle distribution was not computationally feasible. We calculated the $K(r)$ function for all particles in each system and used the average $K(r)$ values of the individual systems in the $L(r)$ function. The black line in figures 2.4 and 2.5 indicates a completely random distribution; the region above the line indicates a clustered distribution, and below the line indicates an ordered distribution. As with the solid fraction versus the R index, there is no significant difference between the $L(r)$ function values for the first two time steps in the 9% OSM and SM systems. In figure 2.4 for $\tau = 0, .5$ both the open-system and settling-only cases both start in the ordered regime and trend to spatial randomness with larger radial distances. For figure 2.4c, $\tau = 1.1$, there is a bifurcation of the two curves after a radial distance of 0.4 cm. Each radial distance is increased by 0.2 cm, the radius of the particles in the system. In figure 2.4c at greater radial distances the OSM tends to a more ordered distribution, while the SM tends to spatial randomness with greater radial distances.

Figure 2.5a-c are $L(r)$ curves for the 1% and 20% systems at $\tau = 0, .5$ and 1.1. The OSM 1% and 20% are diverging by $\tau = 0.5$ and the 1% system undergoes clustering near the particles and moves to ordered with increasing radial distances, while the 20% system is ordered near the particles, but converges on random with increasing radial distances. In figure 2.5c, at $\tau = 1.1$ the 20% system starts in the ordered regime, but approaches randomness before increasing to a more ordered state. Figure 2.5c and f omits the 1% OSM results because by that time step the majority of particles have settled and the clustering analysis gives spurious results.

Another way to represent the clustering is with Ripley's pair correlation function $g(r)$, where:

$$g(r) = \frac{1}{2\pi} \frac{dK(r)}{dr} \left(\frac{1}{r} \right) \quad (2.12)$$

A solution of $g(r) = 1$ indicates a complete spatial random particle distribution, $g(r) > 1$ means the distribution is clustered, and a solution of $g(r) < 1$ means the distribution is ordered. This function

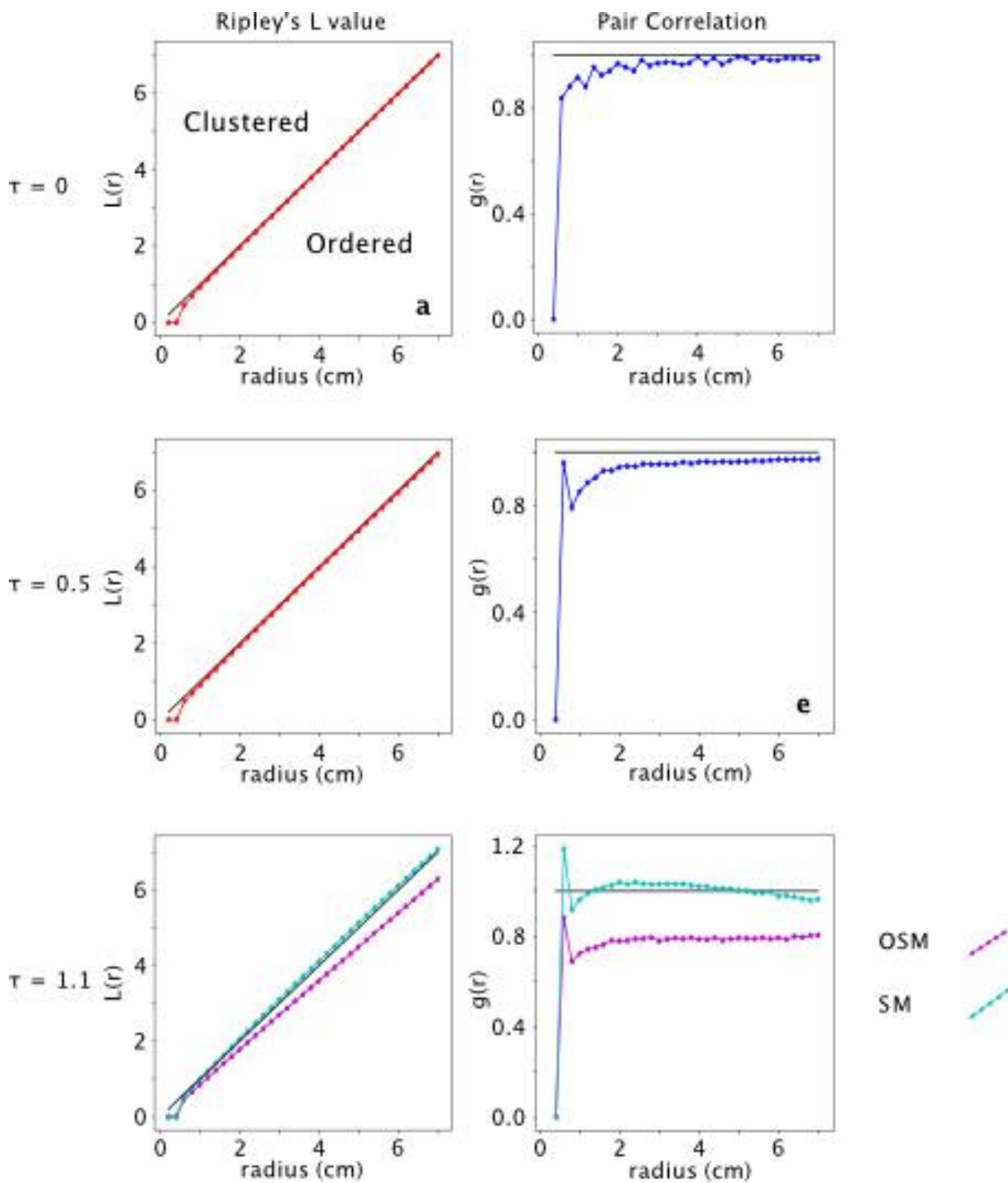


Figure 2.4. Ripley's L value(a-c) and pair correlation (d-f) functions and for both the open system model (OSM) and settling model (SM) at 9% crystal volume per cent. The results for the OSM

and SM were similar for $\tau = 0$ and 0.5 so only the curve of the SM is shown. For $\tau = 1.1$ the maroon line indicates the OSM simulations and the cyan line indicates the SM simulation. The black line represents a random distribution; points above the black line are clustered and points below are ordered. The vertical scale varies between figures.

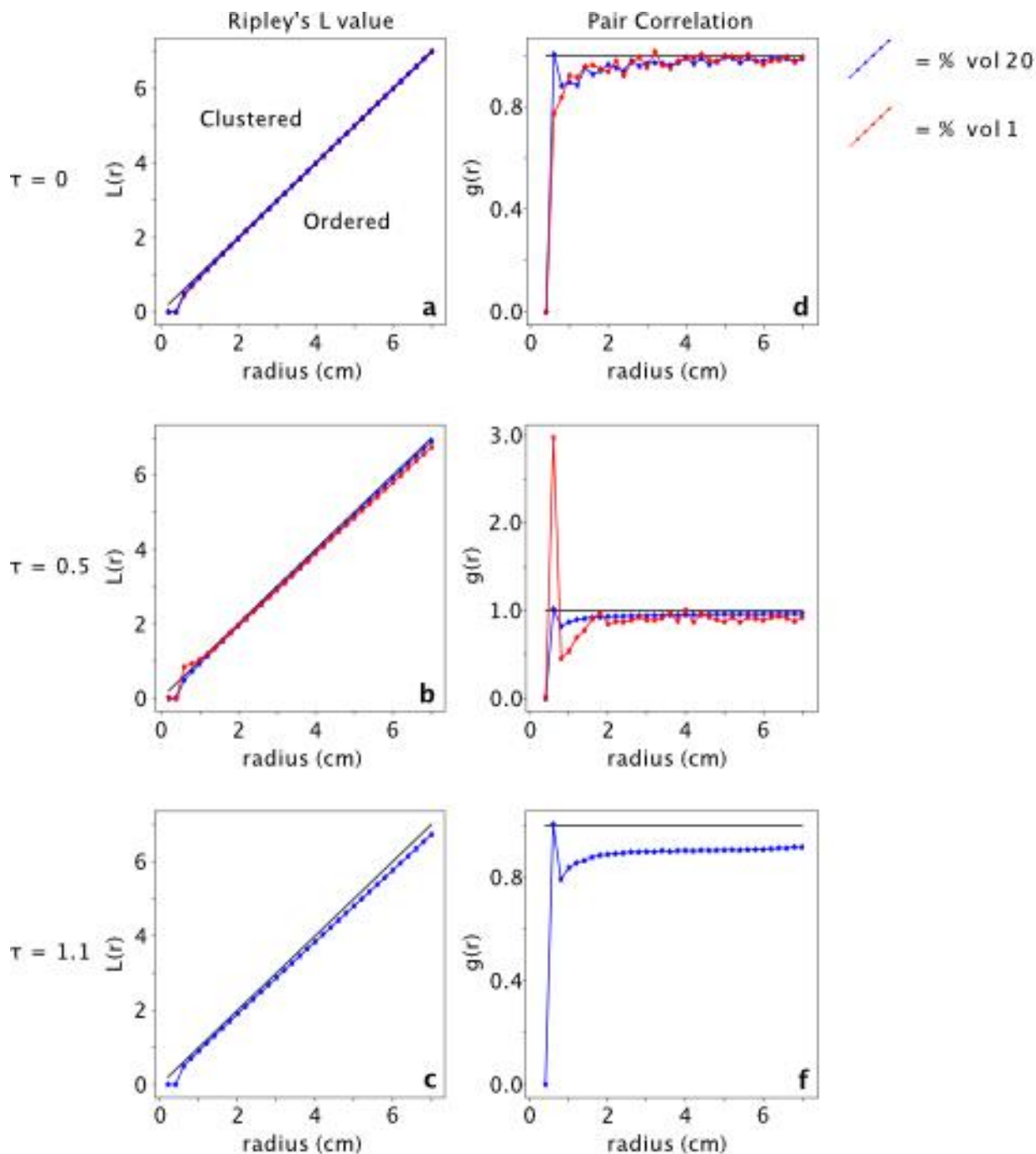


Figure 2.5. Ripley's L value (a-c) and pair correlation (d-f) functions of the open system models (OSM) for a solid volume fraction of 1% and 20%. The one percent OSM is represented by the

red lines and the 20% OSM is represented by the blue lines. The vertical scale varies between figures.

assesses the likelihood that a particle center will be found at or near a specific radial distance of the randomly selected particle center.

The $g(r)$ function is shown on the right-hand side of figures 2.4d,e,f and 2.5d,e,f with the same systems considered as in the $L(r)$ value as in figure 2.4a,b,c and 2.5,a,b,c. As with the $L(r)$ function, the mean value of $K(r)$ was used to calculate the results for the $g(r)$ function giving the average behaviour of the system. Similar to the $L(r)$ function, the results of the $g(r)$ function do not significantly differ between the first two $\tau = 0, .5$ in figure 2.4a,b. However, there is a difference at $\tau = 1.1$ figure 2.4f; the OSM strongly tends to an ordered distribution, while the SM maintains a near-random distribution.

The OSM 1% and 20% initial particle fraction systems in figure 2.5d have similar pair correlations at the initial time step; both start ordered but tend to spatial randomness with increasing radial distance. At $\tau = 0.5$ in figure 2.5e the 1% system starts in the clustered regime, drops to ordered and then converges to random, while the 20% system starts in the ordered regime and converges to spatially random with distance. At $\tau = 1.1$, figure 2.5f the 20% system starts in the ordered regime and tends towards spatial randomness.

2.3.2 *Voronoi tessellation as a measure of clustering*

Voronoi diagrams are a method to quantify clustering: local cluster size, location and cluster orientation. In the two-dimensional case, Voronoi tessellations are polygons where the area of the polygon is the portion of the domain where the closest particle center is the particle within the Voronoi polygon (Ferenc & Néda, 2007). Hence the size and orientation of the polygon is determined by the particle distribution. Figure 2.6b,c are examples of a Voronoi tessellation from

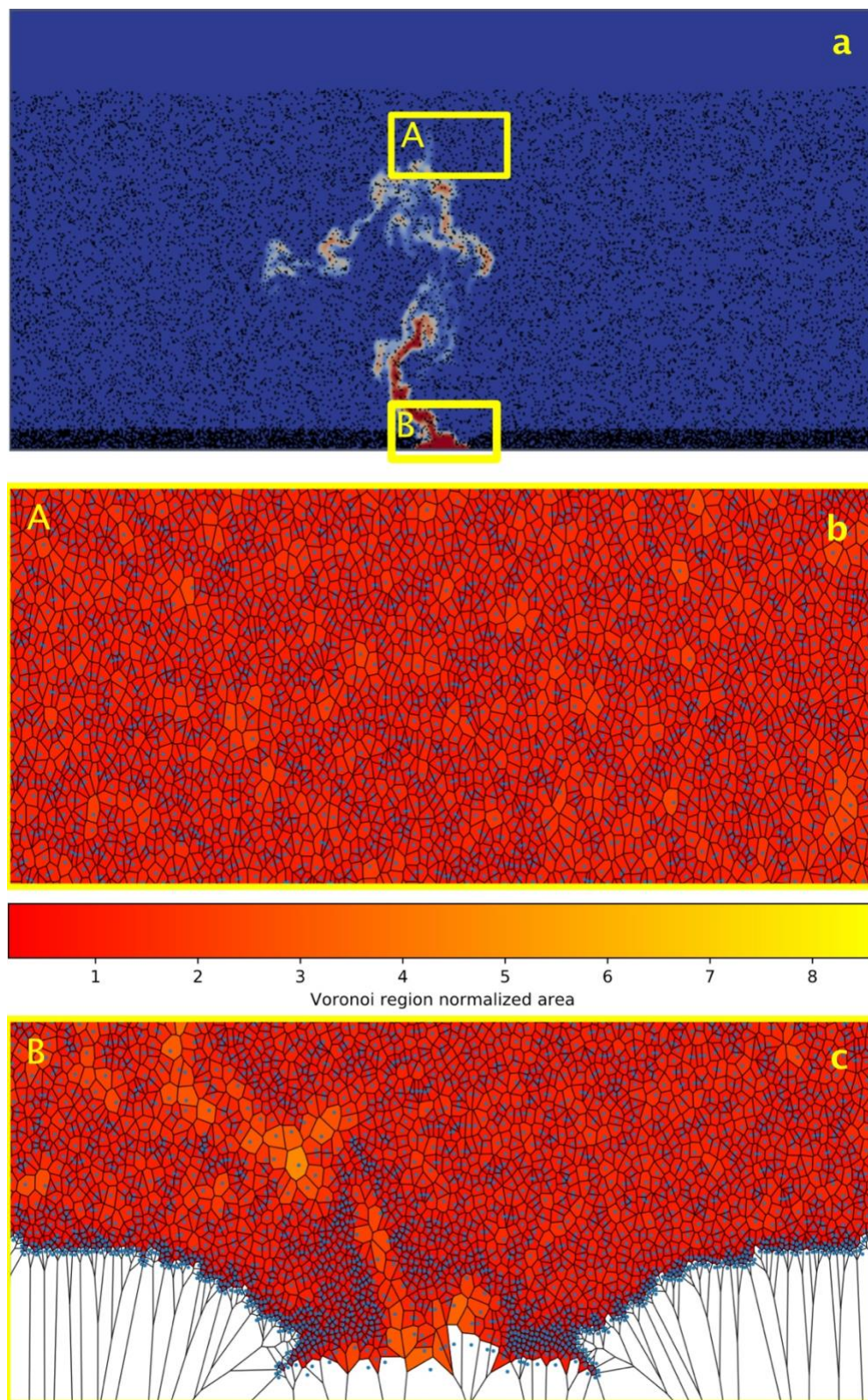


Figure 2.6. Open system model for $\tau = 0.3$ and Voronoi tessellation for two regions of the settling particles. (a) Snapshot of OSM $\tau = 0.3$ with regions A and B highlighted. (b) Voronoi tessellation

for region A. This region was chosen above the new fluid injection site but near the shock front. (c) Region B covers the new fluid injection site. The Voronoi polygons are colored by polygon area normalized to the mean Voronoi polygon area of a random distribution. An area of 1 indicates a random Voronoi polygon size, areas larger than 1 indicate ordering, and areas smaller than 1 indicate clustering.

the OSM 9% solid volume fraction simulation. The Voronoi polygons are coloured by normalized area. Normalization was achieved by dividing each Voronoi polygon area by the mean Voronoi polygon area of a continuous uniform random distribution of particles, using the same number of particles and area. Particles and their Voronoi polygons around the edges are not included in the calculations below to avoid edge effects. Since we are not interested in clustering associated with the static settled bed, all particles that are in fluid cells with a solid volume per cent greater than 46% were removed.

Two regions of the settling regime are highlighted in figure 2.6. Region A is the Voronoi tessellation near the sedimentation shock and region B is the Voronoi tessellation at the mixing bowl. Voronoi polygons in inset A are mostly the same size, as seen by the uniform colour in figure 2.6b, with a value close to that of the mean polygon area of a continuous uniform random distribution (MCURD). The Voronoi polygons in figure 2.6c (inset B) are heterogeneous, and are both larger and smaller than MCURD. The sides of the mixing bowl are composed of Voronoi polygons that are smaller than MCURD, while the centre has regions that are larger than MCURD. The settling interface between the settled bed and the particles still settling are Voronoi polygons that are smaller than MCURD.

2.3.2.1 Voronoi polygon area

The Voronoi polygon area can also be used to determine if the distribution of the system is random, clustered, or ordered. Figure 2.7a-d are probability density functions (PDF), which are a type of histogram, from the settling system (SM) and the open-system (OSM) for $\tau = 0, 0.5,$ and 1.1 . $\tau =$

0 is used as a reference for our initial state and is compared on each plot along with an idealized random curve from an equation in (Ferenc & Néda, 2007):

$$f(a) = \frac{343}{15} \sqrt{\frac{7}{2\pi}} a^{\frac{5}{2}} e^{\frac{7}{2}a} \quad (2.13)$$

where a is the normalized area of a random distribution of similar particles and area. The starting condition for the system differs from the truly random curve from (Ferenc & Néda, 2007) in that the PDF has a greater maximum value but a smaller range of Voronoi polygon area. In figure 2.7a, for SM where $\tau = 0.5$, there is a reduction in the range of Voronoi polygon area, but little change in the maximum value or location of the PDF. The OSM case in figure 2.7b is similar, indicating that at this time there has been no significant expression of clustering relative to the initial distribution.

In figure 2.7b,d, for $\tau = 1.1$, the PDF approaches that of the Ferenc & Néda idealized random curve (Ferenc & Néda, 2007) indicating a shift to a more spatially distribution of particles. There are two peaks in the PDF, both around 1.

2.3.2.1 Voronoi region aspect ratio

The Voronoi polygon area combined with the Voronoi tessellation of the simulation, figure 2.6, provides insight into distribution and magnitude of clustering. Adding information about the aspect ratio and orientation of the aspect ratio provides additional insights into the kinematic conditions associated with the creation of the clusters. Voronoi polygon aspect ratios were used in Uhlmann and Doychev (2014) to determine if clustering was being produced by synneusis (settling particles). In their study they used the longest horizontal distance relative to the longest vertical distance to calculate the aspect ratio. It was found in Uhlmann and Doychev (2014) that a horizontal stretching of the aspect ratio indicated vertical particle clustering through settling.

Having only the horizontal or vertical component is sufficient when working with a purely settling system, but when considering a more complex system with settling and open-system flow, Voronoi polygon aspect ratio orientations that are oblique to the vertical or horizontal are required.

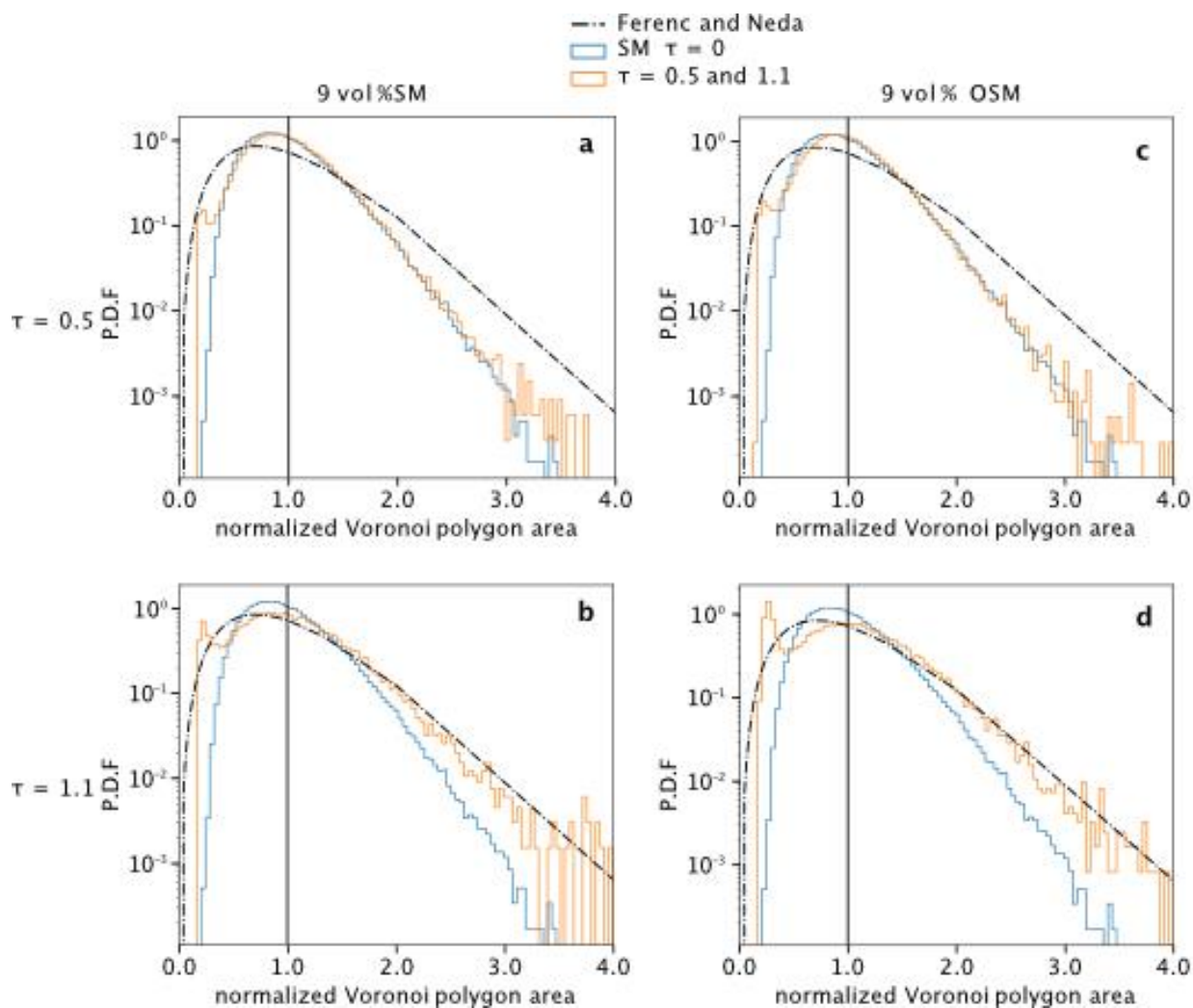


Figure 2.7. Voronoi polygon area histogram for the settling model (SM) (a,b) and the open system model (OSM) (c,d) at 9% particle volume fraction. The area of each polygon is normalized to the mean area of Voronoi polygons for a continuous uniform random particle distribution. The black chain line shows the ideal random distribution as set forth by Ferenc and Neda (2007), the blue line is the histogram from $\tau = 0$ of the SM and the black vertical line indicates unity. The vertical scale varies between figures.

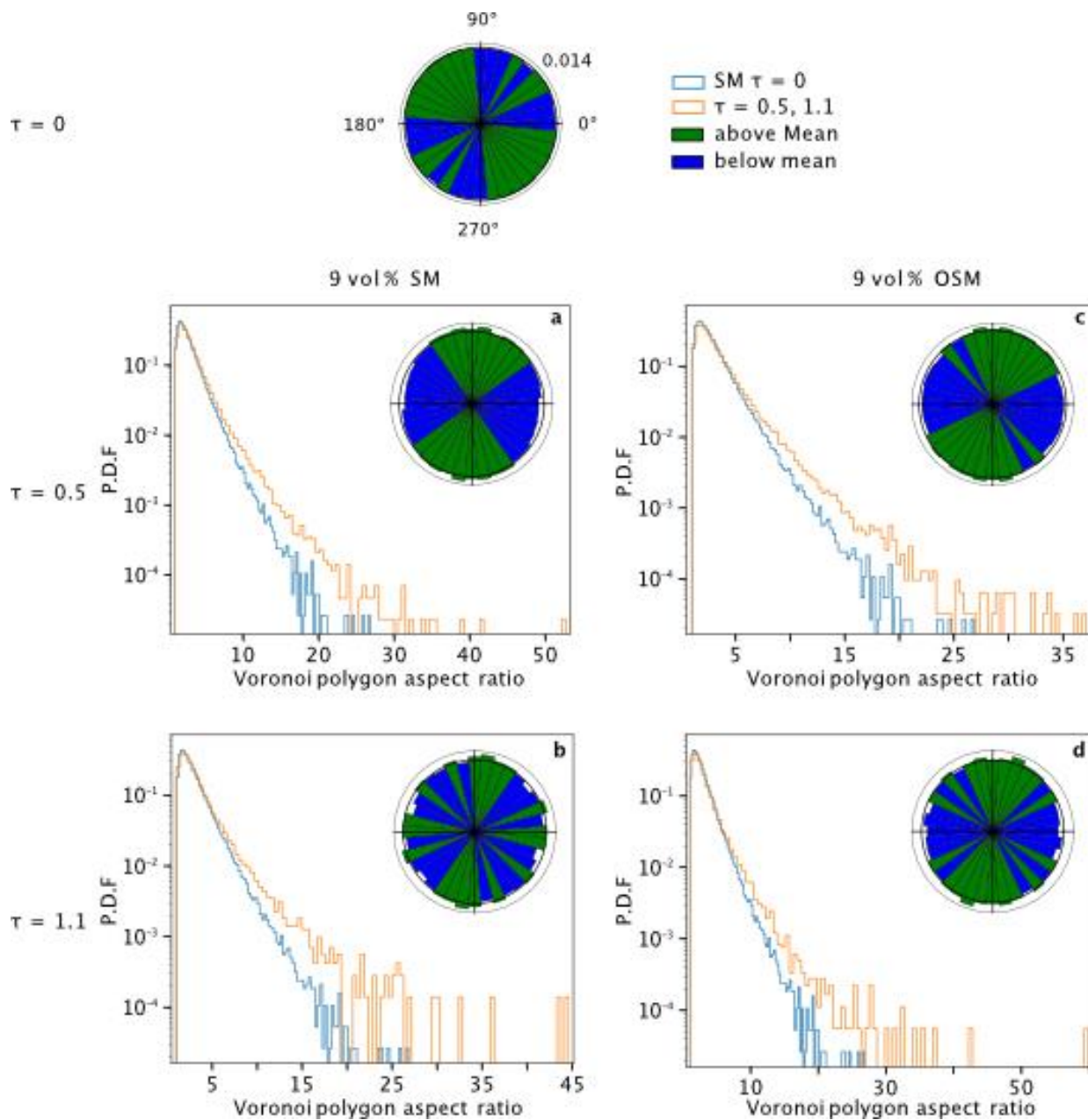


Figure 2.8. Voronoi region aspect ratio for the settling model (SM) (a,b) and the open system model (OSM) (c,d) at 9% particle volume fraction. The blue histogram is the aspect ratio histogram for $\tau = 0$ of the SM and the orange line is the named system. The rose diagram imbedded in the right corner of each plot shows the orientation of the long axis of the aspect ratio. The green bins are above the mean height of the bins and the blue bins are below the mean height. The rose diagram for $\tau = 0$ has the orientations displayed as well as the value of the inner black circle. Vertical scale for the probability density functions varies between figures.

To obtain the aspect ratios of the Voronoi polygons we used eigenvectors calculated using a variance/covariance matrix by using the position of the vertices of each region. The eigenvectors

were used as proxies for the aspect ratio of the Voronoi polygons. All aspect ratios are calculated by the long axes length divided by the short axes length. In figure 2.8 the long axis is shown on a rose diagram, to illustrate orientation data. Each bin represents 10 degrees, so there are 36 bins per rose diagram. Figures 2.8a,d are the PDF of the aspect ratios and rose diagrams of the Voronoi polygons. The mean of the bins was calculated, and the colours indicate if the value of the bin is above or below the mean. In the figure, green represents above the mean and blue represents those below the mean. Values equal to the mean are displayed with those values below the mean.

The initial condition, $\tau = 0$, is shown in the top rose diagram and is the blue curve in all PDF's in figure 2.8a-d. There is an increase in Voronoi polygon aspect ratio to the initial condition in both the open and settling systems and for $\tau = 0.5$ and 1.1 indicating stretching of the Voronoi polygons. The rose diagram for the initial condition represents our random distribution. Even though the bins are coloured according to their value above or below mean, the bins all have values close to mean. For $\tau = 0.5$ there is a preferred orientation of the Voronoi polygons towards the vertical for both the open and settling systems. In figure 2.8d, the open system for $\tau = 1.1$ the vertical preferred orientation is maintained, although slightly oblique, but in figure 2.8c, the settling system there is a horizontal and an oblique preferred orientation.

2.4 DISCUSSION AND CONCLUSIONS

We have demonstrated the application of a number of measures that express particle clustering at different scales. The R value produces a single clustering metric at the domain length scale and so express a system wide tendency to order or randomness. The probability density functions of the Voronoi tessellations express a distribution of cluster sizes based on a closest neighbour criterion, as well as statistics of tessellation anisotropy which is a qualitative expression of the kinematic

state of the flow. The $L(r)$, and pair correlation functions express an average of particle distribution as function of distance.

We first consider the conditions of the settling only (SM) simulation with initially nine volume percent crystals that are randomly distributed. At $\tau = 0.5$ (figure 2.7a, 2.8a) there is no significant change in the clustered state of the system. However, at $\tau = 1.1$ (figure 2.7c, 2.8c) there has been an increase in clustering. This change cannot be ascribed to the processes of KDT referred to in section 1c, as the Galileo number for the system (equation 2.1) is approximately 5, which is a factor of 25 smaller than that which would produce wake unsteadiness. Since virtually all conditions of settling in magmas will have very low Galileo numbers this process is unlikely to be important in producing clustering in magmas. The observed clustering can be attributed to the combined effects of "hindered settling" or crowding from the increase in the solid volume per cent in the remaining liquid producing the formation of local fluid channels from the upward-directed fluid return flow. This in turn produces a corresponding local increase in particle volume per cent. Thus we expect that clustering from sedimentation alone will be most prevalent in regions near the floor or settling capture-front, where hindered settling enhances particle crowding, which produces a complex return flow and particle transport enhancing clustering.

The combined settling and open-system simulations (OSM) show a more complex pattern of particle transport. Figure 2.6a shows the initial nine volume percent particle simulation at a time of $\tau = 0.3$. Figure 2.6b is the Voronoi tessellation of inset A that is the portion of the system largely dominated by particle sedimentation, while figure 2.6c is an inset of the lower portion. This figure illustrates two points in the quantification of clustering, firstly that in a dynamic system any bulk metric of clustering as described in section 3a, will include many scales of heterogeneity and thus may not predict or recover the clustering on a geological sample of size less than the system size.

The second point is expressed by figure 2.6c, centered on a region of strong upwelling. This clearly shows the role of fluid-particle interactions, producing fluid-rich core region surrounded by a ring or tube of enhanced clustering around the upwelling. Above that extensional flow produces a region with a reduced number of particles. Collectively this is similar to the complexity of mixing, more properly called dispersion, discussed in (Schleicher et al., 2016) where a bulk index of mixing (dispersion) suggested good mixing, but a local characterization exposed distinct domains of heterogeneity. This is also expressed by comparison of figures 2.8b and 2.8d. Despite the presence of the flow associated with the new magma input transporting the crystals, there is not a significant difference in the bulk Voronoi polygon aspect ratio. But there is a significant difference in the orientation of the polygons, with a significant contribution to the vertical orientation indicating the presence of an extensional kinematic template (horizontal flattening).

Examination of figures 2.7b and 2.7d at $\tau = 1.1$ leads one to the non-intuitive result that based on bulk measures only, pure settling can produce more clustering than a system with settling and stirring. This reflects the dual nature of open system stirring, particles are gathered by fluid motion into regions where the local particle per cent exceeds any that might result from simple settling, but at the same time the extensional elements of the fluid flow disperse particles and prevent them from settling. This is in part expected given the values of the Stokes number (equation 2.5) and settling factor (equation 2.6) discussed in section 1c. For our simulations the Stokes number is $O(10^{-4})$ and the settling factor $O(10^{-1})$, thus if there is fluid motion associated with open-system input the particles will become almost passive tracers, with a minor 'drift flux' velocity associated with the steady acceleration of gravity. Thus, clustering in open systems is difficult to generalize and dependent on the details and duration of open system stirring.

While it is desirable to compare the general trends obtained from the numerical experiments directly with natural examples, we don't currently have access to sufficiently characterized geological samples. However natural examples do reflect some of the general features seen in figures 2.7 and 2.8, and we briefly describe one example below.

Plagioclase cluster formation in the Holyoke basalt has been explained as a multistage process involving settling and compaction with a role for upward flow of interstitial melt to act as a source of possible vertical mixing (Jerram et al., 2003; Philpotts et al., 1998; Rudge et al., 2008). We would expect that the cluster distribution in the marginal chill would act as an initial reference, in the same way that the Ferenc and Nédá (2007) distribution did in this study. The middle unit, which underwent some compaction, might yield Voronoi tessellations with a preferred orientation, with the Voronoi polygons having a similar orientation to the plagioclase chains. If upward flow associated with the compaction from the mush was vigorous enough cluster formation might produce a distribution like that of the OSM in figure 2.7c,d.

Chapter 3. ON THE DYNAMICS OF MAGMATIC GRAVITY CURRENTS

3.1 INTRODUCTION

The development of the "magma mush" paradigm for magmatic systems requires new elements of description for the mechanics of magmas that are appropriate for crystal-rich conditions (Bachmann & Bergantz, 2004; Ferguson et al., 2019; Holness et al., 2019; Klemetti, 2016; Lissenberg et al., 2019; Paterson et al., 2019). In addition, observations of crystal zoning and mineral fabric from both plutonic and volcanic systems, and the relatively rapid timescales of magma mixing, thermochemical rejuvenation and melt extraction, requires a significant amount of mobility under crystal-rich conditions (Ardill et al., 2020; Bennett et al., 2019; Passmore et al., 2012; Roelofse & Ashwal, 2012; Wolff et al., 2020). Magmas manifestly have a dual nature: they can be crystal-rich under conditions near random close packing, but also exhibit remarkable mobility and complex mixing (Schleicher & Bergantz, 2017; Wiebe et al., 2017). Hence the traditional proposition that magmas are a simple multiphase suspension with a single value of crystal jamming or "lock up," is not consistent with the diversity of observations and time scales recovered from natural examples. A description of magma dynamics requires that both viscous and granular stresses be resolved, hence the system is inherently hydrogranular, yet there has been very little research on the detailed physics of hydrogranular systems under magmatic conditions to guide the interpretation of natural examples (Bergantz et al., 2017; Carrara et al., 2020; Culha et al., 2020; Petford, 2009; Petford & Koenders, 1998; Petford et al., 2020; Qin & Suckale, 2020).

Previous efforts to address the multiphase nature of magma physics were initially with multfluid mixture theory, where the system is assumed to be represented by interpenetrating continua (Eulerian-Eulerian), each of which was described by some averaging scheme with

interface exchange terms (Bergantz & Ni, 1999; Dufek & Bergantz, 2007; Ruprecht et al., 2008). However this approach is not able to capture the complex nature of jamming and the onset of friction, nor can it resolve specific crystal (Lagrangian) paths as an aid to the interpretation of crystal chemical zoning, and the constitutive framework is based on ad hoc assumptions about granular stresses that are not well recovered in Paterson rig type lab experiments (Picard et al., 2013). The obstacle arises in the continuum rheological closures, where the dissipation is assumed to be dominated by viscous or plastic flow laws. In continuum mechanics the local strain is assumed to be a continuous function of the coordinates and is defined by the displacement gradient at a given point. But in crystal-rich materials the particles are not the volume elements of a continuum. The strain is non-affine and non-local and the rheology of granular materials is not governed by a single length scale. Hence the multifluid, or multi-continuum approach is limited in the scope of physical processes it can resolve.

Tank and flume experiments have been used to illustrate magmatic and eruptive processes such as might occur in dry pyroclastic gravity currents (Delannay et al., 2017; Dufresne, 2012; Estep & Dufek, 2012; Farin et al., 2014) or immersed conditions (Castruccio et al., 2010; Forien, Tremblay, Barnes, Burgisser, & Pagé, 2015). The skeletal, nonhydrostatic distribution of force on a scale larger than the particle size was firmly established by experiments with optically sensitive discs (Behringer et al., 1999; Dantu, 1957) and 3-D X-ray diffraction (Hurley et al., 2016). These observations were rationalized with the notion of particle “force chains” (Antony, 2007). While there is no singular definition of a force chain, it is generally understood as being a colinear arrangement of at least three particles carrying more than the mean force, and typically has a length of up to 10 particles (Cates et al., 1998; P. Guo, 2012; Muthuswamy & Tordesillas, 2006; Peters et al., 2005; Wambough, 2010). The fundamental topology of a force chain is that it typically

branches, forming arches, and transmitting force oriented around some mean at the macroscale. During deformation the force chains migrate as percolating networks on a time scale approximately the inverse of the shear rate, where abandoning existing force chains and the recruitment of particles that were previously spectators into new chains discontinuously transmits force.

While these experiments were essential for identifying the distinct large-scale kinematic states and the skeletal nature of force distribution, they were incapable of providing any quantitative information on the microstructure: the emergent granular and fluid stresses internal to the flow. The application of the discrete element numerical method (DEM) where each crystal (or particle, we will use those terms interchangeably) is explicitly resolved provides an opportunity to quantify the fluctuating grain-scale stresses and local particle transport (Ai et al., 2014; Deen et al., 2007; Estep & Dufek, 2013). The numerical experiments act as a probe of the micromechanics and allow for the quantification of particulate mixtures in unprecedented detail, much of which is summarized in a number of texts and review papers (Andreotti et al., 2013; Campbell, 2006; Forterre & Pouliquen, 2008; Franklin & Shattuck, 2015).

Our goal in this contribution is to employ the discrete element method for calculating particle stresses and trajectories coupled with a transport solver for the fluid phase, a Eulerian-Lagrangian approach. We will use this numerical framework to evaluate and exemplify three distinct regimes for the behavior of crystal-rich magmatic gravity currents, all sharing a common initial condition. The goal is not to portray any particular realistic magma system, but instead a generic magma system of wide application. Our aim is to provide a quantitative basis for the interpretation of diverse natural examples, and we will do this by consideration of both the large-scale features of the flow as well as the microstructures.

3.2 THE 'DAM BREAK' SCENARIO AS A PROXY SYSTEM FOR MAGMATIC DENSITY CURRENTS

The dynamic template we employ for investigating magmatic gravity currents is the canonical 'dam break' or 'lock exchange,' set-up. In this scenario a column of particles is placed at rest in a half space, on one end of a planar (but possibly rough) surface that is either flat or tilted. The volume of particles is suddenly released with no other source of induced motion. The system responds with the gravitational collapse of the particles, which eventually comes to rest as a result of frictional interactions with other particles and the base, and if a fluid is present by dissipation from drag. While simple in concept, this set-up has proven to be a very useful framework for revealing the feedback from particle-particle-fluid interactions and the associated mesoscale emergent length and time scales (Ancey et al., 2013a, 2013b; Girolami et al., 2012; Mutabaruka et al., 2014; Pailha et al., 2008; Topin et al., 2012).

It is well established that one of the fundamental characteristics of hydrgranular flow is Reynold's dilatancy (Reynolds, 1885). When a granular media is sheared it will initially dilate as particles are forced to move over and around each other to accommodate the applied stress. If a fluid is present a feedback is induced as the expansion of the particle packing tends to develop negative excess pressure in the pore space, influencing the deformation. This leads to a competition during collapse between initial particle packing and hence permeability, and fluid viscosity which can substantially impact the progress of particle motion. The viscosity of silicate melts can vary orders of magnitude and can be quite high, yet the role of melt viscosity and the initial conditions of a particle mush in controlling the behavior of magmatic density current is not generally understood. The purpose of the simulation below are simplified relative to natural conditions to

illustrate how these feedbacks can create distinctly different dynamic regimes and deposits in the geological record.

3.2.1 Theory

In order to capture the dynamics and interactions of the granular flow on the micro level, the system is modeled with the Lagrangian-Eulerian (LE) method. In the LE method the fluid is treated as a continuum while the particles are treated as discrete elements known as the Discrete Element Method (DEM) (Garg et al., 2012b; T. W. Li et al., 2012). The volume elements on which the fluid is resolved is typically a few particles. MfiX-DEM has been validated and verified (Garg et al., 2012b; T. W. Li et al., 2012), which is discussed below.

MfiX-DEM approaches LE modeling in two steps; the first is the continuity and momentum conservation equations for the liquid-phase which considers drag on the fluid from the particles. The continuity and momentum equations are:

$$\frac{\partial(\epsilon_l \rho_l)}{\partial t} + \nabla \cdot (\epsilon_l \rho_l v_l) = 0. \quad (3.1)$$

and

$$\frac{D}{Dt}(\epsilon_l \rho_l v_l) = \nabla \cdot \bar{\bar{S}}_l + \epsilon_l \rho_l g - \sum_{m=1}^M I_{lm}. \quad (3.2)$$

In both equations ϵ_l is the gas volume fraction, ρ_l is the density of the liquid-phase, and v_l is the volume averaged liquid-phase velocity. For the conservation of momentum equation I_{lm} is the term for momentum transfer between the liquid-phase and the m^{th} solid-phase, and $\bar{\bar{S}}_l$ is the liquid-phase stress tensor (Garg et al., 2012b).

The second method is the treatment of the solid-phase. MFiX-DEM solves the Newtonian equations for position and both linear and angular velocities. The evolution of the particles position, linear velocity and angular velocity are represented by the following equations (Garg et al., 2012b):

$$\frac{dX^{(i)}(t)}{dt} = V^{(i)}(t), \quad (3.3)$$

$$m^{(i)} \frac{dV^{(i)}(t)}{dt} = F_T^{(i)} = m^{(i)} g + F_d^{i \in k.m}(t) + F_c^{(i)}(t) + F_\lambda^{(i)}(t), \quad (3.4)$$

and

$$I^{(i)} \frac{d\omega^{(i)}(t)}{dt} = T^{(i)}. \quad (3.5)$$

Particles are represented in the Lagrangian frame by $\mathbf{X}^{(i)}$, $\mathbf{V}^{(i)}$, and $\boldsymbol{\omega}^{(i)}$. Where (i) represents the i^{th} particle and \mathbf{X} is the position, \mathbf{V} is the velocity, and $\boldsymbol{\omega}$ is the angular velocity. The total force on the i^{th} particle is represented by $F_T^{(i)}$, $F_d^{i \in k.m}$ is the drag force of the i^{th} particle in the k^{th} cell and belonging to the m^{th} solid-phase, $F_c^{(i)}$ is the contact force that is a result of contact with other particles, and $F_\lambda^{(i)}$ is the lubrication force between two particles. $\mathbf{I}^{(i)}$ is the moment of inertia on the i^{th} particle, and $\mathbf{T}^{(i)}$ is the total sum of all torques acting on the i^{th} particle.

Particle-particle and particle-wall collisions are modeled using the soft sphere approach, which is based on the spring-dashpot model (Garg et al., 2012b). The overlap between colliding inelastic particles is represented by a spring and dashpot where the rebound is caused by the spring, and the dissipation of kinetic energy is caused by the dashpot. The spring stiffness determines the particle overlap during collision, however, a large value for spring stiffness decreases the contact time, increasing the computation time (Garg et al., 2012b). Damping effects of the dashpot are

related to the coefficient of restitution (Garg et al., 2012b), which is the ratio of the velocity after collision to the velocity before collision. A coefficient of restitution valued at 1 would have no change in the velocity due to collision - thus no dampening - and the particles would behave as purely elastic. When considering particles submerged in a fluid, lubrication forces dampen particle collisions (Bergantz et al., 2017). Lubrication forces are not specifically modelled but can be mimicked by setting a low coefficient of restitution (Bergantz et al., 2017; Carrara et al., 2019). Both of our simulations use a value of 0.9 for the coefficient of restitution.

3.2.2 *Simulation parameters*

The initial condition is a polydisperse particle column with a porosity of approximately 0.482 that is saturated in a viscous fluid (fig. 3.1). The column is composed of three different particle sizes

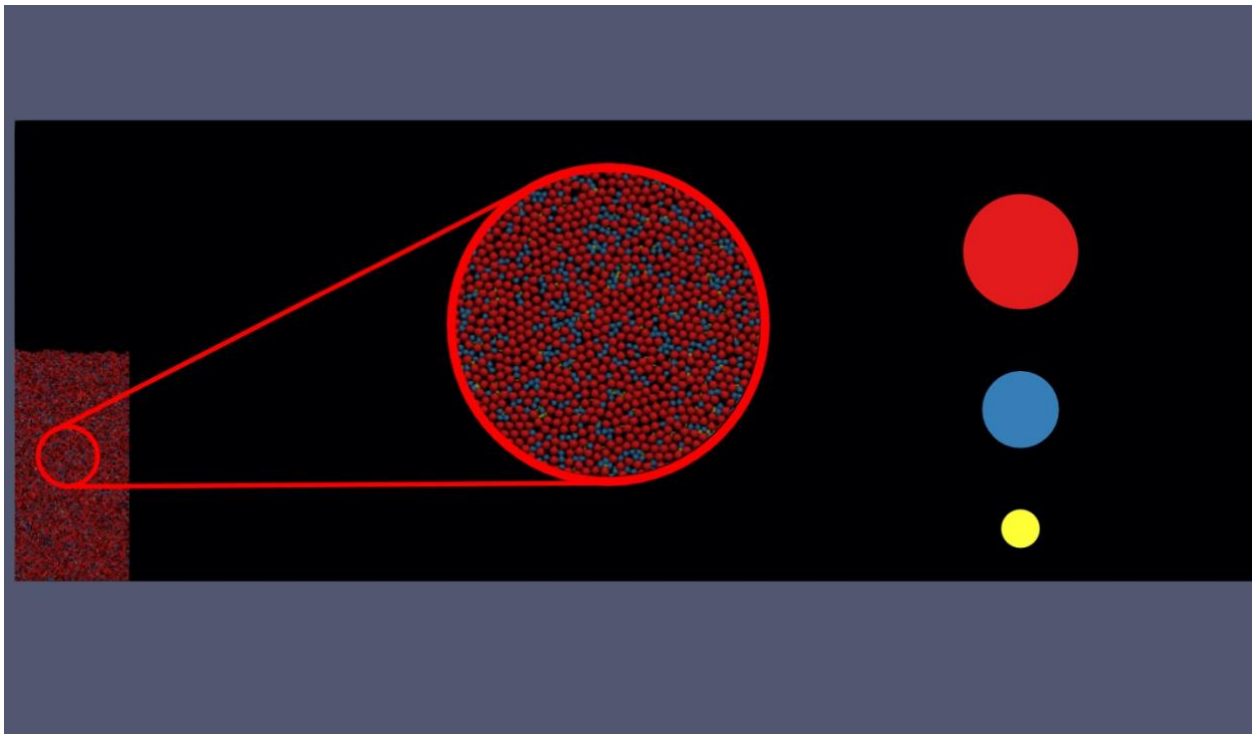


Figure 3.1. Initial condition of the dam break scenario before the domain is tilted. The red particles simulate plagioclase, the blue particles simulate olivine/pyroxene, and the yellow particles simulate magnetite. See table 3.1 for particle properties.

and densities as given in table 3.1. The fluid has a density of 2.65 g/cm^3 and a viscosity of 1 Pascal second. The particle column is two dimensional with a height of 0.64 m and a width of 0.32 m.

A column thickness of 0.006 m was used for the simulations which matches the diameter of the largest particle; the thickness of the column allows for spherical particles while maintaining a $2d$

Table 3.1. Particle properties

	Number of Particles	Particle Diameter (m)	Particle Density(kg/m^3)
Plagioclase	4876	0.006	2750
Olivine/Pyroxene	2438	0.004	3300
Magnetite	813	0.002	518
Total	8127		
Average		0.005	3158

configuration. The overall simulation domain is 5.12 m by 2.56 m that has a grid cell size of $1 \times 10^{-4} \text{ m}^2$. To initiate column collapse under gravitational forcing the bed is tilted 16 degrees.

We employ the use of two friction coefficients (0.1 and 0.58) in our models to explore the effect friction has on the kinematics of the collapse and runout. These friction coefficient values were chosen to produce the end member results of a flow that will continue to advance down the slope and one that eventually stall.

3.2.3 *Scaling*

The application of the simulation requires the identification of global scales. The particle velocity is scaled to the Stokes' settling velocity, time is scaled to the time it takes a single particle to settle

the height of the particle column, and kinetic energy is scaled to the potential energy of a particle positioned at the top of the column.

Particle velocity is obtained from the simulation data, but the scaling needs to be natural scales that can be known before the simulation results. The following three equations obtained from Chen and Zhang, (2008) are used to find the Stokes' settling velocity:

$$U = \sqrt{\frac{4gD(\rho_c - \rho_m)}{3\rho_m C_D}} \quad (3.6)$$

where

$$C_D = \frac{24}{Re} (1 + 0.15Re^{0.687}) + \frac{0.42}{1 + 42,500Re^{-1.16}} \quad (3.7)$$

and

$$Re = \frac{DU\rho_m}{\eta} \quad (3.8)$$

Here Re is the Reynolds number, D is the diameter of the particles, U is the Stokes' settling velocity, ρ_m is the fluid density, η is the fluid dynamic viscosity, g is gravitational acceleration, ρ_c is the particle density, and C_D is the drag coefficient. Because the particles are polydisperse the average diameter and density of all the particles in the column were used in the calculations.

When calculating kinetic energy, the average mass and velocity of the particles at center mass is used.

$$Ke = \frac{mV^2}{2} \quad (3.9)$$

In this equation m and V are the average mass and velocity of the particles at center mass. Because the height of the column is the only natural scale in the system, potential energy is calculated considering a particle that has a mass of the average mass of all the particles in the column at the height of the particle column.

$$Pe = MgH \quad (3.10)$$

M is the average mass of all the particles in the column and H is the height of the column.

To scale time, the time it would take a single particle to settle the height of the particle column is used.

$$\tau = \frac{t}{t^*}, t^* = \frac{H}{U} \quad (3.11)$$

Using this scaling allows for a comparison of the collapse and runout of the particle column to the Stokes' settling time of a single particle. Contact forces are scaled by the average force at each timestep, $\langle F \rangle$.

3.3 MICRO AND MESOSCALE DESCRIPTIONS OF GRAVITY CURRENTS

In the following sections we employ micro and mesoscale descriptions of the evolving forces and contact fabric to illuminate the controls that produce distinct gravity current behavior.

3.3.1 *Force chains and microstructures*

As discussed in the introduction, a granular media distributes force through a heterogeneous network of force chains (Kruyt, 2016; Peters et al., 2005). Unlike a fluid, granular materials transmit forces through contacts (Kruyt, 2016; Peters et al., 2005). An example of force chains in spherical particles can be seen in Figure 3.4a. The force is distributed in filament like chains

(Majmudar & Behringer, 2005), where it has been observed that force is not homogeneous or hydrostatic throughout the granular media (Majmudar & Behringer, 2005). Only the forces that are greater than average and extend through at least 3 particles are considered to be force chains (Peters et al., 2005). The chains build arching structures where orientations will vary around the orientation of the maximum compressional stress. Hence, two elements of description of force transmission are required: the orientation of the contact and the orientation of the force acting on that contact (Kruij, 2016). Both the contact fabric and the force chain fabric can be quantified through use of fabric tensors and Eigenvalues (Kruij, 2016)

The force and contact fabrics cannot typically be obtained from analog experiments, but numerical experiments provide all contact information for every particle. Under steady conditions the force chains tend to align with the principle (compressive) stress direction (Kruij, 2016), but will align at a 45° angle from the shear direction (Utter & Behringer, 2004). The anisotropic orientations of the force and contact fabric are obtained from the model and plotted on a rose diagram. The orientations from the rose diagram are used to find a second rank fabric tensor, F_{ij} .

$$F_{ij} = \frac{1}{N} \begin{bmatrix} \sum_{k=1}^N \cos \theta^k \cos \theta^k & \sum_{k=1}^N \cos \theta^k \sin \theta^k \\ \sum_{k=1}^N \sin \theta^k \cos \theta^k & \sum_{k=1}^N \sin \theta^k \sin \theta^k \end{bmatrix}. \quad (3.12)$$

The anisotropy index is found by the equation:

$$a_c = 2 \frac{F_1 - F_2}{F_1 + F_2}, \quad (3.13)$$

and θ_c is the eigenvector orientation of the larger eigenvalues found from the force and contact rose diagram distributions.

$$\theta_c = \frac{1}{2} \arctan \left(\frac{F_{12} + F_{21}}{F_{11} - F_{22}} \right) = \frac{1}{2} \arctan \left(\frac{\sum_{k=1}^N \sin 2\theta^k}{\sum_{k=1}^N \cos 2\theta^k} \right) \quad (3.14)$$

A curve is fit to the rose diagram using a second order expansion that is representative of the contact and force distributions.

$$E(\theta) = \frac{1}{2\pi} [1 + a_c \cos 2(\theta - \theta_c)] \quad (3.15)$$

3.3.2 *Column collapse and runout*

The following sections will describe the column collapse of both simulations. The column collapses by two distinct methods that develop into three distinct kinematic flow regimes.

3.3.2.1 Initial condition and particle dilation

The simulation is initiated by tipping the domain to 16 degrees. The granular column is no longer statically stable and responds by progressive collapse. As the particles at the edge of the column begin to separate from the core and fall, a negative pore pressure develops as they separate from neighboring particles. This creates a type of pseudo-yield strength as fluid resists being pulled into the pore space, a type of lubrication process (Mutabaruka et al., 2014). This creates a transient where wholesale collapse is inhibited, and instead progresses as distal particles escape the virtual cohesion from lubrication.

The force chains at the start of the simulation (fig. 3.4a) reflect the initial gravitational loading of the column during the initial condition and have an isotropic orientation with a natural bias to greater values deeper in the particle column. As the particles begin to separate at the start of collapse the bulk coordination number, the average number of particle-particle contacts for each particle within the granular system, drops with a corresponding rearrangement of the force chains.

3.3.2.2 Collapse regimes and runout kinematics

When the particles overcome the negative pore pressure they begin to collapse and develop into two collapse regimes (fig. 3.2b). On the top right corner of the column the particles undergo the most dilation and form a progressive toppling collapse. Simultaneously the core of the column starts to bulge and granular fault, or discrete shear zone forms from the bottom right corner to the upper left corner of the column. This fault separates the mobile core from the quasi-static base of the column.

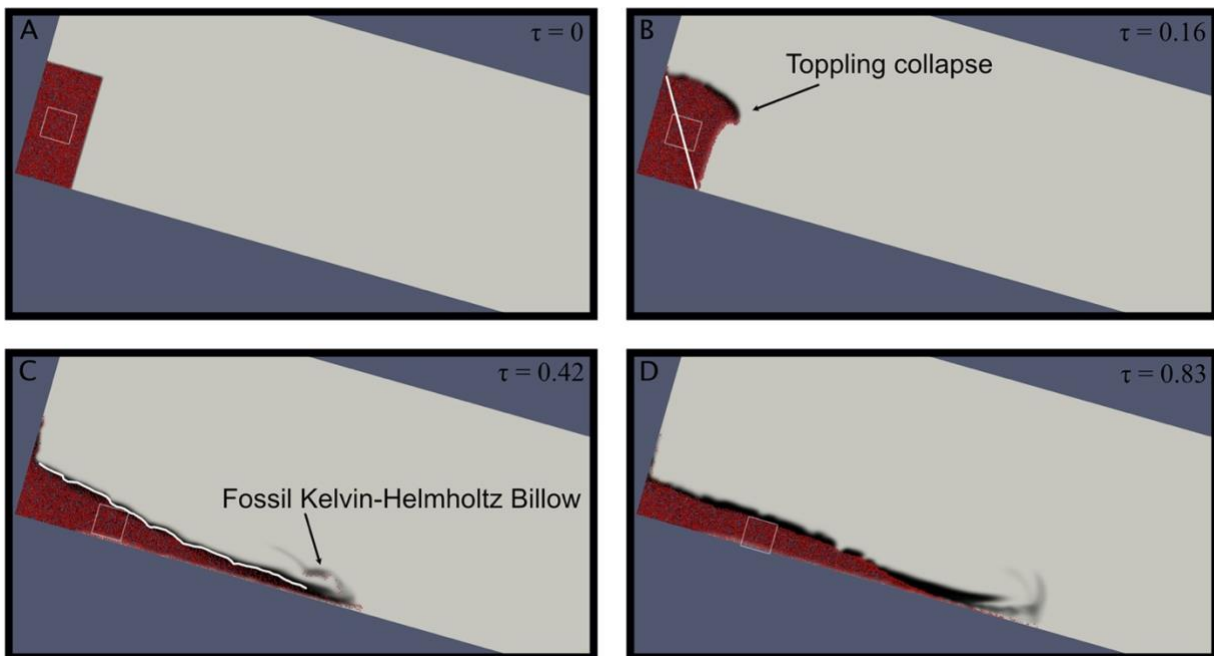


Figure 3.2. Four timesteps from the 0.1 friction coefficient dam break scenario. The domain is rotated 16 degrees. The black fluid has the same properties as the resident white fluid and is used as a tracer. The white box follows the center of mass. (A) is the initial condition of the system after 16 degree rotation. (B) The two collapse regimes, toppling collapse in the upper right corner of the column and sliding collapse (white line). (C) The fossil Kelvin-Helmholtz billow is the only remaining portion of the gravity current still in motion. Surface undulations of the heap flow are highlighted in white. (D) The particles have settled out of the Kelvin-Helmholtz billow and the heap flow continues to advance.

Hence the collapse produces three distinct dynamic regimes governed by hydrogranular behavior: 1) a toppling collapse where particles tend to separate and motion is dominated by a balance of viscous forces from the fluid and gravitational forces on the particles, which forms a dilute gravity current, 2) a mobile region of particles sliding on the granular shear zone that maintain contact and the transport is governed by both granular and viscous stresses, this forms a dense gravity current at high particle volume fraction, and 3) a quasistatic regime that rests at nearly the angle of repose, and does not participate further in the dynamics, other than acting as a base of support for the granular shear zone.

3.3.3 *Gravity current*

The gravity current develops as a result of the toppling collapse producing a dilute energetic flow that proceeds the main collapse. Velocity increases during the fall until the particles hit the sloping floor where they begin their down slope motion. The velocity contrast between the gravity current and the resident fluid creates a shear zone yielding a Kelvin-Helmholtz instability with a characteristic leading billow. The energy of the gravity current is rapidly exhausted and the energy in the Kelvin-Helmholtz billow is lost to viscous dissipation (fig. 3.2c). Column fluid and particles continue downslope with little circulation. Resident fluid becomes trapped under the gravity current when the flow reaches the floor. As the velocity decreases particles begin to settle and the current loses momentum eventually coming to a stop. Particles from the Kelvin-Helmholtz fossil arrive at the floor, eventually settling near the other particles in the gravity current (fig. 3.2d). The morphology of the gravity currents is not sensitive to the particle friction coefficient; both simulations are similar in shape, flow style, and both develop a Kelvin-Helmholtz billow from the velocity shear of the gravity current with the resident fluid. However, the duration of the collapse

between the two is different. The collapse time of the 0.58 friction coefficient simulation is longer than that of the 0.1 friction coefficient simulation, while the runout time is shorter for the 0.58 friction coefficient simulation. This leads to the total collapse and runout time being similar between the two simulations. It is interesting that the gravity currents in both simulations come to a stop at the same time because the 0.58 friction simulation collapse starts a few seconds later than the 0.1 friction simulation. This is because the particles in the gravity current from both runs are mostly fluidized and energy dissipation is dominated by viscous drag which is not influenced by granular stresses. Because the particles are fluidized there is little to no force chain development in the gravity current. Some of the particles form chains as they settle out of the gravity current, but these chains are generally below the average force found in the granular media.

3.3.4 *Plastic flow in the heap*

The kinematic regime that develops from the sliding collapse is dominated by particle-particle frictional interactions and deforms as a plastic flow. During the collapse, a heap of particles forms a triangular wedge that advances and thins (fig. 3.2c). The slope of the triangle steepens with an increasing friction coefficient of the particles. A higher velocity is found in the particles on the surface of the heap flow and surface undulations form as a result (fig. 3.2c). Particles that settled out of the gravity current are overridden by the advancing heap flow. The morphology of the heap flows is different between the two friction coefficient simulations. In the 0.1 friction simulation the granular heap thins at the back of the flow, forms a hump in the middle, and has a rounded advancing front. The 0.58 friction simulation maintains a somewhat triangular shape with a slight concavity in the middle, and a more gradual termination at the advancing front (fig. 3.2d).

The particles in the heap flow maintain enduring contacts throughout the flow, this results in the development of force chains. Figure 3.4 shows force chains at the center of mass for four

time steps. The four time steps are the initial condition, the collapse, the runout, and at the termination of the simulation. The force chains transition from a near isotropic, gravity parallel orientation to an anisotropic orientation that is near 45° from the direction of maximum shear stress.

3.3.5 *Quasi-static regime*

The quasi-static regime is in the lower left corner of the domain. In the quasi-static regime, the majority of the particles do not participate in the flow or collapse but maintain enduring contacts and a force chain support structure for the granular media. The particles undergo some adjustment and shifting during collapse and runout. In the 0.1 friction coefficient simulation the upper portion of the quasi-static regime does become involved in the flow. Since the quasi-static regime is not participating in the flow, the particles contacts and force chains maintain a mostly isotropic orientation.

3.4 MICROSTRUCTURE ANALYSIS

Each of the three regimes have distinct microstructures, described by the orientation of contacts and forces which yield the force chain fabric. In addition, we will look at the velocity and kinetic energy of the different kinematic regimes.

3.4.1 *Velocity and Kinetic energy*

The velocity and kinetic energy for 0.58 friction coefficient simulations are shown in figures 3.3 for the gravity current and the heap flow regimes. Ten particles were chosen to represent the kinematics of the gravity current and a 10 cm x10 cm box around the center of mass was used to represent the particles in the heap. The axes are scaled by equations 3.6, 3.9-3.11. Velocity is

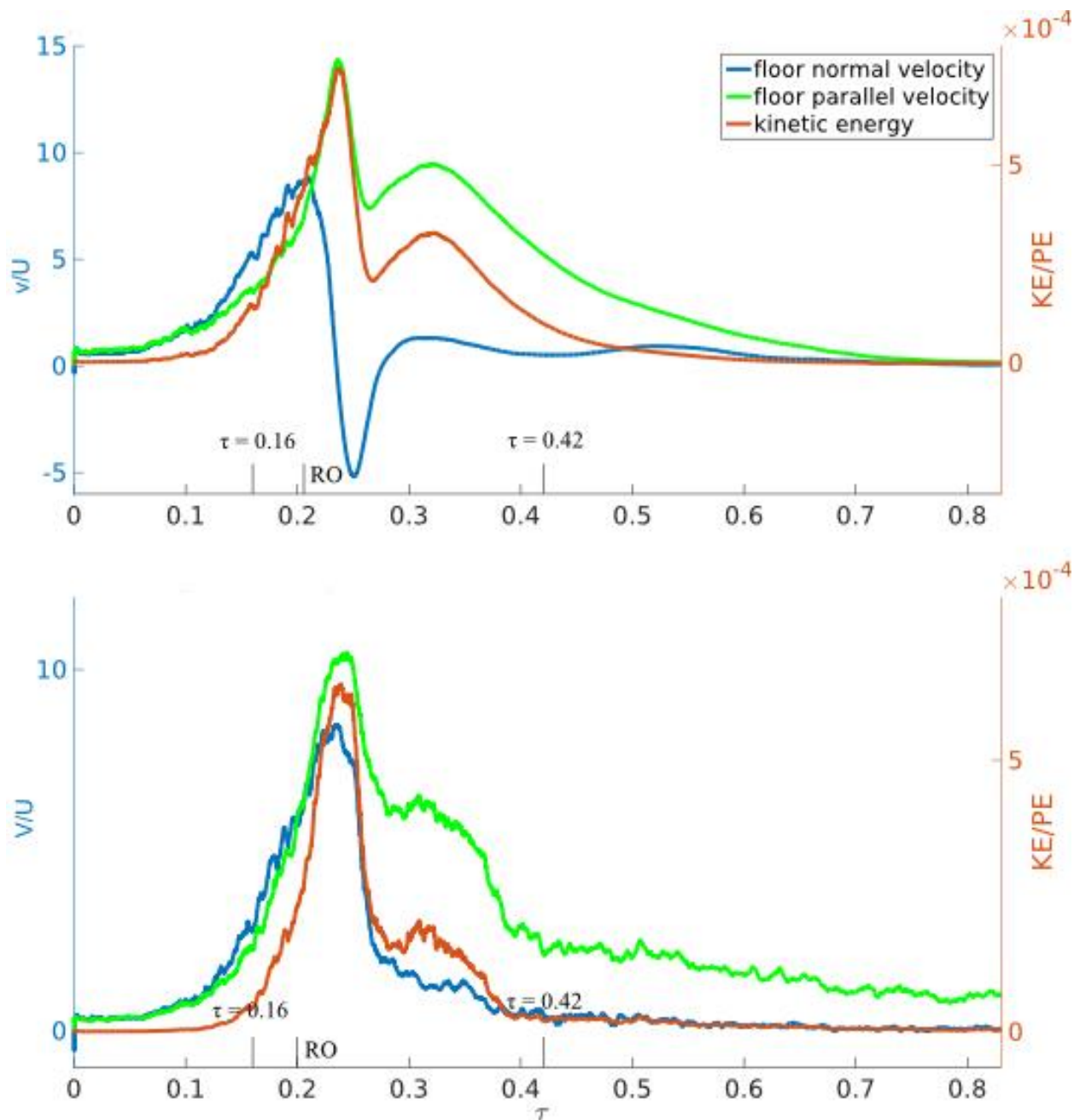


Figure 3.3. Velocity and kinetic energy for the particle friction coefficient of 0.58 simulation. Scaled time that are depicted in figure 3.2, $\tau=0.16$ and $\tau=0.42$ are highlighted, while $\tau=0$ and $\tau=0.83$ are the start and termination points on the axes. The line labeled RO indicates the time where the floor parallel velocity becomes dominant.

plotted in component form which shows the transition from collapse to runout. In both the 0.1 and 0.58 friction coefficient gravity current the floor normal velocity peaks at around 10 times the Stokes' settling velocity and the floor parallel velocity peaks at just under 20 times the Stokes'

settling velocity. In comparison, the center of mass has a floor normal velocity that peaks at around 7.5 times the Stokes' settling velocity and a floor parallel velocity that peaks at around 10 times the Stokes' settling velocity.

The timescale of the kinetic energy dissipation differs between the gravity current and heap flow regimes. In the gravity current case for a friction coefficient of 0.1, the kinetic energy reaches a maximum at the same time as the floor parallel velocity, where the floor normal velocity reaches a minimum. The kinetic energy and floor normal velocity approach zero at a scaled time of 0.4. Similar behavior is observed for a friction coefficient of 0.58, however, the timescales are shifted to greater values. This suggests that the mechanisms of dissipation are the same, and confirms the dissipation is largely due to viscous drag.

Kinetic energy in the heap flow regime is shown in Figure 3.3 at the center of mass. The important difference in dissipation between the gravity current and the heap flow regime is expressed in the high frequency overprinting in the heap flow for both friction coefficients. This is due to the intermittent gain and loss of granular contacts and the formation of fluctuating force chains. That the dissipation is more “noisy” for the 0.58 coefficient heap flow, is expected due to the greater energy loss by granular stresses.

3.4.2 *Force and contact anisotropy*

Hydrogranular systems are inherently isotropic as force chains locally branch and redirect around some average value. Non-coaxiality between contact and force normal arises through interactions involving grain scales properties. To quantify this anisotropy a description of the microstructure is required. The orientation of particles contacts, the distribution of forces among those contacts combined with the coordination number comprise the fabric, expressed as tensor state variables, equations 3.12-3.15.

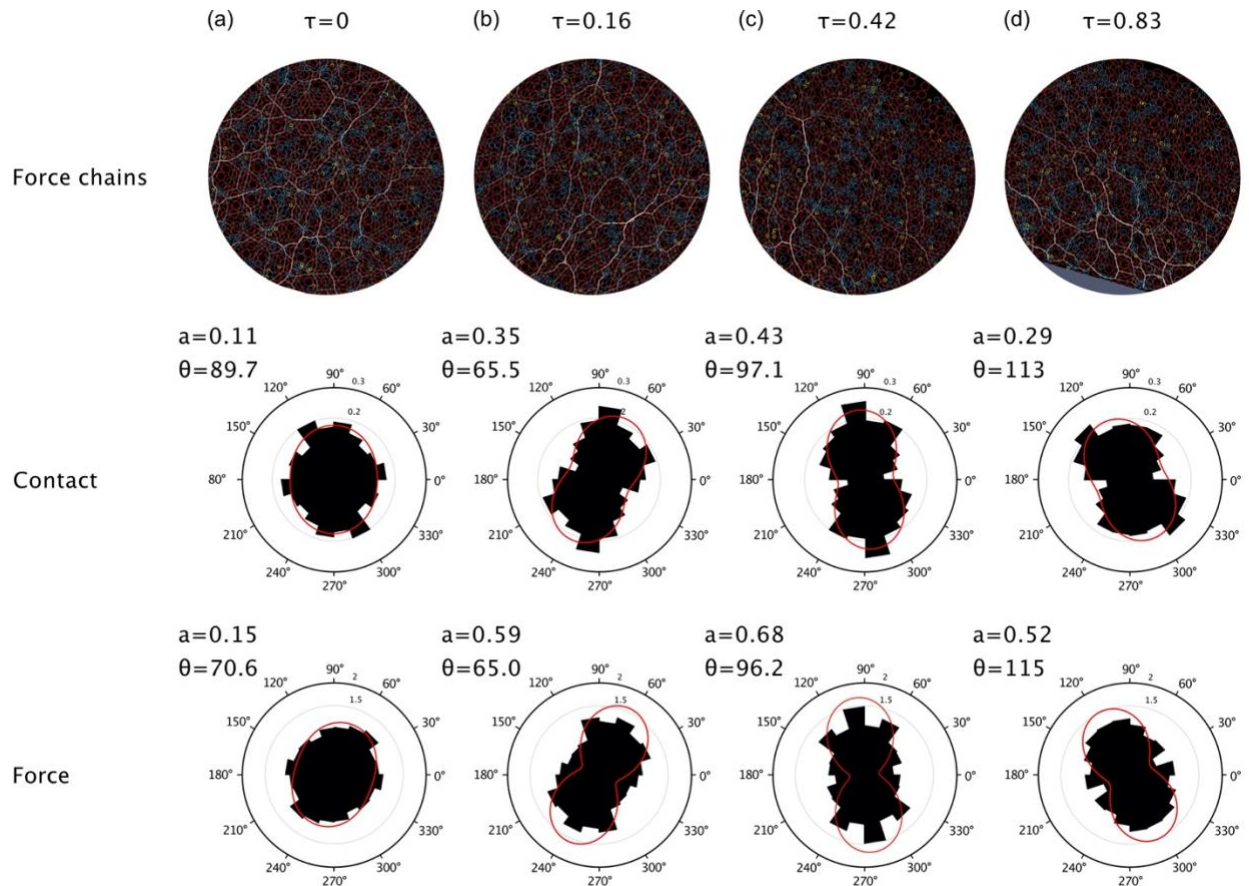


Figure 3.4. Force and contact anisotropy for particle friction coefficient 0.58. (a) The initial condition ($\tau=0$), (b) during the collapse ($\tau=0.16$), the transition from collapse to run-out ($\tau=0.42$), approaching the angle of repose ($\tau=0.83$).

The contact and normal forces for four timesteps at a friction coefficient of 0.58 are shown in figure 3.4. The initial condition ($\tau=0$) reflects the gravitational loading with a small degree of anisotropy. At $\tau=0.16$ the progress of collapse has reoriented the contact fabric through the loss of contacts due to down slope transport of the bed. The anisotropy in the force fabric reflects the dominant role of the remaining normal forces acting perpendicular to the bed. At the downslope motion of the heap no longer leads to a loss of contacts and the orientations of the granular stresses are consistent with those predicted from a simple frictional continuum. At $\tau=0.83$ the kinetic energy is nearly fully dissipated; the velocities are nearly zero and the anisotropy reflects the loading in a granular system approaching the angle of repose.

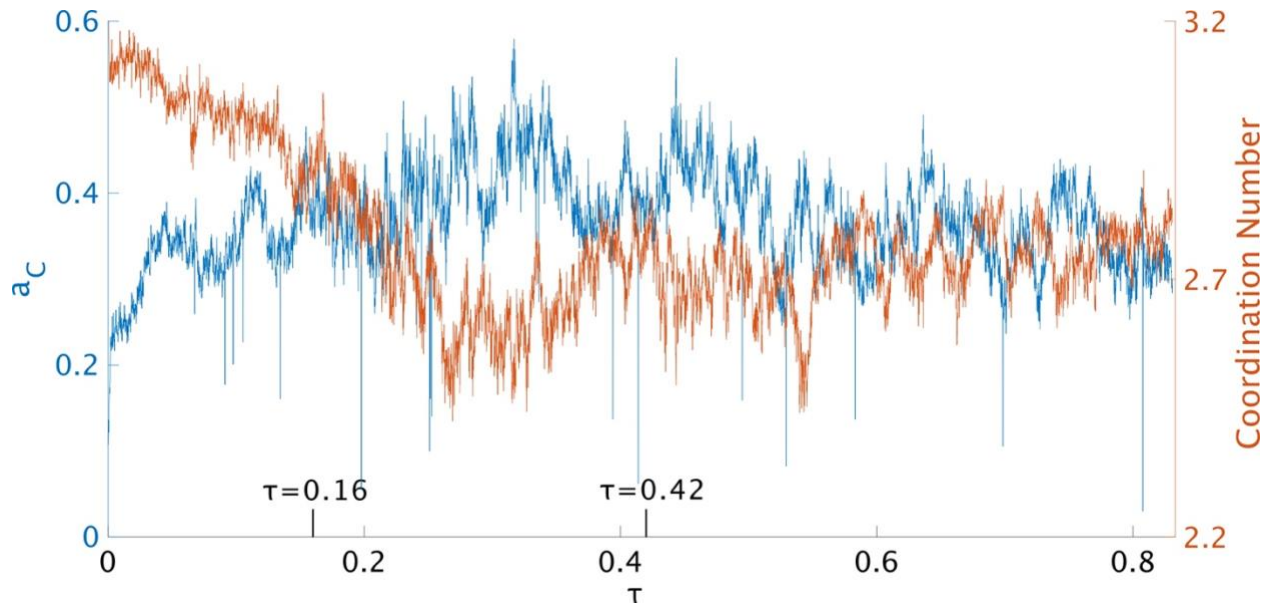


Figure 3.5. Contact anisotropy and coordination number for particle friction 0.58. The position of $\tau=0.16$ and $\tau=0.42$ on the x axis are indicated, while the positions for $\tau=0$ and $\tau=0.83$ are the start and termination points of the x axis.

The time dependence of the coordination number with the contact anisotropy are shown in figure 3.5. During the initial collapse there is a rapid decrease in the number of particle contacts and, hence, coordination number with a corresponding increase in the contact anisotropy reflecting the orientation of the remaining contacts. In triaxial tests, it has been shown that contacts are gained in the direction of greatest principle stress and lost in the direction of greatest extension (Rothenburg & Bathurst, 1989). Once the collapse is finished and the heap flow starts to translate down slope, the coordination number increases as the anisotropy decreases. During subsequent motion the coordination number fluctuates around a mean value, indicating the granular microstructure has reached a self-similar state.

The coaxiality of the force fabric and the contact orientations is presented in figure 3.6. After the initial transient associated with the collapse, the anisotropy difference fluctuates around a mean value of approximately 0.3. This illustrates how the contact and force microstructure are tightly coupled during the translation of the heap as the microstructure has reached a “noisy” steady

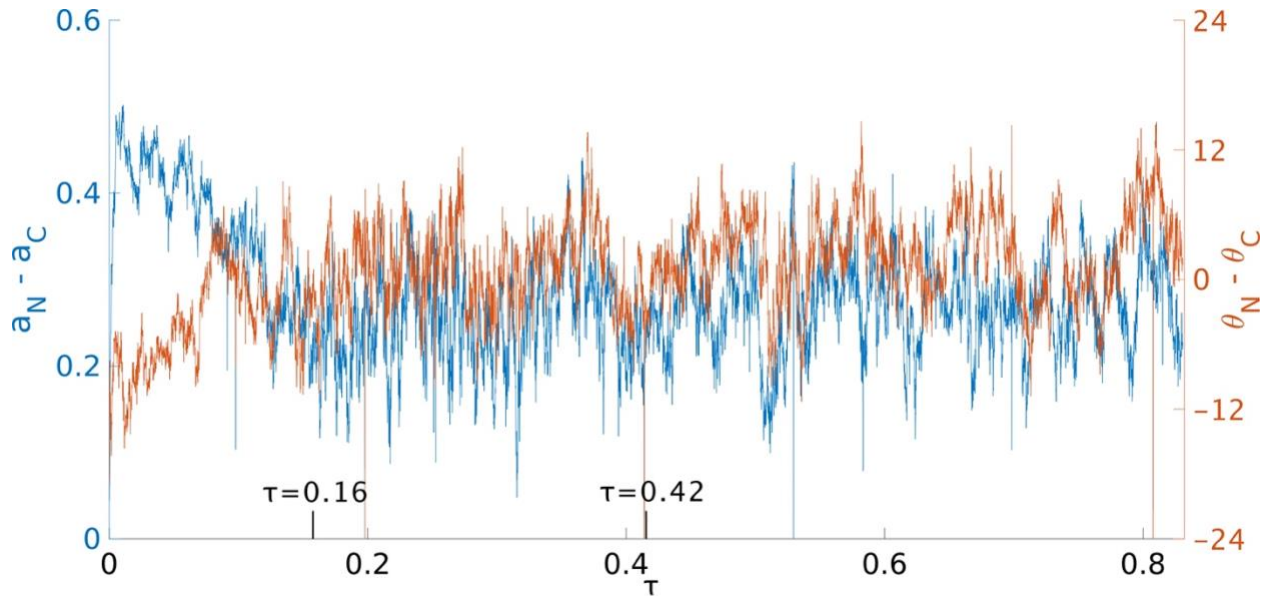


Figure 3.6. Contact and force fabric coaxiality for particle friction coefficient 0.58. The position of $\tau=0.16$ and $\tau=0.42$ on the x axis are indicated, while the positions for $\tau=0$ and $\tau=0.83$ are the start and termination points of the x axis.

state, and the difficulty of describing hydrogranular systems as a simple continuum. Given the stochastic nature of particle motion, perfect coaxiality might be approached but can never be achieved under natural conditions.

The results for the particle friction coefficient of 0.1 were qualitatively similar to those for the particle friction of 0.58, and so, will not be discussed further.

3.5 SUMMARY

A suite of numerical experiments was performed to investigate the kinematics and dynamics of a simple granular gravity current of relevance to magmatic processes as an aid in interpretation of natural examples. The multiphase system was modeled with a discrete element-computational fluid dynamics (DEM-CFD) approach which can resolve grain scale or granular stresses and strain. Two groups of simulations were conducted, one with a particle coefficient of friction of 0.1 and the other of 0.58. The initial condition was the collapse of a polydisperse particle column in a

viscous melt. Three distinct regimes were observed for both values of the friction coefficient: a gravity current, a translating particle heap, and a quasi-static regime.

Microstructural analysis of the force and contact anisotropy, and the coordination number, was used to quantify the role of granular stresses in particle-rich gravity current propagation. This highlights the role of granular friction and the fundamental difference between a particle-rich and pure fluid gravity current. Granular interactions are necessary to produce the three regimes, especially the granular shear zone which separates the heap flow from the quasi-static regime. These interactions are also important as an additional source of dissipation and leads to the final arrest of the flow and reduced runout. The anisotropy of the contact fabric can be attributed to the loss of particle contacts in the direction of initial extension. However, once the heap flow is translating down slope in a quasi-steady state, both the contact and force anisotropies differ by a nearly fixed amount. This reflects the nonaffine nature of particle transport and the challenge in applying traditional concepts from rheology and continuum mechanics to hydrogranular systems.

In addition, the role of negative pore pressure was revealed by the delay in the progressive nature of the toppling collapse. This negative pore pressure produces a pseudo-yield strength behavior that is a function of local particle volume fraction. This is an additional non-continuum process that cannot be recovered without consideration of grain-scale strain and transport trajectories.

While the initial condition is not intended to reflect natural conditions, these results illustrate the degree of particle dispersion by flow and the absence of mixing between interstitial melt and the resident melt. Thus, crystal-rich gravity currents are not a vehicle for mixing or the common observation of strongly zoned crystal populations. They may, however, be responsible for the common observation of layering in mafic intrusions. However, our simulations, which

model the crystals as spheres, are unable to address the role of shape preferred orientation and the emergence of shape fabric as a diagnostic indicator of flow.

Chapter 4. ON THE EXPULSION OF MELT FROM THE INTERSTITIAL SPACES OF A MAGMA MUSH BY PORE SPACE REDUCTION

4.1 INTRODUCTION

Arc systems create new crust largely by a process of repeated melt extraction from mantle-derived cumulates (Jagoutz & Klein, 2018; Müntener & Ulmer, 2018; Taira et al., 1998; Taylor, 1967). The typical arc section transitions from ultramafic/mafic rocks of the lower crust, through tonalites in the middle crust, and dacites/granites with erupted andesite/rhyolite in the upper crust/surface (Behn & Kelemen, 2006; Calvert, 2011; Calvert et al., 2008; Ducea et al., 2015; Rudnick, 1995; Rudnick & Gao, 2014). However, there is still debate on the mechanisms of melt migration and simultaneous pore space reduction (Holness, 2018; Holness et al., 2017; Vukmanovic et al., 2018). For example, processes such as viscous compaction (Cashman et al., 2017; McKenzie, 1984, 2011; Shirley, 1986; VanTongeren et al., 2015), have been shown to be less of a contribution to total pore space reduction in both mafic and felsic crustal systems (Holness, 2018; Holness et al., 2017; Vukmanovic et al., 2018). Our aim is to describe the outcrop and microstructural evidence that may preserve a record of the processes that initiate and sustain melt extraction, with a focus on the mafic lower crust of an arc where the compositional contrast between melts and the cumulates is most pronounced.

Exposed arc sections with clear evidence of transcrustal melt transport are uncommon. Exposures of the Famatinian arc in the Sierra Valle Fértil section provide a continuous record of the growth of the arc crust. The crustal section of Sierra Valle Fértil was created by block rotation to the east due to pre-Triassic uplift synchronous with terrain accretion during the Ordovician (Camilletti et al., 2020; Otamendi et al., 2020; Otamendi, Vujovich, et al., 2009). This rotation provides a cross

section through nearly the entire crustal column, from silicic upper crustal units to mafic/ultramafic lower crustal units. Thermobarometry conducted on metasediments indicate that the crustal column is structurally intact and the exposed units of Sierra Valle Fértil range in pressure from $<5 \pm 0.9$ kbar to approximately 8.2 ± 1.7 kbar or more (Tibaldi et al., 2013; Walker et al., 2015). The mafic complex is comprised of intermingled bodies of centimeter to meter thick layers of ultramafic pyroxene amphibole peridotite and troctolite; both millimeter to meter thick layers, and cumulate bodies of amphibole gabbronorite; and intermediate layers of millimeter to meter thick tonalite and granodiorite (Otamendi et al., 2010; Otamendi, Vujovich, et al., 2009). These compositional contrasts provide a unique opportunity for in-situ study of cumulate formation and melt extraction mechanisms. Preserved within the amphibole gabbronorite are different scales of millimeter to centimeter micro-tonalitic finger and stringers, and centimeter to meter irregular masses that provide outcrop scale physical evidence of melt migration processes and pathways. We utilize field observations and petrographic analysis of microstructural characteristics obtained from Electron Backscatter Diffraction (EBSD) to quantify the mechanisms of pore space reduction associated with tonalitic melt extraction from the amphibole gabbronorite cumulates. We collected twelve samples, eleven of which were oriented, ranging in composition from amphibole gabbronorites to tonalites. Sample collection was focused primarily within the central and upper parts of the mafic complex, proximal to the transition from mafic cumulate dominated to tonalite dominated plutons estimated to be at a pressure of between 6.7 ± 0.5 and 7.3 ± 1 kbar (Tibaldi et al., 2013; Walker et al., 2015) pressures and a maximum temperature of between 830 and 860 °C (Tibaldi et al., 2013).

4.2 MELT EXTRACTION FEATURES IN CRYSTALLIZING SYSTEMS

The diversity of melt collection and extraction features in migmatites has been documented (Brown, 2007, 2013; Brown & Solar, 1998; Hall & Kisters, 2016; Kriegsman, 2001; Martini et al., 2019; Sawyer, 1996, 1998, 2014; Weinberg & Mark, 2008; Závada et al., 2018). Despite fundamental differences in the initial conditions and rheology that lead to melt transfer in melting versus crystallizing systems (Burg & Vigneresse, 2002; Vigneresse & Tikoff, 1999), some features are shared. The expression of melt extraction features found in both migmatites and crystallizing systems are most apparent when there is a compositional contrast between the melt and residuum. These features include patches, veins, channels, stringers, sheets, dikes, and lenses of coarser grained regions that are crystallized remnants of melt that was extracted from a residuum. (Brown, 2007, 2013; Brown & Solar, 1998; Kriegsman, 2001; Sawyer, 1996, 1998) (figs. 4.2, 4.3b).

Evidence of melt extraction can vary with both the composition of the melt and cumulate, and the depth in the crust where extraction is active. Webber et al. (2015) analyzed melt extraction features of the Punta de Tracla tonalite of the Santo Domingo Complex in central Chile. They found that the melt extraction resulted from mafic and intermediate melt intrusion through dike networks. Intruding into the Punta de Tracla tonalite are mafic dikes preserved as enclave swarms. These mafic dikes show the replenishment, thermal rejuvenation, and remobilization of the crystal-rich magma chamber. The intrusion of the dikes, along with syn-magmatic deformation, caused dilation in the intermediate host resulting in the formation of faults, tension gashes, fold hinges, and strain shadows where the leucocratic matrix accumulated. Foliations that are defined by the preferred orientation of plagioclase, hornblende, and biotite within the melt accumulations around mafic enclaves are evidence of magmatic flow (Webber et al., 2015). Leucogranites intruding into the Abbabis Metamorphic Complex of central Namibia were analyzed by Hall and Kisters (2016).

They found fracture-controlled melt features including stromatic sheets and stringers that are connected by various sized lenses. The initiation of fractures provided pathways for magma movement, and as the fractures filled with magma, they grew to form lenses. The leucogranitic magma was then sufficiently buoyant to evacuate and ascend (Hall & Kisters, 2016). Finally, High silica granites of the Risco Bayo-Huemul Plutonic Complex in the Southern Andes of Chile are thought to be the solidified equivalent of extracted rhyolitic melt from a quartz monzonite mush (Schaen et al., 2018). Evidence for rhyolitic melt extraction from the quartz monzonite cumulates are found in the enrichment of trace elements in the quartz monzonite coupled with their depletion in the high silica granite, compositional gaps in whole rock analyses between granite and the high silica granite, Sr ratios, and abundant miarolitic cavities in the high silica granite (Schaen et al., 2018).

While there are similarities in the expressions of melt extraction between the crystallizing and melting systems, they display distinct changes in rheology due to increasing or decreasing melt fractions. In a melting system, an increase in the volume of melt leads to a decrease in the system viscosity. This rheological transition occurs when the volume of melt, initially present only on grain boundaries, increases to become an interconnected network of melt pockets, and eventually, channels of melt flow. In crystallizing systems, the growth of a crystalline network causes magma convection to transition into channelized flow and ultimately rheological lockup of the magma (Burg & Vigneresse, 2002; Sawyer, 1996, 1998; Vigneresse et al., 1996).

Porous melt flow through a crystalline network initiates at a different solid volume fraction in the crystallizing system than in the melting system. The point at which melting systems form an interconnected network of melt pockets is called the liquid percolation threshold (LPT) and the point at which crystallizing systems form a network of touching particles is termed the rigid

percolation threshold (RPT) (Burg & Vigneresse, 2002; Vigneresse et al., 1996). The amount of melt necessary to reach the LPT is less than that needed to reach the RPT. Field observations of partially molten gneisses show that the LPT can be as little as 8 volume percent melt and estimates of random loose packing place the RPT at 55 volume percent crystals (Burg & Vigneresse, 2002; Vigneresse et al., 1996). When the melt volume of the melting system reaches approximately 20 to 25 volume percent, the melt becomes connected through a pore network and the cohesive strength of the protolith vanishes. The loss of cohesive strength in the protolith marks the transition from the LPT to the melt extraction threshold (MET) (Burg & Vigneresse, 2002; Vigneresse et al., 1996). While with the crystallizing system, the continued nucleation and growth of crystals clogs the system to the point where magma can no longer escape without crystal plastic deformation. Crystals become jammed when a random close packing is reached, which is at approximately 70-75 solid volume percent, and is termed the particle locking threshold (PLT) (Burg & Vigneresse, 2002; Vigneresse et al., 1996).

The differences in the amount of melt or crystals needed before melt pathways form, indicate that the mechanisms of extraction could differ between the two regimes. In fact, Etheridge et al. (2021) showed that the increase in volume when melting of a closed system is sufficient to initiate melt extraction. Given that in a crystallizing regime volume should decrease, we would not expect volume change to contribute significantly to the melt extraction process. Yet, the presence of adcumulates (rocks where nearly all the residual melt was expelled) suggest that melt extraction is active in crystallizing systems at high solid volume fractions (Wager et al., 1960) similar to migmatites. The diversity in rheological conditions and expressions of melt extraction in crystallizing systems implies that different mechanisms may be active at different crystallinities and more than one mechanism may be active at the same time. These differences shed light on the

need to consider the process of melt extraction from crystallizing systems as distinct from melting systems.

4.3 MECHANISMS OF MELT EXTRACTION FROM CUMULATES

Here, we will briefly review melt extraction processes with a focus on the microstructural indicators expected for each mechanism. These microstructural indicators are a result of both plastic deformation such as dislocation creep and dissolution–reprecipitation, and both a shape and crystallographic preferred orientation (SPO and CPO respectively).

4.3.1 *Shearing of non-spherical particles*

There is a limit to how much pore space can be reduced by deforming crystal mushes (Holness, 2018; Holness et al., 2017; Marsh, 1981). A critical volume fraction defined by a plateau volume fraction where both compacting loosely packed and dilating densely packed materials converge when sheared (Andreotti et al., 2013, pp. 123-125). Introducing a shape preferred orientation to the crystals composing the mush provides a way to increase the density of the crystal packing. A preferred orientation develops when shearing densely packed disk- and rod-shaped particles with aspect ratios of 0.1 and 4, respectively, and a solid volume fraction of 0.5 for both (Y. Guo et al., 2013; Y. Guo et al., 2012). However, shearing of both spherical and non-spherical particles under constant pressure conditions increases the void ratio (Zhao et al., 2018). The void ratio is the volume of voids over the volume of solids. Increasing the void ratio increases the diameter of the interstitial spaces, and this dilation transports melt into the mush. Therefore, a shear induced preferred orientation still has a net dilation and may not be the pore reducing mechanism.

4.3.2 *Accumulation and primary fabric formation*

Crystal fabric that forms in the suspension regime, above the rigid percolation threshold of a magma, where the crystals are free to re-orient, will be referred to as primary fabric. In this suspension regime, crystals behave as rigid -non-deforming- solids, although some plastic deformation of crystals is possible in dense suspensions, where deformation of the mush is accommodated by the melt in the instances of magmatic flow. Non-equant grains can form a shape preferred orientation (SPO) from settling in a static or convecting magma. This SPO can be expressed as either foliations or lineations (Holness et al., 2017; Nicolas, 1992), and depends on the number of grains in the suspension (this determines how often the particles interact), the aspect ratio of the grains, and the amount of shear -a flowing magma- (Holness et al., 2017; Yamamoto & Matsuoka, 1996). Magma flow applies stresses in the form of simple shear on the suspended crystals. This shear causes non-equant, rigid, and isolated grains to align with the direction of magma flow (Holness et al., 2017; Nicolas, 1992; Yamamoto & Matsuoka, 1996). Crystals rearranged by magmatic flow can form a fabric in the form of an SPO or a crystallographic preferred orientation (CPO) (Holness et al., 2017). When the amount of crystals suspended in the melt have a quantity such that they are interacting with each other, the crystals can form an imbrication or tiling texture when exposed to magmatic flow (Nicolas, 1992). Non-equant crystals can also be rearranged at the interface of the mush and magma forming an SPO (Holness et al., 2017).

4.3.2.1 *Overprinting of melt extraction fabric*

Either hypersolidus or subsolidus deformation of cumulates can overprint and obscure both an SPO and CPO that developed as a result of primary magmatic or secondary melt extraction processes. Textural equilibration of grains due to the reduction of interfacial energy in either a

subsolidus or hypersolidus state, where the temperature of the system has remained elevated for a prolonged period, can result in the obliteration of SPO, but may preserve the CPO, formed during melt extraction. Stress can continue to deform the crystals after solidification of the magma by dislocation creep, sub-grain formation, and grain boundary migration. This can overprint both the SPO and CPO with one that is a result of that stress (Holness et al., 2018; Holness et al., 2017).

4.3.3 *Filter pressing*

Filter pressing is the forcing of melt from interstitial spaces between crystals into adjacent regions of a magmatic system through either regional stress acting on the magmatic system (tectonic), or pressure differences driven by exsolving volatiles (gas).

4.3.3.1 Tectonic filter pressing

Tectonic forces acting on a magmatic system can extract melt from interstitial spaces of cumulates (Brown, 1994; Sawyer, 1994). In calc-alkaline systems, where there is a compositional contrast between the mafic cumulates and the tonalitic interstitial melt, extraction features can be observed at the outcrop scale as vein networks and bands of felsic melt (Berger et al., 2017). The most common microstructure that can be readily interpreted to be a consequence of tectonic filter pressing is a preserved Shape Preferred Orientation (SPO) (Berger et al., 2017; Garibaldi et al., 2018). Orientations of the prismatic crystals are generally perpendicular to the direction of shortening and subparallel to the direction of magma flow (Benn & Allard, 1989; Berger et al., 2017; Garibaldi et al., 2018; Nicolas, 1992). As a result of filter pressing, both brittle and ductile microstructures can be observed (Berger et al., 2017), as well as rigidly rotated grains in regions of magmatic flow (Benn & Allard, 1989; Nicolas, 1992). Evidence for brittle deformation is often expressed through the presence of fractures filled with felsic melt (Berger et al., 2017; Bouchez et al., 1992), whereas crystal plasticity is recorded by the presence of bent plagioclase grains and

sporadic low angle boundaries (Berger et al., 2017). Crystals rigidly rotating in magmatic flow will reorient their long axis to the flow direction depending on their aspect ratio and the number of grains suspended in the magma. Crystals with higher aspect ratios reorient slower than crystals with lower aspect ratios and will have an orientation sub parallel to the flow. If crystals have higher aspect ratios or there is a higher density of crystals suspended in the flow, the likelihood that the crystals will interact with each other increases. Interacting crystals suspended in a magmatic flow can become imbricated, forming a tiling texture. Tiling creates both an SPO and crystallographic preferred orientation (CPO) (Benn & Allard, 1989; Nicolas, 1992).

Berger et al. (2017) looked at the West African Igulid Mafic Intrusion to identify melt extraction processes. They showed that tectonic shortening with simultaneous crystallization from the margins led to a magma flow induced shape preferred orientation (SPO) of the elongate crystals during melt extraction and pore space reduction. In contrast Petford et al. (2020) explored the shearing of a crystal-rich mush where the crystal fraction is above 70% via numerical modelling. They found that shearing these crystal-rich systems results in the dilation of the mush, which increases the pore space. This dilation of the pore space reduces the pore fluid pressure causing more melt to flow in, possibly leading to brittle failure of the mush and melt flowing out along granular faults (Petford et al., 2020). Petford et al. (2020) found that tectonic strain caused dilation on timescales of 10^2 to 10^4 years which is greater than the timescales of thermal diffusion at thermal diffusivities of 3.5×10^{-7} to 5×10^{-7} . This indicates that the magma is likely to completely crystallize before significant segregation of the melt and solid fractions is achieved (Petford et al., 2020). This suggests that tectonic filter pressing is not ubiquitous but unique to certain systems, therefore, other process must be at work in extracting melt from cumulates.

4.3.3.2 Gas driven filter pressing

Gas driven filter pressing occurs when both the crystallizing magma expands and melt is segregated from the crystals due to the over-pressurization of the magma by exsolving volatiles (Anderson et al., 1984; Sanders, 1986; Sisson & Bacon, 1999). Anderson et al. (1984) identified vesicles in subaerial flows of basalt and basaltic andesite that had been filled with melt after the vesicles had become rigid. They speculated that the melt was pushed through a rigid but permeable network of crystals and into the rigid vesicles in response to a pressure gradient generated by the concentration of H₂O in the remaining melt after continued crystallization (Anderson et al., 1984). Later, Sanders (1986) identified segregation vesicles in two dolerite dikes in northwestern Ireland. He determined that the filled vesicles formed from the exsolution of CO₂ and were subsequently filled after H₂O was sufficiently concentrated during crystallization and exsolved in the melt. This second boiling created a pressure gradient that forced melt through the crystalline network and into the CO₂ vesicles. The CO₂ formed vesicles are spherical in shape, while the vesicles formed by the exsolution of H₂O are misshapen due to forming within the crystalline network (Sanders, 1986).

The understanding of gas driven filter pressing has expanded from the initial ideas of Anderson et al. (1984) and Sanders (1986) to include the ejection of melt from the crystal-mush. This extraction mechanism is thought to contribute to melt segregation in shallow magma reservoirs of depths less than 10 km (Lowenstern, 1994; Pistone et al., 2015; Sisson & Bacon, 1999). However, melts with greater than 0.6 wt% H₂O could become saturated with CO₂ at depth between 20 and 50 km. And, it is possible for a magma degassing CO₂ to also degas H₂O (Wallace, 2005). The possibility of degassing CO₂ and H₂O at depths greater than 10 km suggests that gas driven filter pressing could be active in lower and mid crustal magmatic system. The next paragraph evaluates the likelihood of gas driven filter pressing occurring at our sample location.

To determine if gas driven filter pressing was active in Sierra Valle Fértil, we need to understand how CO₂ and H₂O behave in magmatic systems and how much of each was available. Exsolution of water vapor and carbon dioxide is determined by the concentrations of each gas in the magma, the composition of the magma, the oxygen fugacity, the temperature, and the pressure of the system (Lowenstern, 2001; Roggensack et al., 1997; Wallace, 2005). Sierra Valle Fértil Mass balance calculations show that the original water concentration of the magma was between 1 and 2wt.% and increased to between 3 and 5wt.% at around 50% crystallization, indicated by the appearance of amphibole (Otamendi et al., 2010). An H₂O concentration of 3-5wt.% would not exsolve water vapor at the crystallization depth of our samples regardless of the CO₂ concentrations (Lowenstern, 2001; Moore, 2008; Roggensack et al., 1997; Wallace, 2005). Constraining the saturation pressure and exsolution of CO₂ is more complicated. The primary uncertainty is the original CO₂ content of the mafic magmas at the time of intrusion. Variations in CO₂ concentration in magmas can lead to CO₂ saturation at depths from anywhere between 20 to 50 km (Wallace, 2005). Evidence from eruptions of volcanoes, such as Cerro Negro, suggest that for volatile-rich arc magmas, the saturation pressure is approximately 6 kbar (Lowenstern, 2001; Roggensack et al., 1997). However, the magma intruding at Valle Fértil was not volatile-rich and our samples formed at approximately 7 kbar; therefore, we assume that gas driven filter pressing was not contributing to the extraction of melt from the interstitial spaces of the mafic cumulates of Valle Fértil.

4.3.4 *Compaction*

4.3.4.1 Mechanical compaction

Mechanical compaction is defined by Holness (2018) as the rearrangement of ridged, non-deforming, grains. Mechanisms that can accommodate mechanical compaction are shape sorting

by magmatic currents, slumping of a magma mush, (Holness, 2018), and magma recharge (Carrara et al., 2020).

The Skaergaard layered mafic intrusion provides an example of mechanical compaction via magmatic currents (Holness et al., 2017; Vukmanovic et al., 2018). When investigating the Skaergaard adcumulates, Holness et al. (2017) found a preserved SPO and CPO. Despite having a preserved fabric, they found that there was almost no deformation of the crystals in the form of dislocation creep nor dissolution-reprecipitation. They conclude that the observed CPO and SPO in the adcumulates is a result of either primary mush formation processes or secondary processes acting at the interface between the mush and bulk magma, such as a magma current (Holness et al., 2017). Similarly, Vukmanovic et al. (2018) found SPO and CPO with minimal evidence of plastic deformation in plagioclase grains from the trough bands of Skaergaard. They conclude that the fabric is consistent with an origin from crystal-laden density currents that originated from the chamber walls (Vukmanovic et al., 2018).

The kinematics of magma recharge have been investigated by numerical models (Bergantz et al., 2015, 2017; Carrara et al., 2020; Schleicher & Bergantz, 2017; Schleicher et al., 2016). Schleicher and Bergantz (2017) found that the injection of magma into a preexisting magma mush causes the mush to have a viscoplastic response which fluidizes the crystals directly above the injection and forms a mixing bowl. The boundaries of the mixing bowl are granular faults. Crystals from the base of the mush are entrained in the rising magma plume while crystals from the top of the mush are transported down towards the intruding material along the granular faults (Schleicher & Bergantz, 2017). (Carrara et al., 2020) expanded on the model by intruding melts that have a density contrast with the host melt. They found that when the density of the intruder was greater than the density of the host melt the intruder remained close to and spread out along

the bottom of the mush, an intruder whose melt is less dense than the host melt formed a rising regime where the intruding melt punches through the crystal mush, and a fluidization regime when the densities of the intruding melt and host melt are equal (Carrara et al., 2020). In all three modeled cases, (Carrara et al., 2020) found that the intrusion forced the residual melt out of the space being intruded and into the rest of the mush. This intrusion over pressurized the pore spaces in the mush forcing the crystals apart and decreasing the crystal volume fraction (Carrara et al., 2020). While the use of spherical particles in these experiments prevented the analysis of a shape fabric, both a force and a contact preferred orientation developed with the continued input of the intruding magma (Bergantz et al., 2017). It is likely that the development of a mixing bowl from magma recharge would generate preferred orientation of the non-equant crystals being conveyed towards the intrusion along the granular faults.

4.3.4.2 Viscous compaction

Viscous compaction is the reduction of pore space in a crystal mush by the plastic deformation of crystals within the mush due to the gravitation loading of crystals settling out of the magma. Viscous compaction occurs at the point when the reduction of pore space by the rigid rearrangement of crystals can no longer occur. Mechanical compaction can act on a clustered crystal framework until the point of jamming (Jerram, 2003; Philpotts et al., 1998). The further compaction of the crystal mush can be achieved by the viscous deformation of the crystal (Bertolett et al., 2019; Holness et al., 2017; VanTongeren et al., 2015).

Mckenzie (1984) introduced a numerical model that considers the viscous compaction of a crystal-rich magma mush for both the mantle and crust. The concept of the model is that the density contrast between crystals and melt causes the crystals to settle out of the magma. As the crystals accumulate, the crystals deeper in the accumulated mush have greater and greater stresses

applied. This stress, under magmatic conditions, eventually causes the crystals to plastically deform by processes such as dislocation creep and dissolution-reprecipitation. The actively deforming layer of mush is characterized by an inverse relationship between the fraction of interstitial melt and depth. This layer is bound on the bottom by a migrating upwards crust and bound at the top by the bulk magma. The reduction of pore spaces expels the remaining melt while the pore spaces are interconnected. Therefore, viscous compaction works from the bottom up forcing melt from lower in the mush upwards and out into the bulk magma (Mckenzie, 1984, 2011).

The presence of viscous deformation can affect the CPO depending on which deformation mechanism is operating. If the principal mechanism is dislocation creep, the primocrysts will record low angle boundaries and crystal bending. In this case, the CPO might be very similar to the magmatic fabric (Benn & Allard, 1989; Nicolas, 1992; Stunitz, 1998). The mechanism of dissolution–reprecipitation changes the shape of the crystals, producing crystals with no faceted faces and can alter the CPO. On the example of plagioclase, dissolution–reprecipitation will create a CPO fabric with [100] axes perpendicular to the compression direction whereas the (010) faces and poles to (001) are parallel to the compression direction (Arvidson et al., 2004; Heidelbach et al., 2000). Grains will be elongated in a direction perpendicular to the (010) faces (Svahnberg & Piazzolo, 2012), instead of parallel to (010).

4.3.5 *Summary*

Expelling melt from the interstitial spaces of cumulates by either tectonic filter pressing, gas driven filter pressing, viscous compaction, or mechanical compaction will impart a microstructural signature to the cumulate. While individual microstructures may be the same for multiple extraction mechanisms, the combination of microstructures for each mechanism are unique.

Techniques such as Electron Backscatter Diffraction (EBSD) identify lattice distortions and CPO in the analyzed samples. The data obtained from the analyses can then be used to identify which of the melt extraction mechanisms were active.

4.4 GEOLOGIC SETTING: THE FAMATINIAN MAGMATIC ARC

The Famatinian arc (Fig. 2.1) is a subduction-driven paleo arc that formed on the proto-Pacific margin of Gondwana and was active from the upper Cambrian to the middle Ordovician (Otamendi, Vujovich, et al., 2009). Accretion of an exotic, Laurentian-derived (Otamendi, Vujovich, et al., 2009) terrane resulted in the cessation of magmatism in the central section of the paleoarc (Otamendi et al., 2010; Otamendi, Vujovich, et al., 2009). Paleozoic and Andean uplift caused the differential exposure across approximately 2500 km of the arc, from northern Peru to central Argentina (Cristofolini et al., 2014; Tibaldi et al., 2013). In Argentina, the Famatinian arc is exposed between 22°S to 38°S (Tibaldi et al., 2013). A deep crustal section is exposed in the region of Sierra Valle Fértil from 28°S to 33°S (Cristofolini et al., 2014; Otamendi, Ducea, et al., 2009; Tibaldi et al., 2013). Overall, the strike of the Famatinian arc is approximately N-S (Cristofolini et al., 2014; Otamendi, Ducea, et al., 2009; Tibaldi et al., 2013). The Sierra Valle Fértil exposes an eastward-tilted section of arc crust that provides a cross section from paleodepths of 12-32 km (Tibaldi et al., 2013; Walker et al., 2015).

The exposed section of Sierra Valle Fértil is almost completely plutonic and preserves no stratigraphic relationships of the migmatites and other metasedimentary rocks that are dispersed throughout the system. Directionality is determined by using magmatic indicators, groupings of rock types, and thermobarometry. The rock units that comprise Sierra Valle Fértil are a mafic unit that is dominated by amphibole gabbro-norite, quartz bearing diorites, and olivine bearing cumulate

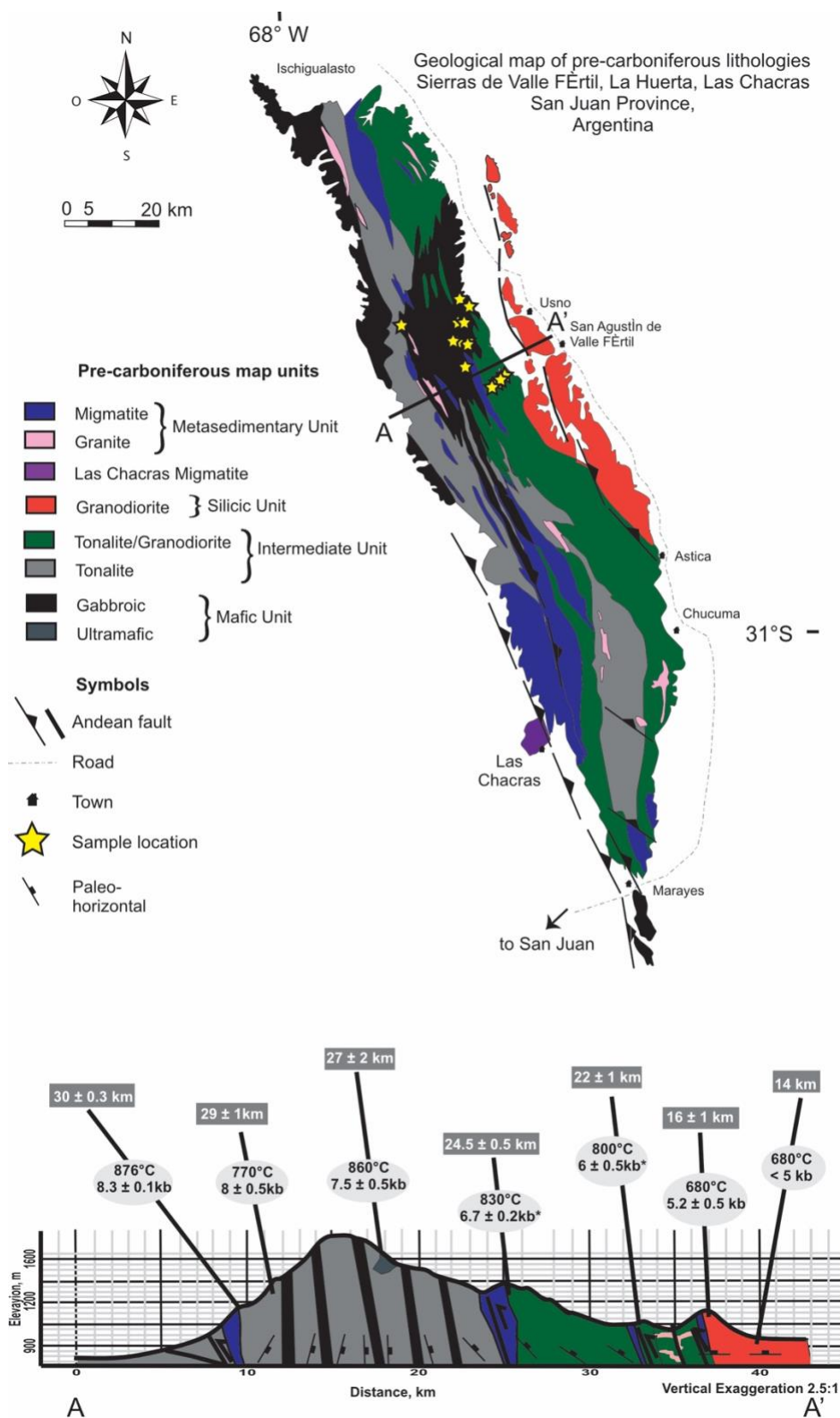


Figure 4.1. Geologic map of the Sierra Valle Fértil modified from Otamendi, Vujovich, et al. (2009); Tibaldi et al. (2013); Walker et al. (2015) and geologic cross section with temperatures and pressures modified from Tibaldi et al. (2013); Walker et al. (2015).

rocks; an intermediate unit of tonalite that is amphibole rich and biotite bearing; an amphibole and biotite bearing granodiorite; and metasedimentary units that are dominated by paragneissic migmatites (Otamendi et al., 2010). A primary magmatic foliation defined by a shape preferred orientation of plagioclase laths and elongate amphibole is pervasive throughout the gabbroic rocks (Cristofolini et al., 2014). Chemical abrasion-thermal ionization mass spectrometry (CA-TIMS) ages suggest that the total lifespan of the system was around 4 million years falling between 472 to 468 Ma (Ducea et al., 2017).

Intrusion of mafic magmas due to subduction related magmatism in the region of Sierra Valle Fértil caused deformation and partial melting of the surrounding country rock (Otamendi, Vujovich, et al., 2009). With the cessation of magmatism from the accretion of the allochthonous terrane, came uplift of the plutonic bodies of Sierra Valle Fértil (Otamendi et al., 2020; Otamendi, Vujovich, et al., 2009). Evidence for this uplift and strain are preserved as discrete mylonitic belts in both the igneous and metasedimentary bodies. The solid-state foliation fabrics in the igneous mylonites, generated by the strain from uplift, parallel and transition from the magmatic layering and are roughly trending N-S. The mylonitic microstructures found in the igneous suite have two distinct fabrics. The first is a coarse-grained texture with rounded clasts of amphibole, plagioclase, clinopyroxene, orthopyroxene, and quartz. The second microstructural fabric is a dynamically recrystallized fine-grain matrix with serrate grain boundaries (Cristofolini et al., 2014).

4.4.1.1 Expressions of melt extraction

Melt extraction features are preserved in the mafic complex gabbroic cumulates that range in size from millimeter to centimeter patches and veins to meter scale channels and dikes. In some cases, in situ melt was able to separate from the crystals and pond but no veins or channels formed to accommodate melt movement (Fig. 4.2a). Other locations show melt moving in channels and

veins to local dilatational areas where the melt ponds (Fig. 4.2b). Multiple scales of melt segregation are also preserved in the same outcrop (Fig. 4.2c). In these outcrops we see separate



Figure 4.2. Expressions of tonalitic melt extracted from amphibole gabbronorite preserved in the mafic complex of Valle Fertil. (a) Patches of in situ nonfoliated tonalitic melt separated from the mafic cumulate. (b) channels and veins of tonalitic melt in a gabbro cumulate host. (c) a variety of expressions where tonalitic melt is segregating from the gabbroic cumulate. See text for details. (d) Tonalite surrounding blocks of cumulate.

patches of melt not connected to any veins or channels indicating that melt is segregating from the cumulate, while adjacent to the patches are veins and channels where melt was likely sourced from outside the local area and flowed into centimeter to meter sized ponds. Figure 4.2c illustrates how local rheology can vary on the centimeter scale, where coherent blocks of cumulate, from which the melt has already been extracted, is just centimeters away from cumulate undergoing extraction. Figure 4.2d shows blocks of brecciated cumulate being surrounded by tonalitic melt.

4.5 METHODS

4.5.1 *Electron Backscatter Diffraction (EBSD)*

Fourteen thin sections from eleven oriented samples, and thin sections from four unoriented samples were polished for approximately one hour using 0.06 micrometer colloidal silica at the University of Cambridge, UK. These 18 thin sections were then analyzed on an FEI sFEG XL30 SEM located in the Department of Physics at the University of Cambridge. The electron backscatter diffraction patterns (EBSDPs) were collected using AZtecHKL 2.2 acquisition software. Both MTEX MatLab toolbox and Oxford Instrument Channel 5 software were used for constructing pole figures and EBSD maps (Hielscher & Schaeber, 2008). The EBSD working conditions were 20.0 kV, a 70° specimen tilt, the aperture set to 3, a working distance of 20 mm, and a step size of 20 μm . A 4 x 4 binning was used for camera settings and a frame averaging of 3 was used for image processing. Each scan conducted covered approximately 1/3 of the thin section and took around 3 hours to complete. The long scan time prevented us from scanning the entire thin section.

Channel 5 software was employed to create the one point per grain dataset that was used to plot pole figures in MTEX MatLab. The construction of pole figures was based on a lower hemisphere, equal area projection. Determination of the fabric strength was conducted by calculating the M-index, J-index, pole figure J-indicies, (PFJ), and the BA-index using the MTEX MatLab toolbox Orientation Distribution Function (ODF). To identify the location of the subgrains and determine the amount of misorientation, both total misorientation in a single grain and at individual dislocations, misorientation to mean orientation (Mis2Mean) and kernel average misorientation (KAM) were performed on the full EBSD data (Wright et al., 2011). KAM calculations use a pixel and its neighbors (kernel) to calculate the misorientation. The average

difference in orientation of the neighboring pixels with that of the center pixel is the misorientation assigned to the center pixel (Cruz-Gandarilla et al., 2019). Shape preferred orientation rose diagrams were created using the MatLab fit ellipse function after the removal of all grains from the calculation that intersected the scanned area boundary. The orientation of the long axis of the ellipse was then plotted in the rose diagram.

4.5.2 *Quantitative evaluation of minerals by scanning electron microscopy (QEMScan)*

QEMScan images for the 15 thin sections from the 11 oriented and 1 unoriented sample were collected at the Department of Earth Sciences, University of Cambridge using a Quanta 650F field emissions gun that is equipped with two Bruker XFlash 6130 energy dispersive spectrometers (EDS). Maps of the concentrations of Ca in Plagioclase crystals were created to visualize the compositional zoning in plagioclase and to aid in identifying dissolution-reprecipitation and/or diffusion creep as per Holness et al. (2017). The QEMScan image resolution is 5 μm .

4.6 PETROLOGY

Samples FA18-01 through FA18-12 were collected throughout the Usno, El Jaboncillo, El Turbante, and Corral Grande valleys of Valle Fértil. We supplemented this data set with samples FA10-03m collected in the upper reaches of Usno Valley, FA10-17 collected in Las Tunas Valley, and FA2-11-26 collected in Algarrobo Valley. We collected samples in the mafic complex of Valle Fértil which ranges in pressure from 6.7 to 8.3 kb (Tibaldi et al., 2013). The reported grain sizes are determined using the long axis of the grains calculated using the fitEllipse function in MTEX v5.2.0 on MatLab R2019a, and the aspect ratio is calculated using the aspectRatio function in MTEX v5.2.0 on MatLab R2019a. Both functions are used after the removal of twin boundaries

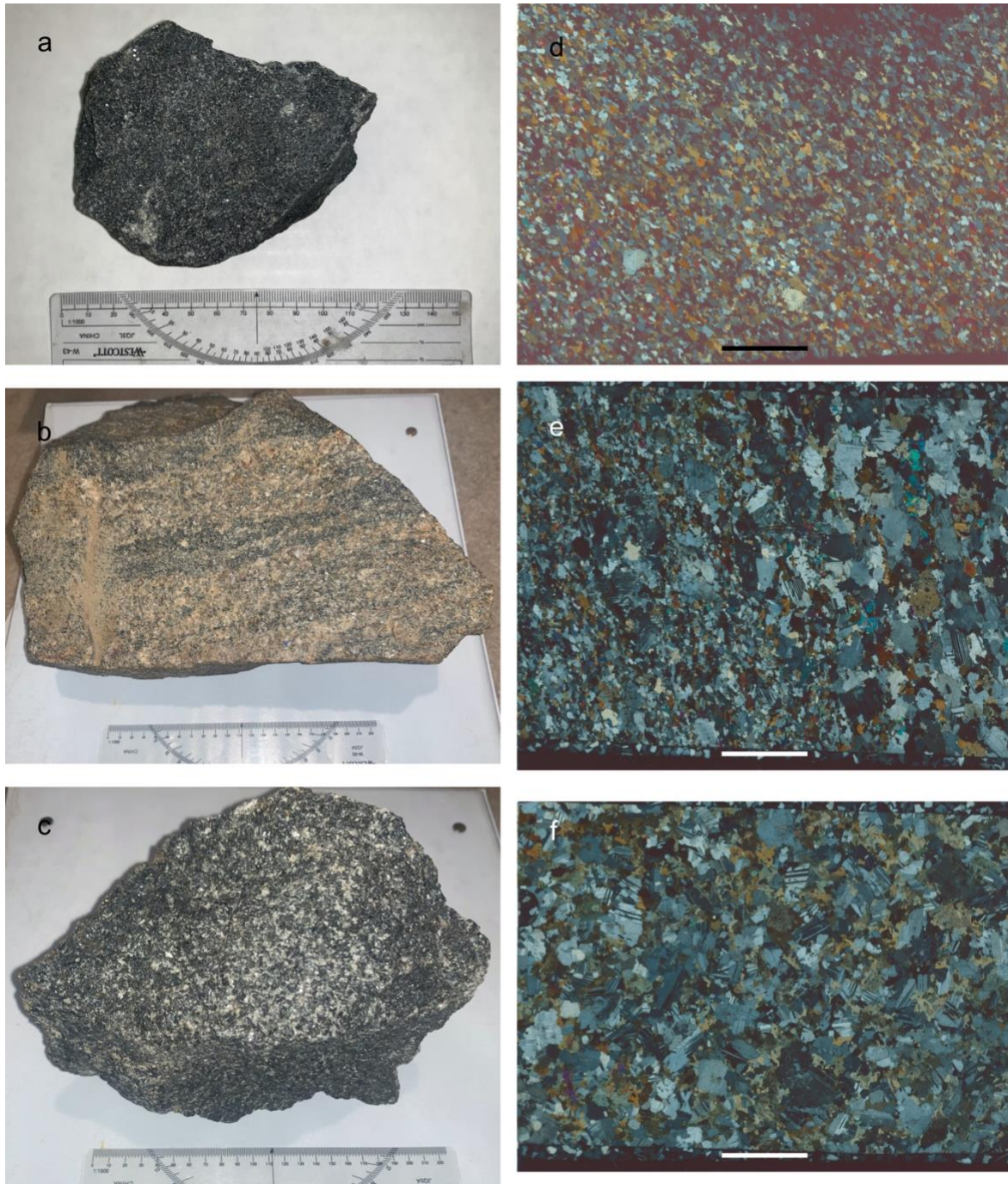


Figure 4.3. Hand samples a) FA10-03m, b) FA18-01, and c) FA18-03. Thin section images for the respective hand samples d) FA10-03, e) FA18-01a, and f) FA18-03. Each scale bar in the thin section image represents 10 mm.

from the plagioclase grains and the removal of grains whose boundaries intersect the boundary of the area considered. Samples FA10-03m, FA18-01a, and FA18-03 (Fig. 4.3) were chosen as end

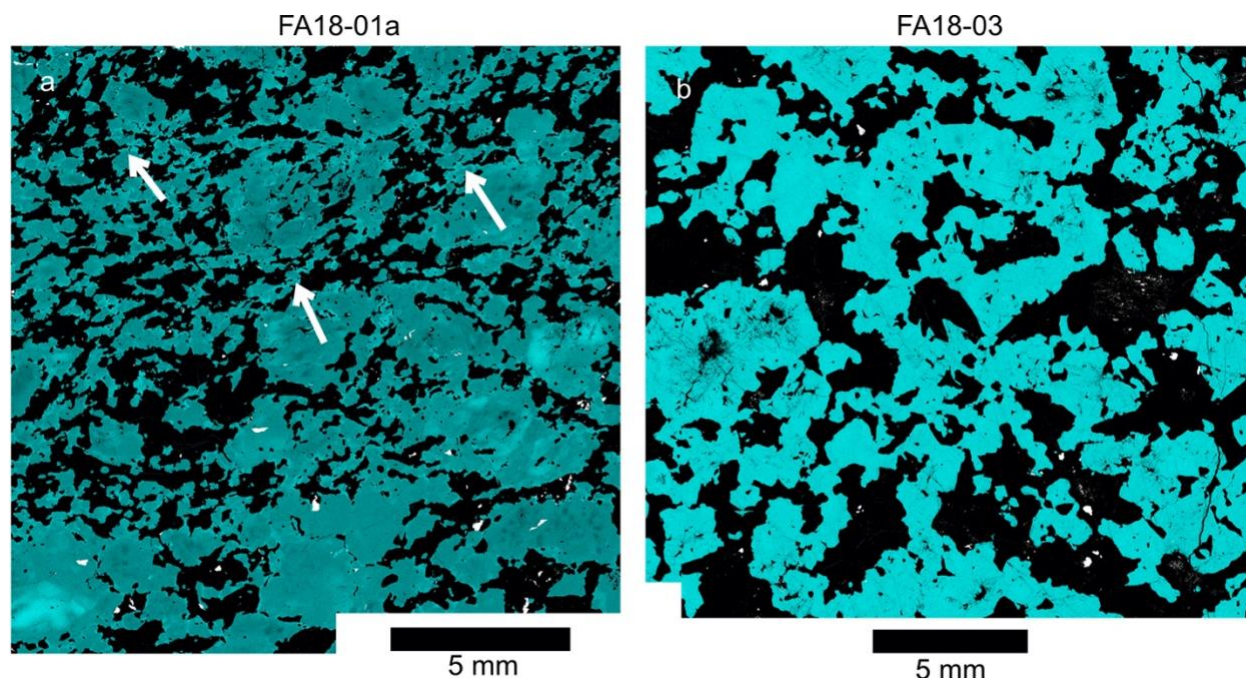


Figure 4.4 QEMScan Ca maps of samples (a) FA18-01a and (b) FA18-03. (a) Arrows point to examples of higher Ca content on plagioclase rims. (b) Has no identifiable Ca zoning. This lack of zoning is the dominant result from the samples analyzed.

member representations for the fabrics and textures observed in all samples. The grain sizes and aspect ratios for the three samples are listed in table 4.2. The data for the remaining samples can be found in the supplemental materials.

We conducted QEMscan analysis to determine Ca zoning in plagioclase on all samples. The results show little to no growth zoning in the crystals with minor amounts of higher Ca zoning on some rims (Fig. 4.4a). Of the samples analyzed, only FA18-01a and b, and FA18-04a, and b show any Ca zoning. The lack of Ca zoning in the plagioclase crystals (Fig. 4.4b) is interpreted to be a result of the crystals representing instantaneous solid compositions (Morse, 1976). Chemical differences in the presence of a fluid could explain the higher Ca rims that are observed (Svahnberg & Piazzolo, 2012). Figure 4.4a shows the Ca map for the banded sample, FA18-01a. The bands of tonalite that are present in this outcrop are likely non locally derived tonalitic melt. This could explain the higher Ca rims on the plagioclase.

4.6.1 FA10-03m

Sample FA10-03 is an amphibole gabbro-norite collected in the upper reaches of Usno Valley (Fig. 4.1). The modal abundance of phases is listed in table 4.1. Plagioclase is subhedral with both faceted and irregular grain boundaries (Fig. 4.5a), suggesting that the grains continued to grow into melt-filled spaces after contacting other grains (Holness, 2018; Holness et al., 2018; Holness et al., 2019; Holness et al., 2017). Plagioclase grain size varies throughout the sample with large grains that exceed 1 mm, while the average grain size is around 0.4 mm (table 2). Smaller grains display evidence of textural equilibration (Fig. 4.5b), while larger grains maintain a more prismatic shape (Fig. 4.5b). This difference in texture separated by grain size indicates that temperatures needed for textural equilibration were likely not maintained for a prolonged period (Holness, 2018; Holness et al., 2018; Holness et al., 2019; Holness et al., 2017). While there are mechanical twins present in the form of bent and tapering twins (Fig. 4.3a), there are also undeformed growth twins (Figure 4.2a) indicating that this sample underwent only minor amounts of deformation.

Table 4.1. Composition of selected samples

Sample number	rock type	Modal abundances (%)					
		plagioclase	orthopyroxene	clinopyroxene	amphibole	quartz	Oxides
FA10-03m	amphibole gabbro-norite	45.7	7.6	2.8	40.5	1.1	1.1
FA18-01a	dark band	56	5.43	4.29	19.43	8.86	6
FA18-01a	light band	63.1	8.57	8	6.57	10.86	2.86
FA18-03	amphibole norite	57.4	9.1	1.4	27	1.2	0.746

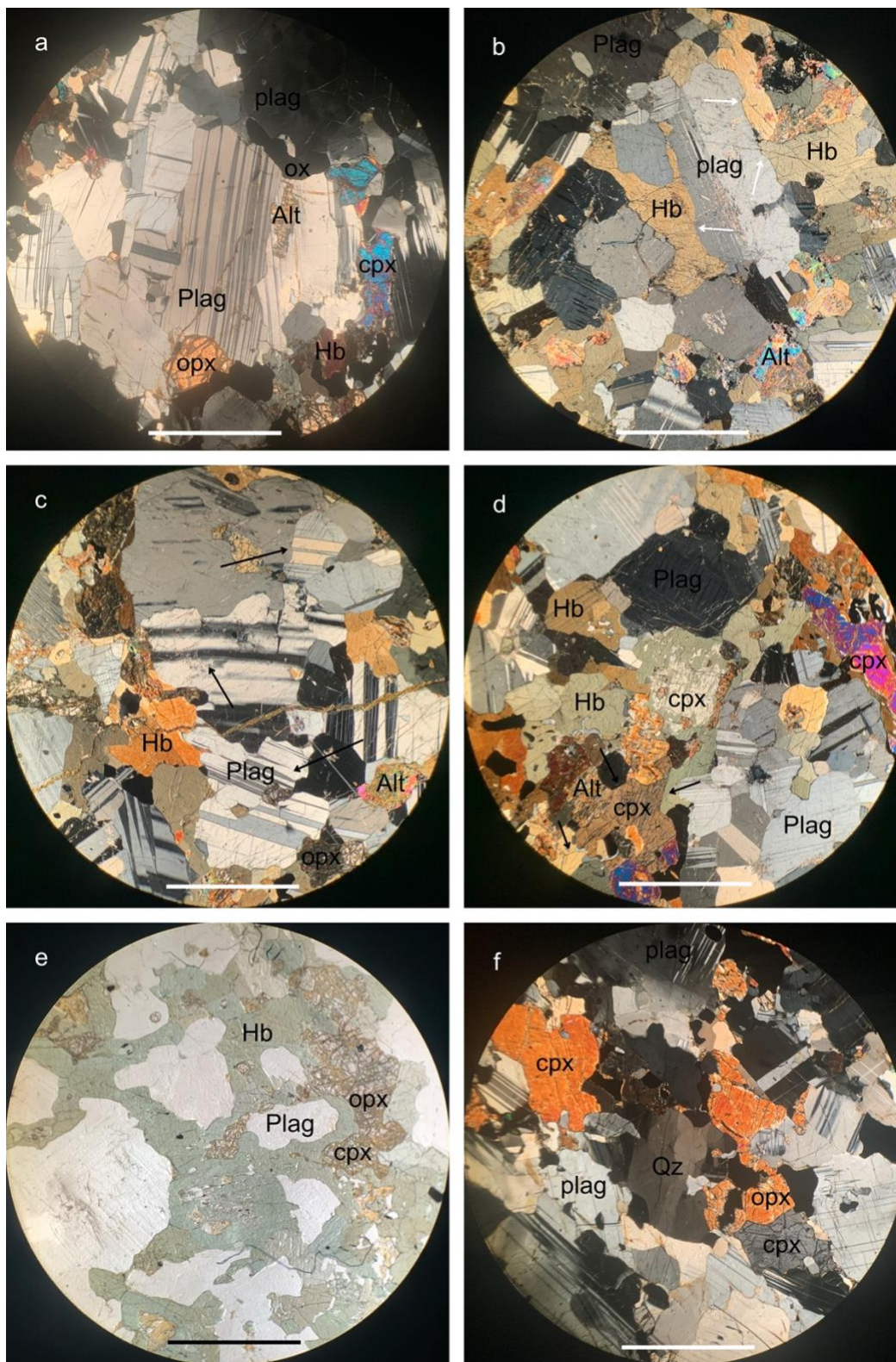


Figure 4.5. Photomicrographs of Famatinian samples. Only frame e is under plane polarized light. The others are under crossed polarized light. the scale bar is 0.5 mm in all subfigures. (a) shows a cluster of plagioclases (plag) whose grains continued to grow into melt filled pores after

agglomerating from sample FA18-01a. Some textural equilibration of the smaller grains is present at triple junctions and in rounded convex grain boundaries. (b) Sample FA18-03 with plagioclase showing faceted grain boundaries that transition into irregular grain boundaries. Arrows show the location of the transition. Interstitial hornblende (Hb) is also present. Pyroxenes show alteration (Alt). (c) Sample FA18-03 with examples of the types of twins found in plagioclase. Arrows from top to bottom show growth twins, bent twins, and tapering twins. (d) Sample FA18-03 showing hornblende growing on the rims of and consuming clinopyroxene (cpx). We also see examples of faceted grain boundaries between pyroxene-pyroxene contacts, hornblende-hornblende, and some pyroxene-hornblende contacts (arrowed). (e) In this image of sample FA18-03 we see an example of some of the interconnected yet discrete grained hornblende networks. Image is in plane polarized light to highlight the interconnected hornblende network. Hornblende is seen as an interstitial phase and growing on the rims of clinopyroxene and orthopyroxene (opx). (f) Example of a quartz grain displaying mild subgrains with undulating extinction from sample FA18-01a.

Amphibole replaces both OPX and CPX on crystal rims (Fig. 4.5d) as an interstitial phase (Fig. 4.5b-d) and as a primary phase (Figure 4.5d). The amphibole grain size varies with a few large grains that are over 1 mm and an average grain size of around 0.4 mm (table 2). Amphibole grain boundaries are subhedral to anhedral with primocrysts tending more to subhedral, and interstitial and pyroxene rim growth tending to be more anhedral. Despite the late formation of amphibole relative to plagioclase, texturally equilibrated triple junctions seem to be more pervasive in amphibole. The variety of ways in which amphibole crystallized suggests that it was one of the last phases to form and that it experienced minimal plastic deformation and overprinting. However, there is a strong SPO preserved in both the amphibole and plagioclase as can be seen in thin section (Fig. 4.3d) and quantified with rose diagrams (Fig. 4.6c,e). Clinopyroxene is generally larger than orthopyroxene with orthopyroxene being slightly more abundant. Both phases of pyroxene tend to be euhedral, but there are some examples of subhedral grains with amphibole present on the rims.

4.6.2 *FA18-01a*

Sample FA18-01 displays alternating light and dark colored bands (Fig. 4.3b). Thin section FA18-01a was cut at the transition between two bands. This sample was collected in Usno Valley (Fig. 4.1). Table 4.1 lists the mineral modes as a product of the different band composition.

Table 4.2. Grain size and aspect ratio of the main silicate phases from the selected samples.

sample number	phase	grain size (μm)				aspect ratio				Number of grains
		mode	average	small	large	mode	average	small	large	
FA10-03m	Anorthite	124.6	166.0	62.5	623.0	1.3	1.6	1.0	4.2	1289
	Hornblende	104.1	164.1	64.3	446.6	1.4	1.7	1.0	4.8	925
	Clinopyroxene	80.9	146.9	70.3	560.1	1.4	1.5	1.1	2.8	59
	Orthopyroxene	110.5	132.4	93.5	256.5	1.3	1.6	1.1	2.8	33
	Quartz	76.7	108.8	76.7	126.5	1.2	1.9	1.2	3.0	5
FA18-01a dark band	Anorthite	99.1	199.9	79.3	1091.7	1.3	1.7	1.1	4.5	247
	Hornblende	116.0	191.2	77.6	762.3	1.6	1.8	1.0	3.9	135
	Clinopyroxene	97.2	154.3	97.1	270.0	1.9	1.8	1.1	2.7	41
	Orthopyroxene	85.1	142.3	85.1	332.7	1.5	1.6	1.1	2.8	15
	Quartz	92.0	164.9	69.3	506.9	1.3	1.7	1.1	3.5	73
FA18-01a light band	Anorthite	81.8	270.4	67.9	1830.0	1.5	1.7	1.0	3.4	318
	Hornblende	105.5	191.1	73.4	523.2	1.4	1.9	1.2	4.1	72
	Clinopyroxene	149.2	221.8	79.9	757.5	1.3	1.7	1.0	3.4	100
	Orthopyroxene	101.1	156.3	74.7	560.8	1.6	1.6	1.1	2.9	66
	Quartz	104.4	172.3	66.3	893.8	1.4	1.7	1.1	3.9	117
FA18-03	Anorthite	144.8	364.9	123.4	1354.1	1.2	1.5	1.0	3.8	140
	Hornblende	155.3	261.2	109.4	682.0	1.6	1.8	1.0	4.0	227
	Clinopyroxene	141.7	335.6	141.7	739.2	1.7	1.7	1.1	2.4	17
	Orthopyroxene	132.8	204.1	132.8	277.2	1.5	1.5	1.4	1.5	3
	Orthoclase	186.8	193.8	186.8	200.7	1.4	1.7	1.4	2.0	2

Examination of the thin section of this sample reveals that the bands differ by the size of the plagioclase grains (table 4.2) and the abundance of amphibole (table 4.1). Overall, the darker bands contain smaller plagioclase grains with some clusters of larger grains, and a larger modal abundance of amphibole.

The mineralogy is similar between the two bands with the primary minerals being plagioclase, amphibole, orthopyroxene, clinopyroxene, and quartz. The modal abundances for each phase can be found in table 4.1. Average grain size for plagioclase is 0.1 mm and 1.1 mm is the maximum grain size in the dark bands, while 0.27 mm with a maximum grain size of 1.8 mm in the light bands (table 2). Plagioclase in both bands have an average aspect ratio of 1.7 (table 2). The grain boundary geometry for plagioclase is subhedral elongate grains with faceted boundaries that transition into irregular grain boundaries (Fig. 4.5a). This geometry indicates a preservation of magmatic contacts where growth continued into melt pockets (Holness et al., 2018; Holness et al., 2019). Some smaller grains provide indications of minor textural equilibration in triple junction and grain boundary geometries, but these indicators are less common in larger grains. Both mechanical twins present as bent and tapering twins, and growth twins are present in large and small plagioclase crystals (Fig. 4.5c). Undulatory extinction is seen in some of the larger plagioclase grains, and a strong SPO is present in both the large and small non-equant plagioclase grains (Figs. 4.7c, 4.8c).

Amphibole presents as primocrysts (rarely), an interstitial phase, and on the rims of and consuming pyroxene. The average grain size and aspect ratio for amphibole is similar in the darker and lighter bands at around 1.9 mm and 1.8 respectively (table 2). However, the maximum grain size is larger in the darker band at 0.76 mm compared to 0.52 mm in the lighter band (table 2). Amphibole in the lighter bands occurs only as interstitial phases or on the rims of pyroxenes. As primocrysts in the darker band, amphibole is subhedral with faceted faces that parallel twin boundaries and cleavage planes. As interstitial phases or as rim growths, amphibole is subhedral to anhedral, forming straight grain boundaries only when in contact with a faceted grain. A few

amphibole grains exhibit undulatory extinction. Elongate grains of amphibole in both light and dark bands display a clear SPO in thin section (Figs. 4.7e, 4.8e).

Orthopyroxene is slightly more abundant than clinopyroxene in both bands (table 4.1), but both pyroxenes are more abundant in the lighter bands than in the darker bands. Both pyroxenes are euhedral to subhedral when amphibole is not present on the rims, but subhedral to anhedral with amphibole growth on rims. Undulatory extinction is present in pyroxene grains. Quartz is pervasive in both types of bands (table 4.1) as anhedral interstitial phases. Quartz displays minor subgrain formation and undulose extinction (Fig. 4.5f).

4.6.3 *FA18-03*

Sample FA18-03 is an amphibole gabbro norite (Fig. 4.3c) collected in Usno Valley. This sample has a near-isotropic fabric composed of plagioclase, clinopyroxene, orthopyroxene, amphibole, and minor amounts of quartz (Fig. 4.3f). The modal abundances of each phase are listed in table 4.1.

Plagioclase orientations are randomly distributed in this sample, and we see populations of both equant and elongate plagioclase grains. The average grain size is .36 mm with an average aspect ratio of 1.5 (table 2). The maximum grain size is 1.3 mm. The minimum and maximum aspect ratio is 1.2 and 3.4 respectively (table 2). Grain boundaries are subhedral to anhedral across all orientations. Small plagioclase grains have both dihedral angles at triple junctions, and convex grain boundaries that indicate textural equilibration. Larger grains have faceted grain boundaries that transition into irregular grain boundaries, suggesting continued growth into a pocket of interstitial melt after contact with other grains. Plagioclase displays tapered and bent deformation twinning, as well as straight growth twins.

Amphibole occurs as interstitial phases, it is found on the rims of and consuming pyroxene (Fig. 4.5d). The grain boundary geometry is subhedral to anhedral. We find minimal textural equilibration on amphibole grain boundaries and triple junctions. Faceted faces transitioning into irregular grain boundaries occur when amphibole is in contact with plagioclase (Fig. 4.5b), suggesting that the two were growing simultaneously. Amphibole often fills large, interconnected networks of interstitial spaces as smaller, touching individual grains (Fig. 4.5e). Because amphibole forms later during the crystallization of magma, we can infer that enough pore space was present to accommodate amphibole crystallization. Both OPX and CPX are altered along grain boundaries, fractures, and cleavage planes. However, the alteration does not affect the amphibole grains that are in contact with and/or grow on the rims of the pyroxene. The shape of the grain boundaries for unaltered pyroxene are subhedral to anhedral. Quartz is found as inclusions in amphibole and along amphibole grain boundaries as an interstitial phase, suggesting that amphibole formation enriched the melt in silica, which allowed for the crystallization of quartz in the remaining interstitial spaces.

4.6.4 *Summary*

The evidence presented in this section suggests that magmatic primocrysts remain relatively pristine in these samples. We therefore infer from our textural analyses that the samples are likely to preserve fabric and microstructural indicators of melt extraction mechanisms.

4.7 FABRIC QUANTIFICATION

Foliations in the mafic and tonalitic bodies, whether formed by gravitational settling, magmatic flow, or deformation fabric, have variable spatial orientations that depend on the orientation of the local shear zone that exhumed the individual cumulate bodies. However, the solid-state fabrics

formed in high strained zones parallel, and transition from the magmatic fabric. The general trend of the foliations is NNW-SSE and steeply dips to either the west or east (Cristofolini et al., 2014; Otamendi, Vujovich, et al., 2009).

4.7.1 FA10-03m

Plagioclase [100] axes and poles to the (010) plane are parallel to foliation. Poles to the (001) plane form a strong point maximum that spreads out into a weak girdle. The (001) is almost 90° apart from the (010) point maximum (Fig. 4.6b). The BA index defined by Satsukawa et al. (2013) is 0.3, corresponding to B-type fabric (Table 4.3). Plagioclase misorientation axes forms point maxima that corresponds to the [100] axes (Fig. 4.6b). The shape preferred orientation diagram (SPO) shows a strong correlation between grain shape and the orientation of [100] and (010). Poles to the (100) of hornblende display strong point maxima, whereas [001] axes form a girdle, suggesting that the foliation is defined by (100) planes. The (010) poles are randomly distributed (Fig. 4.6d). Hornblende misorientation axes form strong point maxima that correspond with the [001] axes. Similar to plagioclase, hornblende shape preferred orientation data strongly correspond with its CPO.

Table 4.3. Textural parameters for selected samples

Sample number	Phase	N	BA	J-index	PFJ 100	PFJ 010	PFJ 001	M-index	CPO
FA10-03m	Plagioclase	2993	0.34	3.15	1.19	1.22	1.07	0.07	B
	Amphibole	2496		2.1	1.27	1.02	1.23	0.04	
FA18-01a dark band	Plagioclase	422	0.23	11.04	1.25	1.33	1.18	0.07	B
	Amphibole	158		6.01	1.35	1.19	1.36	0.04	
FA18-01a light band	Plagioclase	665	0.26	5.01	1.13	1.11	1.07	0.05	B
	Amphibole	80		10.23	1.43	1.32	1.35	0.04	
FA18-03	Plagioclase	716	0.65	4.39	1.15	1.07	1.11	0.03	A
	Amphibole	916		2.55	1.09	1.06	1.1	0.01	

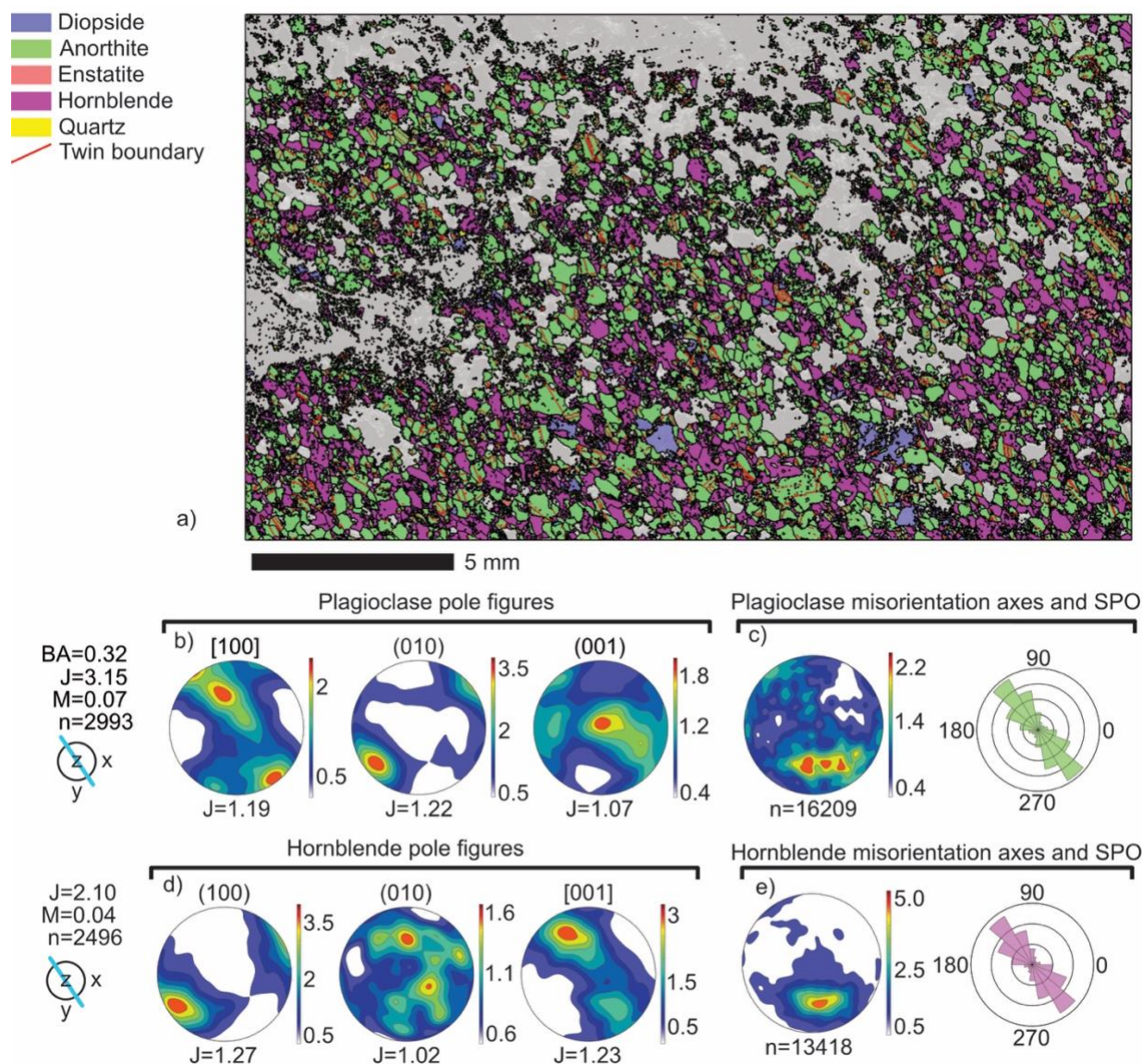


Figure 4.6. Electron Backscatter Diffraction (EBSD) orientation results for sample FA10-03m. a) Phase map of the EBSD scanned area. b) Lower hemisphere equal-area projections of plagioclase [100] axis, and (010) and (001) poles to planes. c) Plagioclase misorientation axis and shape preferred orientation rose diagram. d) Lower hemisphere equal-area projection of hornblende (100) and (010) poles to planes, and [001] axis. e) Hornblende misorientation axis and shape preferred orientation rose diagram. Blue lines intersecting the orientation reference indicate the foliation direction.

Microstructural analysis presented by pole figures shows a weak dispersion of [100] and (001) around (010) poles in some plagioclase grains (Fig. 4.11a). A similar amount of misorientation is present in hornblende (Fig. 4.12a). However, the amount of misorientation observed in both phases

is minimal and suggests this sample saw limited plastic deformation. We can qualify with figures 4.11a and 4.12a that the deformation is similar across two phases that formed at different times within the magma, suggesting that the deformation event happened after the crystallization of the later phase. We can further quantify that qualification with KAM analyses. KAM histograms, which calculate and show the amount of misorientation associated with each dislocation, are presented in figure 4.13. The histograms are similar for each of the three phases: plagioclase, hornblende, and quartz (Fig. 4.13d). The similarity indicates that the deformation event that formed the dislocations likely happened after the crystallization of quartz. Furthermore, quartz was likely the last phase to form in the system, indicating that the deformation event that formed the misorientations was likely subsolidus.

4.7.2 *FA18-01a*

Despite the visual differences in grain size and modal abundances between the two bands of this sample, the fabric results are quite similar. Because of this, the results from the two bands are presented together and the misorientation axes data is calculated from the total section, rather than from the individual bands.

Plagioclase [100] axes and (010) planes are parallel to foliation, while poles to the (001) planes are randomly distributed. The [100] axes form two point maxima that continue into a girdle, while the (010) planes define the foliation (Fig. 4.7b, 4.8b). The BA index is 0.23 for the dark band and 0.26 for the light band, which corresponds to B-type fabric for both bands (Satsukawa et al., 2013). Plagioclase misorientation axes (Fig. 4.9a) form point maxima that correspond to the [100] axes (Fig. 4.7b, 4.8b). The shape preferred orientation diagram displays a strong correlation between grain shape and the orientation of [100] axes and (010) planes. Poles to the (100) of hornblende show strong point maxima whereas the [001] axis forms a girdle, suggesting that the

foliation is defined by (100) planes. The (010) poles are randomly distributed (Fig. 4.7d, 4.8d).

Hornblende misorientation axes form strong point maxima that correspond to the [001] axis.

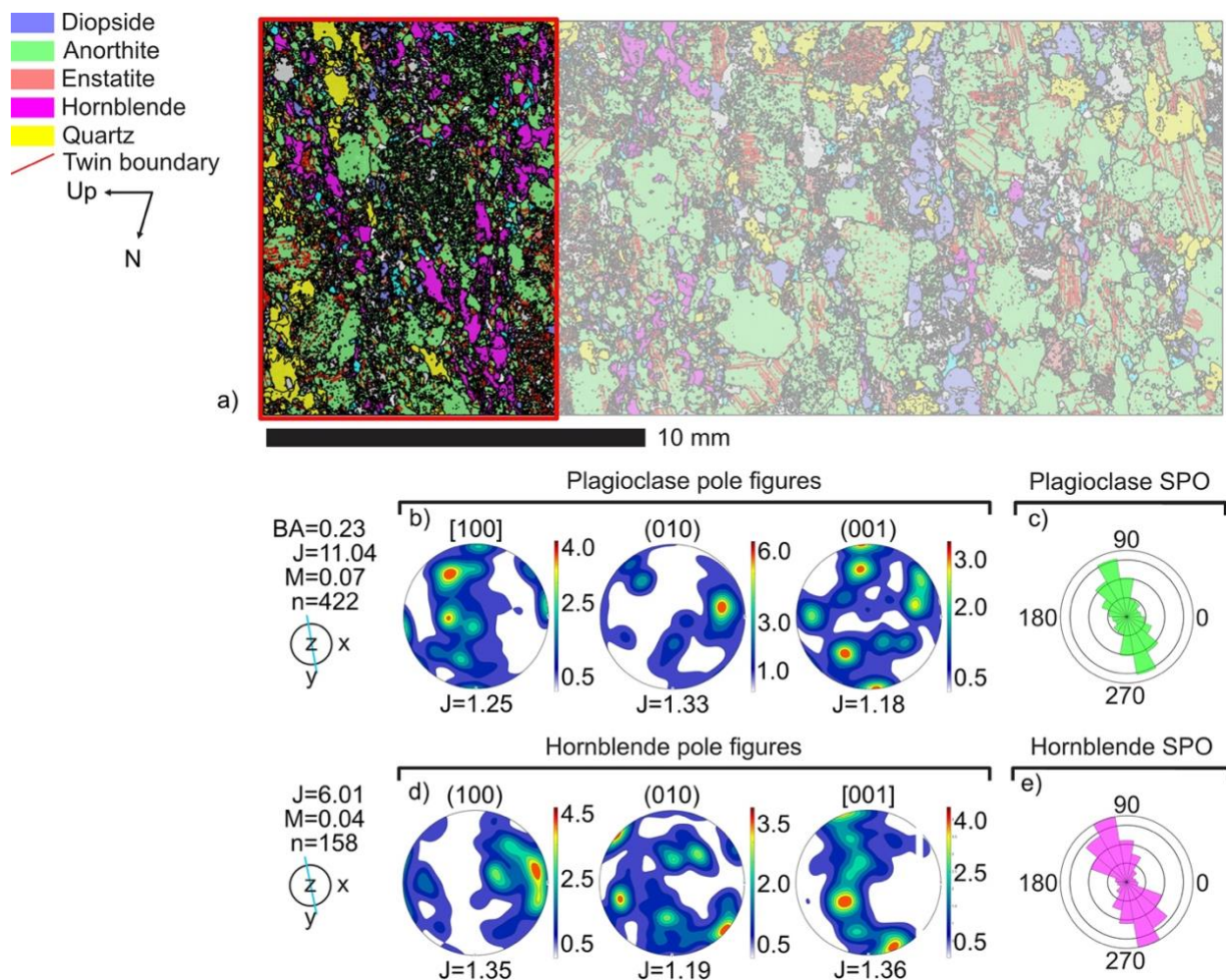


Figure 4.7. Electron Backscatter Diffraction (EBSD) orientation results for sample FA18-01a dark band. a) Phase map of the EBSD scanned area. b) Lower hemisphere equal-area projections of plagioclase [100] axis, and (010) and (001) poles to planes. c) Plagioclase shape preferred orientation rose diagram. d) Lower hemisphere equal-area projection of hornblende (100) and (010) poles to planes, and [001] axis. e) Hornblende shape preferred orientation rose diagram. Blue lines intersecting the orientation reference indicate the foliation direction.

Similar to plagioclase, hornblende's SPO strongly corresponds to its CPO.

We observe some differences in the microstructural analyses between the two bands. The larger plagioclase grains in the lighter band show a large dispersion of poles then around (010) and (001) with a pole of rotation at [100] (Fig. 4.11c). Smaller plagioclase grains in the darker band

have a lesser amount of dispersion with pole of rotation seen in the pole figures around [100] and dispersion of poles in (010) and (001) (Fig. 4.11b). crystal lattice distortions are less developed in

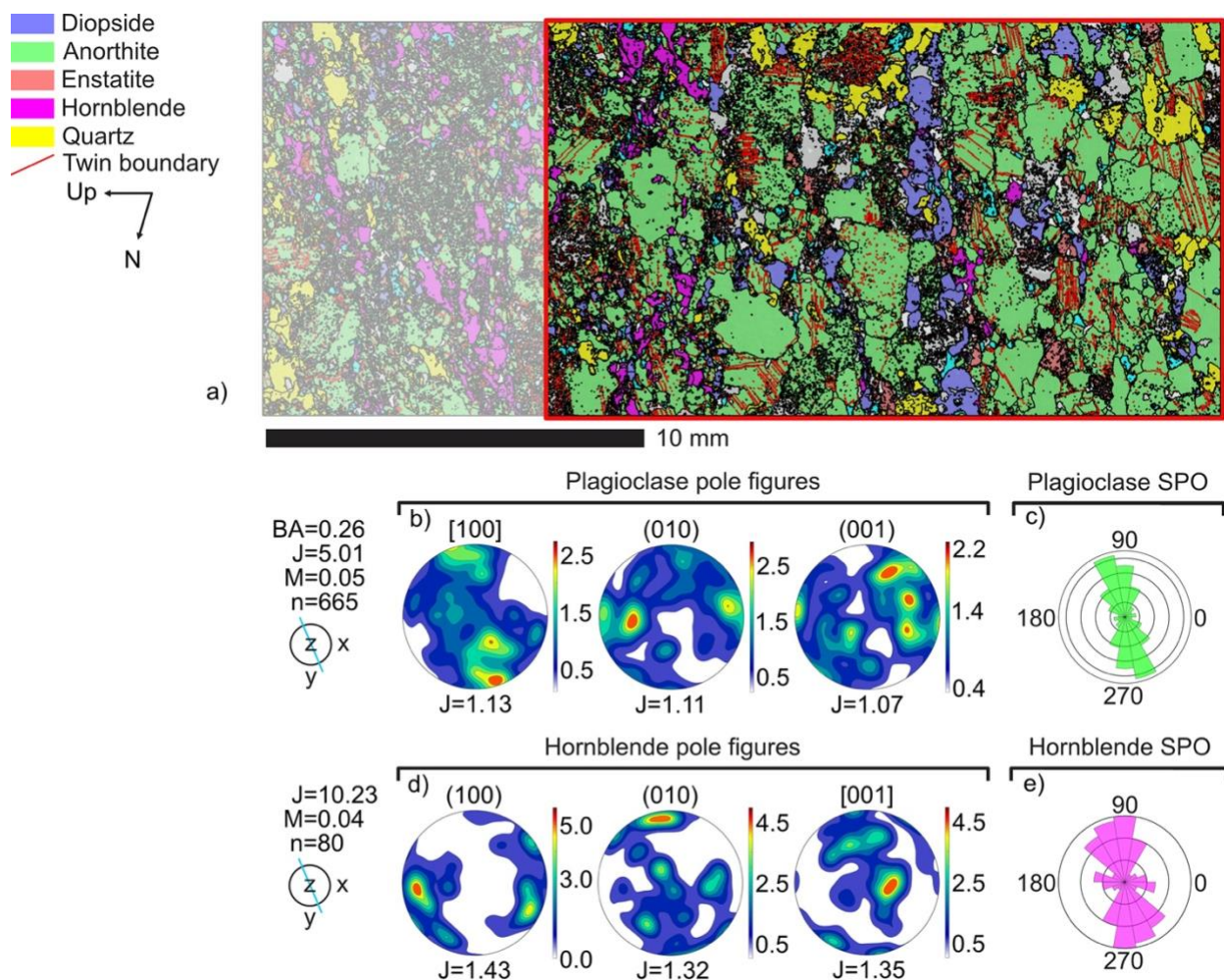


Figure 4.8. Electron Backscatter Diffraction (EBSD) orientation results for sample FA18-01a light band. a) Phase map of the EBSD scanned area. b) Lower hemisphere equal-area projections of plagioclase [100] axis, and (010) and (001) poles to planes. c) Plagioclase shape preferred orientation rose diagram. d) Lower hemisphere equal-area projection of hornblende (100) and (010) poles to planes, and [001] axis. e) Hornblende shape preferred orientation rose diagram. Blue lines intersecting the orientation reference indicate the foliation direction.

the smaller hornblende crystals in the lighter band as seen in the sharp color boundary of figure 4.12b. Quartz appears to have more lattice distortion than the hornblende (Fig. 4.12b). In the darker

band, both hornblende and quartz preserve minimal lattice distortions. However, unlike in the lighter band, we see a well-developed alignment of distortions for both quartz and hornblende with a sharp color boundary that runs almost perpendicular to the long axes of the crystal (Fig. 4.12c). The KAM histograms show similar distributions of misorientations not only for plagioclase,

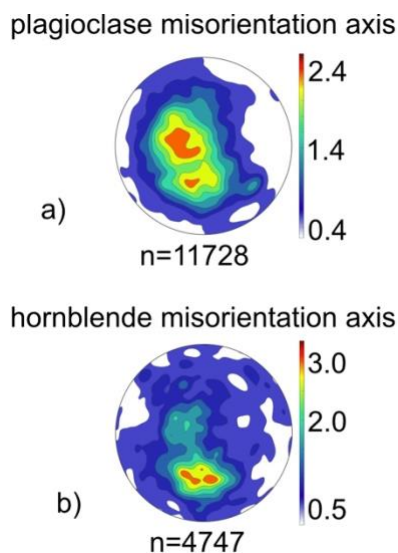


Figure 4.9. Plagioclase (a) and hornblende (b) misorientation axes for sample FA18-01a. The analyses of misorientation axes are not segregated into the distinct composition bands.

hornblende, and quartz in each band, but also between the two bands (Fig. 4.13a, 4.13b). This result suggests that the deformation event happened after segregation of the bands and the crystallization of quartz.

4.7.3 FA18-03

Plagioclase shows a point maximum that develops into a girdle for the [100] axis and a random distribution for both (010) and (001) poles to planes (Fig. 4.10b). Despite the girdle in the [100] axis, no foliation is apparent. The BA index is 0.65, corresponding to an A-type fabric (Satsukawa et al., 2013). The misorientation axis has a point maximum that correlates to the [100] axis, but

overall has a random distribution (Fig. 4.10c) There is a weak SPO that does not correlate to the girdle formed by [100] (Fig. 4.10c). Hornblende has a point maximum that continues into a weak girdle, while the (100) and (010) poles display a random distribution (Fig. 4.10d). Like the plagioclase, hornblende shows no foliation. We find a random distribution in the misorientation axis, but unlike plagioclase, a shape preferred orientation that correlates with the [001] axis (Fig. 4.10e).

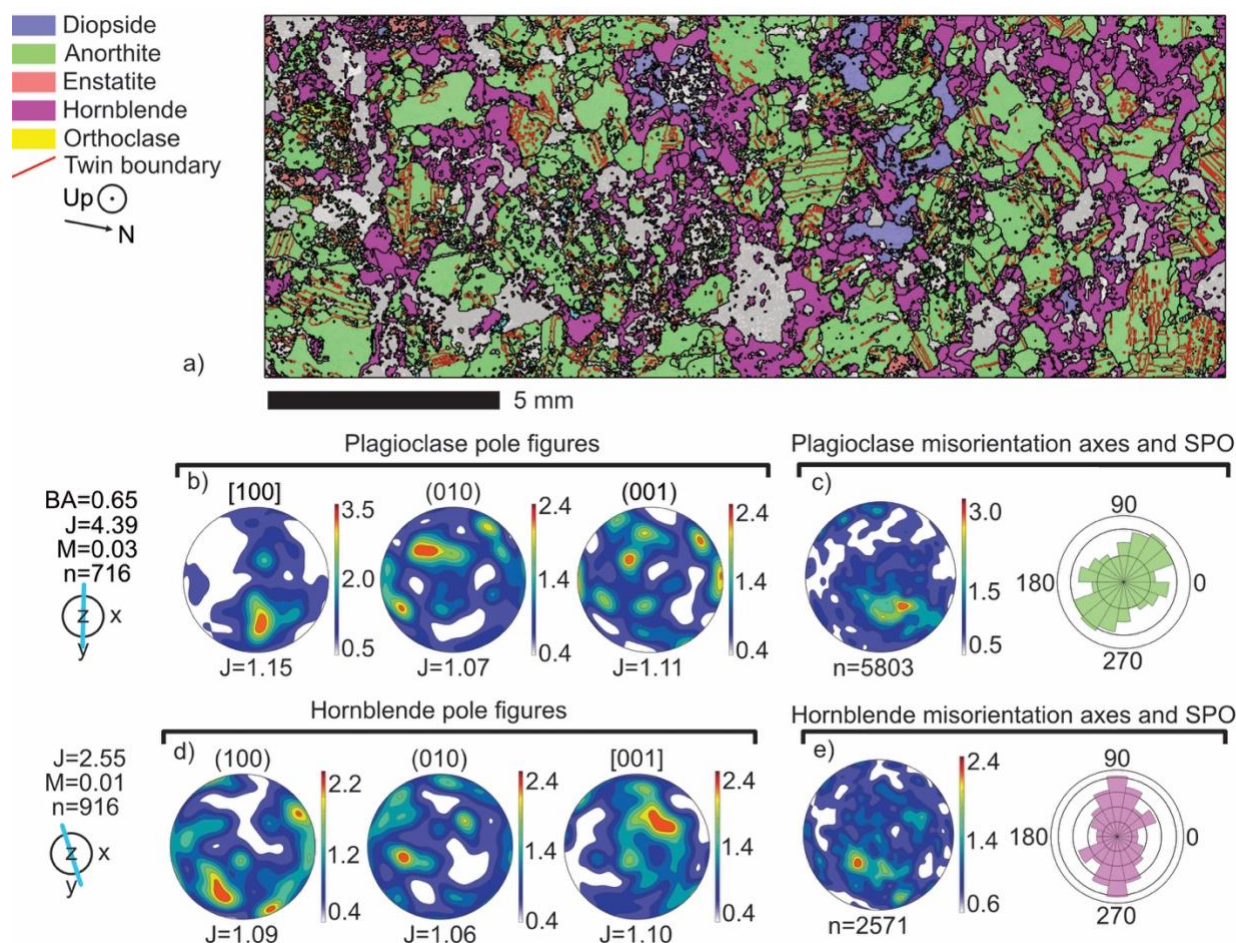


Figure 4.10. Electron Backscatter Diffraction (EBSD) orientation results for sample FA18-03. a) Phase map of the EBSD scanned area. b) Lower hemisphere equal-area projections of plagioclase [100] axis, and (010) and (001) poles to planes. c) Plagioclase misorientation axis and shape preferred orientation rose diagram. d) Lower hemisphere equal-area projection of hornblende (100) and (010) poles to planes, and [001] axis. e) Hornblende misorientation axis and shape preferred orientation rose diagram. Blue lines intersecting the orientation reference indicate the foliation direction based on the girdles found for the [100] and [001] axes for plagioclase and hornblende respectively.

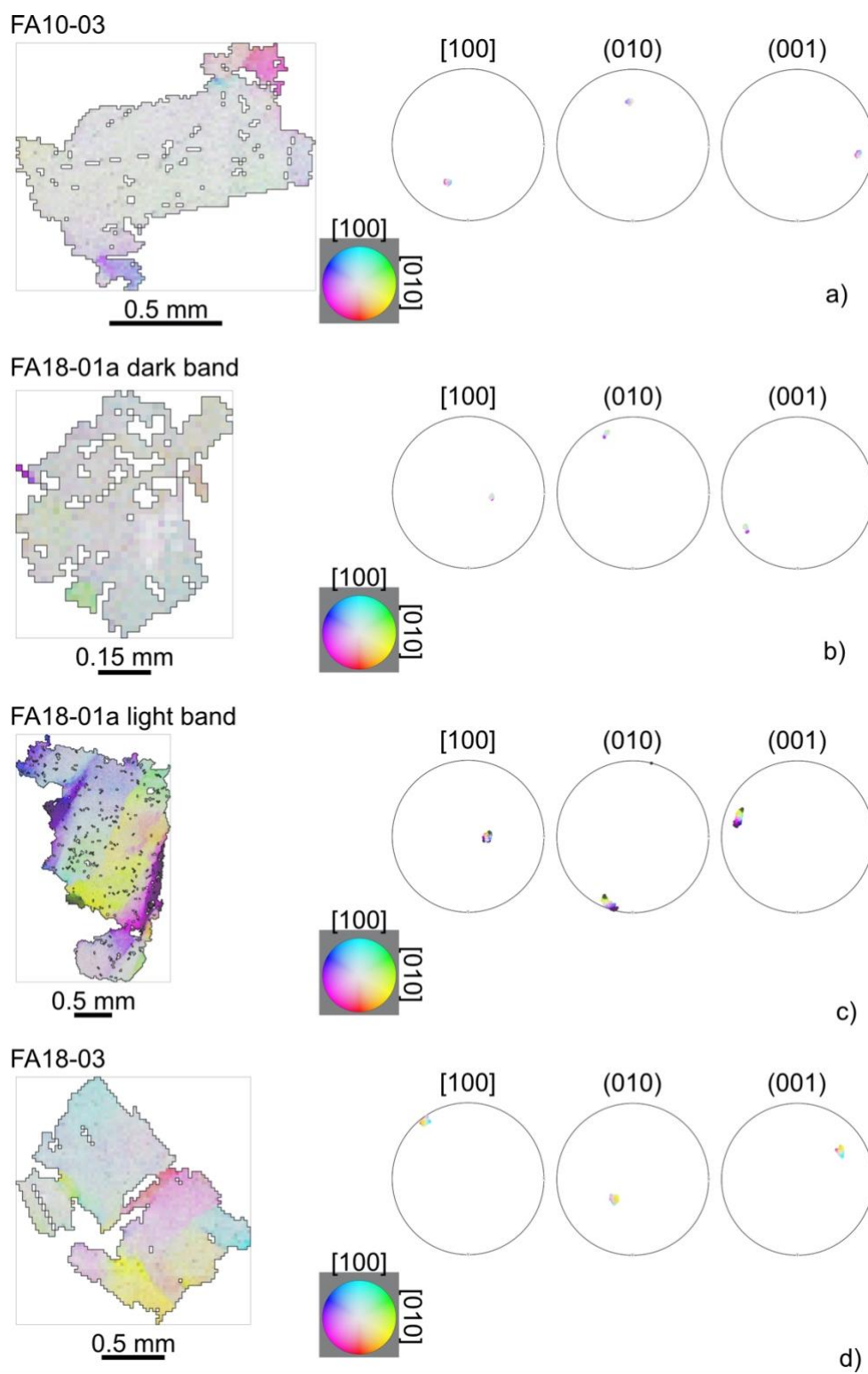


Figure 4.11. Pole figures for individual plagioclase grains from each sample. The grain maps are colored to the inverse pole figure (IPF) key which is referenced to the mean orientation of the

grain. The color scale, located at the bottom right of each grain map, is adjusted so that light grey is 0° and dark grey is 10° or more of misorientation. Sharp boundaries between colors in the grain maps indicate internal lattice distortions. a) FA10-03 shows a minor amounts of internal lattice distortion. The corresponding pole figures show a minor amount of dispersion of poles in [100] and (001), with a pole of rotation at (010). b) Grain from FA18-01a dark band shows little to no internal lattice distortions in the grain map and minor amounts of dispersion of poles in the (010) and (001) pole figures with a pole of rotation at [100]. c) This grain from the light band of sample FA18-01a shows several sharp color transitions indicating internal lattice distortions, however, total misorientation remains below 10° . Pole figures show dispersion of poles in (010) and (001), with a pole to rotation in [100]. d) This plagioclase from sample FA18-03 displays several transitions of colors across sharp boundaries indicating minor amounts of internal lattice distortions. There seems to be a small amount of dispersion of poles in [100] and (001) with a pole of rotation at (010).

Inverse pole figure maps and pole figure projections of individual plagioclase grains reveal a dispersion of poles in both [100] and (001) with (010) the pole of rotation (Fig. 4.11d). The dispersions are minimal, but sharp boundaries between colors of the represented grain in figure 4.11d indicate the presence of internal lattice distortion. Hornblende displays minimal internal lattice distortions with the color boundaries being more diffuse indicating lattice distortions are not as well developed as in the plagioclase (Fig. 4.11d, 4.12d). The KAM histogram for plagioclase and hornblende (Figure 4.13c) shows that the distribution of misorientations associated with dislocations is similar between the two phases, indicating that the deformation occurred after the formation of hornblende.

4.8 DISCUSSION

4.8.1 *Crystallization, accumulation, and igneous fabric formation*

Major element geochemistry shows early depletion of CaO with minor changes in Al_2O_3 , which indicates that the formation of clinopyroxene preceded plagioclase crystallization. Crystallization of anhydrous plagioclase, clinopyroxene, and later orthopyroxene increased the H_2O content of the melt from an initial concentration of around 1 or 2 wt.% to 3 or 5wt.% (Otamendi et al., 2010).

This increase in H₂O allowed for the formation of hornblende (Claeson & Meurer, 2004; Otamendi et al., 2010). Orthopyroxene and late-stage crystallization of hornblende created a differentiation trend that increased SiO₂ and decreased MgO in the remaining melt. Small interstitial quartz grains found within grains, and on the grain boundaries, of hornblende are evidence that the SiO₂ content of the melt was sufficiently high enough to form quartz. The decrease in MgO corresponds with the increase in the mass fraction of incompatible oxides such as Na₂O, TiO₂, and K₂O (Otamendi et al., 2010). Increasing the concentration of SiO₂ along with the other incompatible oxides changed the composition of the remaining melt from gabbroic to tonalitic.

The formation of hornblende was an essential step in increasing the SiO₂ in the remaining melt; therefore, the extraction of tonalitic melt only occurred after hornblende crystallization. The pervasiveness of hornblende throughout the mafic complex and the interconnecting network of interstitial hornblende grains (Fig. 4.5e) suggests that there was enough pore space to accommodate hornblende growth. Furthermore, when comparing the abundances of incompatible trace elements, the amount in the mafic cumulates of Sierra Valle Fértil is lower than both primitive arc magmas and MORB, indicating that melt was removed from the mafic cumulates (Otamendi et al., 2010). The lines of evidence presented in this section indicates that an evolved, silica enriched, tonalitic melt was extracted from the pore spaces of a gabbroic cumulate mush.

4.8.2 *The origin of plastic deformation in the cumulate crystals*

The deformation of plagioclase is apparent in all samples, and some of the larger grains show the greatest occurrence of dislocations. Examples of this are seen in figures 4.11c and 4.11d where sharp color boundaries within the plagioclase grains mark the presence of lattice distortions. Sharp color boundaries indicating internal lattice distortions can be seen in hornblende (Fig. 4.12a,c,d) and quartz (Fig. 4.12b,c). Furthermore, the correlation between the plagioclase and hornblende

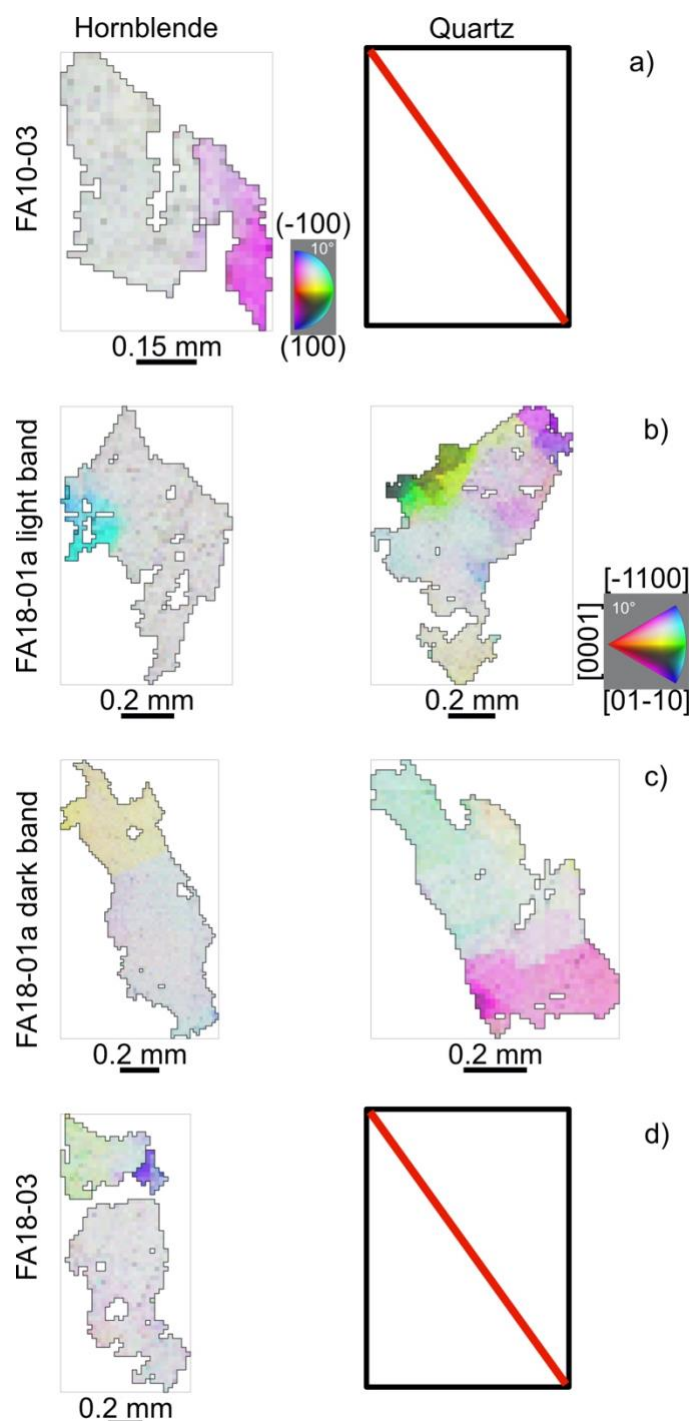


Figure 4.12. Misorientation figures colored to inverse pole figure (IPF) key for hornblende and quartz and are referenced to the mean orientation of each grain. The color scale, located at the bottom right of the hornblende grain for all hornblende in a) and to the bottom right of the quartz grain for all quartz in b), is adjusted so that light grey is 0° and dark grey is 10° . Sharp boundary between colors indicate crystal lattice distortions in the form of dislocations. Boxes with red lines indicate either that quartz was not analyzed (FA18-03) or that quartz was too small to get a proper misorientation figure (FA10-03). a) Sample FA10-03 hornblende shows minor amounts of misorientation with a good alignment of dislocations. b) Sample FA18-01a light band hornblende

shows minor misorientation and quartz show misorientations with some alignment of dislocations. c) Sample FA18-01a dark band both hornblende and quartz show minor amounts of misorientation with good alignment of dislocations. d) Sample FA18-03 hornblende shows minor amounts of misorientation.

misorientation axes indicate that the crystals experienced one deformation regime (Reddy & Buchan, 2005; Vukmanovic et al., 2019). Misorientations due to lattice distortions seen in the KAM histograms (Fig. 4.13) have similar distributions across all three phases (plagioclase, hornblende, and quartz) and have similar distributions for all three samples. Therefore, it is likely that the deformation was caused by strain in the solid pluton before localization into discrete shear bands due to terrain accretion (Cristofolini et al., 2014; Otamendi, Vujovich, et al., 2009). Crystal plastic deformation is then not related to pore space reduction and melt extraction.

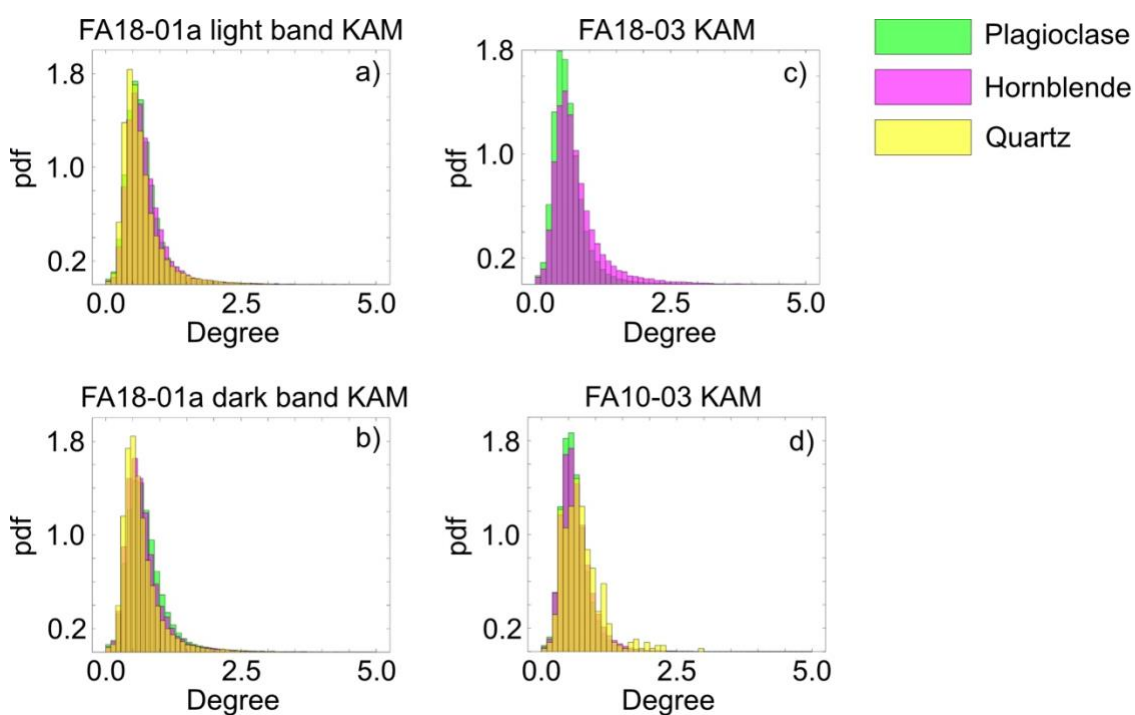


Figure 4.13. Kernel average misorientation (KAM) histograms for plagioclase, hornblende, and quartz. KAM provides the amount of misorientation associated with each dislocation. a) sample FA18-01a light band, b) sample FA18-01a dark band, c) sample FA18-03, and d) sample FA10-03. The peaks for all four histograms are around 1° of misorientation.

4.8.3 *The mechanisms of melt extraction*

There are several potential melt extraction mechanisms at work in Sierra Valle Fértil. The positioning of the tonalitic bodies stratigraphically higher than the gabbroic bodies suggests buoyancy is a potential mechanism. However, the random orientation of the observed melt pathways suggests that the initial expulsion of melt is due to some other process. It is necessary that any explanation for the mechanisms at work extracting melt from the interstitial spaces of the mush accounts for the deep sourcing of melt from the mush that is observed in the outcrops, as well as the near absence of plastic deformation in the crystals. It is unclear if the SPO and CPO preserved in the samples is related to melt extraction. If the melt was extracted due to either viscous compaction or tectonic filter pressing, then the fabric would likely be associated with the melt extraction process. However, both processes reduce pore space by the deformation (plastic or brittle) of the crystals. Mechanical compaction is the only remaining melt extraction mechanism supported by the SPO, CPO, and near lack of crystal-plastic deformation we observe.

The near-random orientation of the melt extraction channels (Fig. 4.2c), and deep sourcing of melt observed in the outcrops of Sierra Valle Fértil suggest that magma recharge could be a potential mechanism for melt extraction. As (Carrara et al., 2020) observed and Petford et al. (2020) suggested, magma recharge causes the mush to dilate. Dilating the mush may eventually lead to brittle failure of the mush, which can lead to the extraction of melt (Petford et al., 2020). This failure process is a potential source of the melt extraction channels, veins, and dikes observed in Sierra Valle Fértil. Brittle failure of the mush cannot explain the observed in situ accumulations of melt that are not accompanied by migration features (Fig. 4.2a); however, mush dilation without brittle failure can explain these melt patches. Shearing of the mush is also a possible mechanism for the formation of the CPO and SPO observed in our samples (Figs. 4.6, 4.7, 4.8, 4.10). As

discussed earlier, shearing of both spherical and non-spherical particles increases the void ratio (Zhao et al., 2018), dilating the mush (Petford et al., 2020). However, by its very nature mush dilation increases pore space, implying that an SPO and CPO cannot be components of pore space reduction. Despite the evidence that mush dilation occurred in Sierra Valle Fértil, we cannot imply that mush dilation explains the expulsion of melt by the reduction in pore space. Therefore, the ideas of mechanical compaction discussed in this paper are not responsible for pore space reduction.

4.9 CONCLUSION

The process of melt extraction from magma mushes is essential for our understanding of arc crust formation. However, we are still unsure of the mechanisms that expel melt from the interstitial spaces of cumulates. The exposed arc cross section of Sierra Valle Fértil provides a unique natural laboratory where we can study the mechanisms of melt extraction at the transition between the mafic lower crust and the tonalitic middle crust. Thorough examination of both microstructural and field evidence from samples and outcrops of Sierra Valle Fértil we can present two main conclusions that inform on potential future research. The first conclusion is that the presence of an SPO and CPO is not necessarily indicative of pore space reduction, and the shear responsible for the formation of the fabric likely resulted in mush dilation. The second conclusion is that shear alone cannot reduce the pore spaces enough to fit our observations of near-complete pore space reduction. Sheared granular material reaches a critical volume fraction given enough strain (Andreotti et al., 2013, pp. 123-125), meaning shear alone cannot reduce the pore space to zero. Therefore, some other, possibly unknown, mechanism is involved in pore space reduction.

To gain a more comprehensive picture of the processes involved in pore space reduction, both numerical and analogue experiments must be conducted. Ideally these would consist of non-

spherical elongate grains in a viscous fluid medium because this would more accurately simulate crystal-rich mushes, and current research under these conditions is sparse. Multiphase numerical models bring greater insight into the kinematics and dynamics of granular systems and provide resources for which we can compare field and petrographic observations.

BIBLIOGRAPHY

- Ai, J., Langston, P. A., & Yu, H.-S. (2014). Discrete element modelling of material non-coaxiality in simple shear flows. *International Journal for Numerical and Analytical Methods in Geomechanics*, 38(6), 615-635. <http://dx.doi.org/10.1002/nag.2230>
- Ancey, C., Andreini, N., & Epely-Chauvin, G. (2013a). The dam-break problem for concentrated suspensions of neutrally buoyant particles. *Journal of Fluid Mechanics*, 724, 95-122. <Go to ISI>://WOS:000318920800007
- Ancey, C., Andreini, N., & Epely-Chauvin, G. (2013b). Granular suspension avalanches. I. Macro-viscous behavior. *Physics of Fluids*, 25(3), 033301. <http://aip.scitation.org/doi/abs/10.1063/1.4793719>
- Anderson, A. T., Swihart, G. H., Artioli, G., & Geiger, C. A. (1984). Segregation Vesicles, Gas Filter Pressing, and Igneous Differentiation. *Journal of Geology*, 92(1), 55-72. <Go to ISI>://WOS:A1984SA07600004
- Andreotti, B., Forterre, Y., & Pouliquen, O. (2013). *Granular media : between fluid and solid*. Cambridge: Cambridge : Cambridge University Press.
- Antony, S. J. (2007). Link between single-particle properties and macroscopic properties in particulate assemblies: Role of structures within structures. *Philosophical Transactions: Mathematical, Physical and Engineering Sciences*, 365(1861), 2879-2891. <http://www.jstor.org/stable/25190630>
- Arbaret, L., Diot, H., & Bouchez, J.-L. (1996). Shape fabrics of particles in low concentration suspensions: 2D analogue experiments and application to tiling in magma. *Journal of Structural Geology*, 18, 941-950.
- Ardill, K. E., Paterson, S. R., Stanback, J., Alasino, P. H., King, J. J., & Crosbie, S. E. (2020). Schlieren-bound magmatic structures record crystal flow-sorting in dynamic upper-crustal magma-mush chambers. *Frontiers in Earth Science*, 8(190). Original Research. <https://www.frontiersin.org/article/10.3389/feart.2020.00190>
- Arvidson, R. S., Beig, M. S., & Lutge, A. (2004). Single-crystal plagioclase feldspar dissolution rates measured by vertical scanning interferometry. *American Mineralogist*, 89(1), 51-56. <Go to ISI>://WOS:000188115000007
- Bachmann, O., & Bergantz, G. W. (2004). On the Origin of Crystal-poor Rhyolites: Extracted from Batholithic Crystal Mushes. *Journal of Petrology*, 45(8), 1565-1582. <https://doi.org/10.1093/petrology/egh019>
- Beane, R., & Wiebe, R. A. (2012). Origin of quartz clusters in Vinalhaven granite and porphyry, coastal Maine. *Contributions to Mineralogy and Petrology*, 163(6), 1069-1082. <https://doi.org/10.1007/s00410-011-0717-1>
- Behn, M. D., & Kelemen, P. B. (2006). Stability of arc lower crust: Insights from the Talkeetna arc section, south central Alaska, and the seismic structure of modern arcs. *Journal of Geophysical Research-Solid Earth*, 111(B11). <https://doi.org/10.1029/2006JB004327>. <Go to ISI>://WOS:000241985900004

- Behringer, R. P., Howell, D., Kondic, L., Tennakoon, S., & Veje, C. (1999). Predictability and granular materials. *Physica D: Nonlinear Phenomena*, 133(1-4), 1-17. <http://www.sciencedirect.com/science/article/pii/S0167278999000949>
- Benn, K., & Allard, B. (1989). Preferred Mineral Orientations Related to Magmatic Flow in Ophiolite Layered Gabbros. *Journal of Petrology*, 30(4), 925-946. <Go to ISI>://WOS:A1989AZ89100004
- Bennett, E. N., Jenner, F. E., Millet, M.-A., Cashman, K. V., & Lissenberg, C. J. (2019). Deep roots for mid-ocean-ridge volcanoes revealed by plagioclase-hosted melt inclusions. *Nature*, 572(7768), 235-239. <https://doi.org/10.1038/s41586-019-1448-0>
- Bergantz, G. W., & Ni, J. (1999). A numerical study of sedimentation by dripping instabilities in viscous fluids. *International Journal of Multiphase Flow*, 25(2), 307-320. <https://www.sciencedirect.com/science/article/pii/S0301932298000500>
- Bergantz, G. W., Schleicher, J. M., & Burgisser, A. (2015). Open-system dynamics and mixing in magma mushes. *Nature Geoscience*, 8(10), 793-+. <Go to ISI>://WOS:000363951200020
- Bergantz, G. W., Schleicher, J. M., & Burgisser, A. (2017). On the kinematics and dynamics of crystal-rich systems. *Journal of Geophysical Research-Solid Earth*, 122(8), 6131-6159. <Go to ISI>://WOS:000411340500017
- Berger, J., Lo, K., Diot, H., Triantafyllou, A., Plissart, G., & Femenias, O. (2017). Deformation-driven Differentiation during in situ Crystallization of the 2 center dot 7 Ga Iguilid Mafic Intrusion (West African Craton, Mauritania). *Journal of Petrology*, 58(4), 819-840. <Go to ISI>://WOS:000407428500007
- Bertolett, E. M., Prior, D. J., Grayley, D. M., Hampton, S. J., & Kennedy, B. M. (2019). Compacted cumulates revealed by electron backscatter diffraction analysis of plutonic lithics. *Geology*, 47(5), 445-448. <Go to ISI>://WOS:000465420900021
- Bouchez, J. L., Delas, C., Gleizes, G., Nedelec, A., & Cuney, M. (1992). Submagmatic Microfractures in Granites. *Geology*, 20(1), 35-38. <Go to ISI>://WOS:A1992GZ53700009
- Brown, M. (1994). The Generation, Segregation, Ascent and Emplacement of Granite Magma - the Migmatite-to-Crustally-Derived-Granite Connection in Thickened Orogens. *Earth-Science Reviews*, 36(1-2), 83-130. <Go to ISI>://WOS:A1994NK27800005
- Brown, M. (2007). Crustal melting and melt extraction, ascent and emplacement in orogens: mechanisms and consequences. *Journal of the Geological Society*, 164, 709-730. <Go to ISI>://WOS:000248627600002
- Brown, M. (2013). Granite: From genesis to emplacement. *Geological Society of America Bulletin*, 125(7-8), 1079-1113. <Go to ISI>://WOS:000323270800003
- Brown, M., & Solar, G. S. (1998). Granite ascent and emplacement during contractional deformation in convergent orogens. *Journal of Structural Geology*, 20(9-10), 1365-1393. <Go to ISI>://WOS:000077215900016
- Burg, J. P., & Vigneresse, J. L. (2002). Non-linear feedback loops in the rheology of cooling-crystallizing felsic magma and heating-melting felsic rock. *Geological Society, London, Special Publications*, 200(1), 275-292. <http://sp.lyellcollection.org/content/200/1/275.abstract>
- Burgisser, A., & Bergantz, G. W. (2002). Reconciling pyroclastic flow and surge: the multiphase physics of pyroclastic density currents. *Earth and Planetary Science Letters*, 202, 405-418.

- Burgisser, A., Bergantz, G. W., & Breidenthal, R. E. (2005). Addressing complexity in laboratory experiments: the scaling of dilute multiphase flows in magmatic systems. *Journal of Volcanology and Geothermal Research*, 141, 245-265.
- Cahyadi, A., Anantharaman, A., Yang, S., Karri, S. B. R., Findlay, J. G., Cocco, R. A., & Chew, J. W. (2017). Review of cluster characteristics in circulating fluidized bed (CFB) risers. *Chemical Engineering Science*, 158, 70-95.
<https://www.sciencedirect.com/science/article/pii/S0009250916305310>
- Calvert, A. J. (2011). The Seismic Structure of Island Arc Crust. In D. Brown & P. D. Ryan (Eds.), *Arc-Continent Collision* (pp. 87-119). Berlin, Heidelberg: Springer Berlin Heidelberg.
- Calvert, A. J., Klemperer, S. L., Takahashi, N., & Kerr, B. C. (2008). Three-dimensional crustal structure of the Mariana island arc from seismic tomography. *Journal of Geophysical Research-Solid Earth*, 113(B1). <Go to ISI>://WOS:000252754200001
- Camilletti, G. C., Otamendi, J. E., Tibaldi, A. M., Cristofolini, E., Leisen, M., Romero, R., et al. (2020). Geology, petrology and geochronology of sierra Valle Fertil - La Huerta batholith: Implications for the construction of a middle-crust magmatic-arc section. *Journal of South American Earth Sciences*, 97. <Go to ISI>://WOS:000509617600024
- Campbell, C. S. (2006). Granular material flows- An overview. *Powder Technology*, 162, 208-229.
- Carrara, A., Burgisser, A., & Bergantz, G. W. (2019). Lubrication effects on magmatic mush dynamics. *Journal of Volcanology and Geothermal Research*, 380, 19-30. <Go to ISI>://WOS:000474329500002
- Carrara, A., Burgisser, A., & Bergantz, G. W. (2020). The architecture of intrusions in magmatic mush. *Earth and Planetary Science Letters*, 549, 116539.
<https://www.sciencedirect.com/science/article/pii/S0012821X20304830>
- Cashman, K. V., Sparks, R. S., & Blundy, J. D. (2017). Vertically extensive and unstable magmatic systems: A unified view of igneous processes. *Science*, 355(6331), eaag3055.
<https://www.ncbi.nlm.nih.gov/pubmed/28336610>
- Castruccio, A., Rust, A. C., & Sparks, R. S. J. (2010). Rheology and flow of crystal-bearing lavas: Insights from analogue gravity currents. *Earth and Planetary Science Letters*, 297(3-4), 471-480.
<http://www.sciencedirect.com/science/article/pii/S0012821X10004383>
- Cates, M. E., Wittmer, J. P., Bouchaud, J. P., & Claudin, P. (1998). Jamming, Force Chains, and Fragile Matter. *Physical Review Letters*, 81(9), 1841-1844.
<https://link.aps.org/doi/10.1103/PhysRevLett.81.1841>
- Chen, Y.-M., Jang, C.-S., Cai, P., & Fan, L.-S. (1991). On the formation and disintegration of particle clusters in a liquid—solid transport bed. *Chemical Engineering Science*, 46(9), 2253-2268. <http://www.sciencedirect.com/science/article/pii/000925099185124G>
- Claeson, D. T., & Meurer, W. P. (2004). Fractional crystallization of hydrous basaltic ?arc-type? magmas and the formation of amphibole-bearing gabbroic cumulates. *Contributions to Mineralogy and Petrology*, 147(3), 288-304.
- Clark, P. J., & Evans, F. C. (1954). Distance to Nearest Neighbor as a Measure of Spatial Relationships in Populations. *Ecology*, 35(4), 445-453.
<https://esajournals.onlinelibrary.wiley.com/doi/abs/10.2307/1931034>
- Coetsee, M. S., Bate, M. D., & Elsenbroek, J. H. (1995). Flow differentiation - an explanation for the origin and distribution of plagioclase glomerocrysts in the Annas Rust dolerite sill,

- Vredefort Dome. *South African Journal of Geology*, 98(3), 276-286.
<https://journals.co.za/content/journal/10520/EJC-92a3c8267>
- Cooper, K. M. (2015). Timescales of crustal magma reservoir processes: insights from U-series crystal ages. *Geological Society, London, Special Publications*, 422(1), 141-174.
<http://sp.lyellcollection.org/content/422/1/141.abstract>
- Cooper, K. M., & Kent, A. J. (2014). Rapid remobilization of magmatic crystals kept in cold storage. *Nature*, 506(7489), 480-483. <https://www.ncbi.nlm.nih.gov/pubmed/24531766>
- Cristofolini, E. A., Otamendi, J. E., Walker, B. A., Tibaldi, A. M., Armas, P., Bergantz, G. W., & Martino, R. D. (2014). A Middle Paleozoic shear zone in the Sierra de Valle Fertil, Argentina: Records of a continent-arc collision in the Famatinian margin of Gondwana. *Journal of South American Earth Sciences*, 56, 170-185. <Go to ISI>://WOS:000346452500011
- Crowe, C. T., Chung, J. N., & Troutt, T. R. (1988). Particle mixing in free shear flows. *Prog. Engr. Combust. Sci.*, 14, 171.
- Crowe, C. T., Summerfield, M., & Tsuji, Y. (1998). *Multiphase Flows with Droplets and Particles*: CRC Press.
- Crowley, J. M. (2006). Viscosity-induced instability of a one-dimensional lattice of falling spheres. *Journal of Fluid Mechanics*, 45(1), 151-159.
<https://www.cambridge.org/core/article/viscosityinduced-instability-of-a-onedimensional-lattice-of-falling-spheres/FDCB3394876E93AC3F0FA9A03A7F0596>
- Cruz-Gandarilla, F., Bolmaro, R. E., Mendoza-Leon, H. F., Salcedo-Garrido, A. M., & Cabanas-Moreno, J. G. (2019). Study of recovery and first recrystallisation kinetics in CGO Fe3%Si steels using misorientation-derived parameters (EBSD). *J Microsc*, 275(3), 133-148. <https://www.ncbi.nlm.nih.gov/pubmed/31271444>
- Culha, C., Suckale, J., Keller, T., & Qin, Z. (2020). Crystal Fractionation by Crystal-Driven Convection. *Geophysical Research Letters*, 47(4), e2019GL086784.
<https://agupubs.onlinelibrary.wiley.com/doi/abs/10.1029/2019GL086784>
- Dantu, P. (1957). *Contribution à l'Étude Mécanique et Géométrique des Milieux Pulvérulents*. Paper presented at the Proc. Of the 4th International Conf. On Soil Mech. and Foundation Eng.
- Deen, N. G., Annaland, M. V., Van der Hoef, M. A., & Kuipers, J. A. M. (2007). Review of discrete particle modeling of fluidized beds. *Chemical Engineering Science*, 62(1-2), 28-44. Review. <Go to ISI>://WOS:000243095400003
- Delannay, R., Valance, A., Mangeney, A., Roche, O., & Richard, P. (2017). Granular and particle-laden flows: from laboratory experiments to field observations. *Journal of Physics D: Applied Physics*, 50(5), 053001. <http://dx.doi.org/10.1088/1361-6463/50/5/053001>
- Ducea, M. N., Bergantz, G. W., Crowley, J. L., & Otamendi, J. (2017). Ultrafast magmatic buildup and diversification to produce continental crust during subduction. *Geology*, 45(3), 235-238. <Go to ISI>://WOS:000396125100010
- Ducea, M. N., Saleeby, J. B., & Bergantz, G. W. (2015). The Architecture, Chemistry, and Evolution of Continental Magmatic Arcs. *Annual Review of Earth and Planetary Sciences*, Vol 43, 43(1), 299-331. <Go to ISI>://WOS:000355760100011
- Dufek, J., & Bergantz, G. W. (2007). Suspended load and bed-load transport of particle laden gravity currents: the role of particle-bed interaction. *Theoretical and Computational Fluid Dynamics*, 21(2), 119-145.

- Dufresne, A. (2012). Granular flow experiments on the interaction with stationary runout path materials and comparison to rock avalanche events. *Earth Surface Processes and Landforms*, 37(14), 1527-1541. <https://onlinelibrary.wiley.com/doi/abs/10.1002/esp.3296>
- El Yacoubi, A., Xu, S., & Wang, Z. J. (2012). Computational study of the interaction of freely moving particles at intermediate Reynolds numbers. *Journal of Fluid Mechanics*, 705, 134-148. <https://www.cambridge.org/core/article/computational-study-of-the-interaction-of-freely-moving-particles-at-intermediate-reynolds-numbers/2FDEAE92DDA524F4503038CA2EABE737>
- Ellis, B. S., Bachmann, O., & Wolff, J. A. (2014). Cumulate fragments in silicic ignimbrites: The case of the Snake River Plain. *Geology*, 42(5), 431-434. <http://dx.doi.org/10.1130/G35399.1>
- Ern, P., Risso, F., Fabre, D., & Magnaudet, J. (2012). Wake-Induced Oscillatory Paths of Bodies Freely Rising or Falling in Fluids. *Annual Review of Fluid Mechanics*, 44(1), 97-121. <https://www.annualreviews.org/doi/abs/10.1146/annurev-fluid-120710-101250>
- Estep, J., & Dufek, J. (2012). Substrate effects from force chain dynamics in dense granular flows. *Journal of Geophysical Research-Earth Surface*, 117(F1), n/a-n/a. <Go to ISI>://WOS:000301943800001
- Estep, J., & Dufek, J. (2013). Discrete element simulations of bed force anomalies due to force chains in dense granular flows. *Journal of Volcanology and Geothermal Research*, 254, 108-117. <Go to ISI>://WOS:000316920900009
- Etheridge, M. A., Daczko, N. R., Chapman, T., & Stuart, C. A. (2021). Mechanisms of melt extraction during lower crustal partial melting. *Journal of Metamorphic Geology*, 39(1), 57-75. <Go to ISI>://WOS:000560230500001
- Farin, M., Mangeney, A., & Roche, O. (2014). Fundamental changes of granular flow dynamics, deposition, and erosion processes at high slope angles: Insights from laboratory experiments. *Journal of Geophysical Research: Earth Surface*, 119(3), 504-532. <https://agupubs.onlinelibrary.wiley.com/doi/abs/10.1002/2013JF002750>
- Faroughi, S. A., & Huber, C. (2015). Unifying the relative hindered velocity in suspensions and emulsions of nondeformable particles. *Geophysical Research Letters*, 42(1), 53-59. <https://agupubs.onlinelibrary.wiley.com/doi/abs/10.1002/2014GL062570>
- Ferenc, J.-S., & Nédá, Z. (2007). On the size distribution of Poisson Voronoi cells. *Physica A: Statistical Mechanics and its Applications*, 385(2), 518-526. <http://www.sciencedirect.com/science/article/pii/S0378437107007546>
- Ferguson, M. R. M., Ehrig, K., Meffre, S., & Feig, S. (2019). From magma to mush to lava: Crystal history of voluminous felsic lavas in the Gawler Range Volcanics, South Australia. *Lithos*, 346-347, 105148. <http://www.sciencedirect.com/science/article/pii/S0024493719302993>
- Forien, M., Tremblay, J., Barnes, S.-J., Burgisser, A., & Pagé, P. (2015). The role of viscous particle segregation in forming chromite layers from slumped crystal slurries: Insights from analogue experiments. *Journal of Petrology*, 56(12), 2425-2444. <http://dx.doi.org/10.1093/petrology/egv060>
- Forien, M., Tremblay, J., Barnes, S. J., Burgisser, A., & Page, P. (2015). The Role of Viscous Particle Segregation in Forming Chromite Layers from Slumped Crystal Slurries: Insights from Analogue Experiments. *Journal of Petrology*, 56(12), 2425-2444. <Go to ISI>://WOS:000373646800007

- Forterre, Y., & Pouliquen, O. (2008). Flows of dense granular media. In *Annual Review of Fluid Mechanics* (Vol. 40, pp. 1-24). Palo Alto: Annual Reviews.
- Fortes, A. F., Joseph, D. D., & Lundgren, T. S. (2006). Nonlinear mechanics of fluidization of beds of spherical particles. *Journal of Fluid Mechanics*, 177, 467-483.
<https://www.cambridge.org/core/article/nonlinear-mechanics-of-fluidization-of-beds-of-spherical-particles/3AC50F237EEA886F3EC7DD24A80A6E6B>
- Franklin, S. V., & Shattuck, M. D. (Eds.). (2015). *Handbook of Granular Materials*. Amsterdam: CRC Press.
- Fu, X., Yao, Z., & Zhang, X. (2017). Numerical simulation of polygonal particles moving in incompressible viscous fluids. *Particuology*, 31, 140-151.
<http://www.sciencedirect.com/science/article/pii/S1674200116301274>
- Fullmer, W. D., & Hrenya, C. M. (2017). The Clustering Instability in Rapid Granular and Gas-Solid Flows. *Annual Review of Fluid Mechanics*, Vol 49, 49(1), 485-510. <Go to ISI>://WOS:000396042600020
- Garg, R., Galvin, J., Li, T., & Pannala, S. (2012a). Documentation of open-source MFIX-DEM software for gas-solids flows. https://mfix.netl.doe.gov/documentation/dem_doc_2012-1.pdf.
- Garg, R., Galvin, J., Li, T. W., & Pannala, S. (2012b). Open-source MFIX-DEM software for gas-solids flows: Part I-Verification studies. *Powder Technology*, 220, 122-137. <Go to ISI>://WOS:000302338900015
- Garibaldi, N., Tikoff, B., Schaen, A. J., & Singer, B. S. (2018). Interpreting Granitic Fabrics in Terms of Rhyolitic Melt Segregation, Accumulation, and Escape Via Tectonic Filter Pressing in the Huemul Pluton, Chile. *Journal of Geophysical Research: Solid Earth*, 123(10), 8548-8567.
<https://agupubs.onlinelibrary.wiley.com/doi/abs/10.1029/2018JB016282>
- Girolami, L., Hergault, V., Vinay, G., & Wachs, A. (2012). A three-dimensional discrete-grain model for the simulation of dam-break rectangular collapses: comparison between numerical results and experiments. *Granular Matter*, 14(3), 381-392. <Go to ISI>://WOS:000303881800007
- Guazzelli, E., & Hinch, J. (2011). Fluctuations and Instability in Sedimentation. *Annual Review of Fluid Mechanics*, 43(1), 97-116.
<https://www.annualreviews.org/doi/abs/10.1146/annurev-fluid-122109-160736>
- Guo, P. (2012). Critical length of force chains and shear band thickness in dense granular materials. *Acta Geotechnica*, 7, 41-55.
- Guo, Y., Wassgren, C., Hancock, B., Ketterhagen, W., & Curtis, J. (2013). Granular shear flows of flat disks and elongated rods without and with friction. *Physics of Fluids*, 25(6). <Go to ISI>://WOS:000321272600020
- Guo, Y., Wassgren, C., Ketterhagen, W., Hancock, B., James, B., & Curtis, J. (2012). A numerical study of granular shear flows of rod-like particles using the discrete element method. *Journal of Fluid Mechanics*, 713, 1-26. <Go to ISI>://WOS:000311889500001
- Hall, D., & Kisters, A. (2016). Episodic granite accumulation and extraction from the mid-crust. *Journal of Metamorphic Geology*, 34(5), 483-500. <Go to ISI>://WOS:000379933100005
- Hansen, S., Khakhar, D. V., & Ottino, J. M. (1998). Dispersion of solids in nonhomogeneous viscous flows. *Chemical Engineering Science*, 53(10), 1803-1817.
<https://www.sciencedirect.com/science/article/pii/S0009250998000104>

- Heidelbach, F., Post, A., & Tullis, J. (2000). Crystallographic preferred orientation in albite samples deformed experimentally by dislocation and solution precipitation creep. *Journal of Structural Geology*, 22(11-12), 1649-1661. <Go to ISI>://WOS:000165521400013
- Hielscher, R., & Schaeben, H. (2008). A novel pole figure inversion method: specification of the MTEX algorithm. *Journal of Applied Crystallography*, 41(6), 1024-1037.
- Hirsch, D. M., Ketcham, R. A., & Carlson, W. D. (2000). An evaluation of spatial correlation functions in textural analysis of metamorphic rocks. *Geological Materials Research*, 2(3), 1-42.
- Holness, M. B. (2018). Melt segregation from silicic crystal mushes: a critical appraisal of possible mechanisms and their microstructural record. *Contrib Mineral Petrol*, 173(6), 48. <https://www.ncbi.nlm.nih.gov/pubmed/30996392>
- Holness, M. B., Clemens, J. D., & Vernon, R. H. (2018). How deceptive are microstructures in granitic rocks? Answers from integrated physical theory, phase equilibrium, and direct observations. *Contrib Mineral Petrol*, 173(8), 62. <https://www.ncbi.nlm.nih.gov/pubmed/30956283>
- Holness, M. B., Stock, M. J., & Geist, D. (2019). Magma chambers versus mush zones: constraining the architecture of sub-volcanic plumbing systems from microstructural analysis of crystalline enclaves. *Philos Trans A Math Phys Eng Sci*, 377(2139), 20180006. <https://www.ncbi.nlm.nih.gov/pubmed/30966927>
- Holness, M. B., Vukmanovic, Z., & Mariani, E. (2017). Assessing the Role of Compaction in the Formation of Adcumulates: a Microstructural Perspective. *Journal of Petrology*, 58(4), 643-673. <Go to ISI>://WOS:000407428500001
- Hoomans, B. P. B., Kuipers, J. A. M., Briels, W. J., & van Swaaij, W. P. M. (1996). Discrete particle simulation of bubble and slug formation in a two-dimensional gas-fluidised bed: A hard-sphere approach. *Chemical Engineering Science*, 51(1), 99-118. <https://www.sciencedirect.com/science/article/pii/0009250995002715>
- Horio, M., & Clift, R. (1992). A note on terminology: 'Clusters' and 'agglomerates'. *Powder Technology*, 70(3), 196. <https://www.sciencedirect.com/science/article/pii/003259109280053Y>
- Hoyal, D., Bursik, M. I., & Atkinson, J. F. (1999). Settling-driven convection: A mechanism of sedimentation from stratified fluids. *Journal of Geophysical Research*, 104(C4), 7953-7966.
- Huisman, S. G., Barois, T., Bourgoin, M., Chouippe, A., Doychev, T., Huck, P., et al. (2016). Columnar structure formation of a dilute suspension of settling spherical particles in a quiescent fluid. *Physical Review Fluids*, 1(7), 074204. <https://link.aps.org/doi/10.1103/PhysRevFluids.1.074204>
- Hurley, R. C., Hall, S. A., Andrade, J. E., & Wright, J. (2016). Quantifying Interparticle Forces and Heterogeneity in 3D Granular Materials. *Physical Review Letters*, 117(9), 098005. <https://link.aps.org/doi/10.1103/PhysRevLett.117.098005>
- Iverson, R. M. (1997). The physics of debris flows. *Reviews of Geophysics*, 35(3), 245-296. <Go to ISI>://WOS:A1997XN90100002
- Jagoutz, O., & Klein, B. (2018). On the importance of crystallization-differentiation for the generation of SiO₂-rich melts and the compositional build-up of arc (and continental) crust. *American Journal of Science*, 318(1), 29-63. <http://www.ajsonline.org/content/318/1/29.abstract>

- Jayaweera, K. O. L. F., Mason, B. J., & Slack, G. W. (1964). The behaviour of clusters of spheres falling in a viscous fluid Part 1. Experiment. *Journal of Fluid Mechanics*, 20(1), 121-128. <https://www.cambridge.org/core/article/behaviour-of-clusters-of-spheres-falling-in-a-viscous-fluid-part-1-experiment/D34813BB8574D33F65AEA59E78BC39BB>
- Jellinek, A. M., & Kerr, R. C. (2001). Magma dynamics, crystallization, and chemical differentiation of the 1959 Kilauea Iki lava lake, Hawaii, revisited. *Journal of Volcanology and Geothermal Research*, 110, 235-263.
- Jenny, M., Dušek, J., & Bouchet, G. (2004). Instabilities and transition of a sphere falling or ascending freely in a Newtonian fluid. *Journal of Fluid Mechanics*, 508, 201-239. <https://www.cambridge.org/core/article/instabilities-and-transition-of-a-sphere-falling-or-ascending-freely-in-a-newtonian-fluid/68B3173FDB05D467F590C1A98DF6221E>
- Jerram, D. A. (2003). Quantifying the Building Blocks of Igneous Rocks: Are Clustered Crystal Frameworks the Foundation? *Journal of Petrology*, 44(11), 2033-2051.
- Jerram, D. A., & Cheadle, M. J. (2000). On the cluster analysis of grains and crystals in rocks. *American Mineralogist*, 85(1), 47-67. <http://dx.doi.org/10.2138/am-2000-0107>
- Jerram, D. A., Cheadle, M. J., Hunter, R. H., & Elliott, M. T. (1996). The spatial distribution of grains and crystals in rocks. *Contributions to Mineralogy and Petrology*, 125(1), 60-74. journal article. <https://doi.org/10.1007/s004100050206>
- Jerram, D. A., Cheadle, M. J., & Philpotts, A. R. (2003). Quantifying the building blocks of igneous rocks: Are clustered crystal frameworks the foundation? *Journal of Petrology*, 44, 2033-2051.
- Joseph, D. D., Liu, Y. J., Poletto, M., & Feng, J. (1994). Aggregation and dispersion of spheres falling in viscoelastic liquids. *Journal of Non-Newtonian Fluid Mechanics*, 54, 45-86. <https://www.sciencedirect.com/science/article/pii/0377025794800154>
- Kajishima, T. (2004). Influence of particle rotation on the interaction between particle clusters and particle-induced turbulence. *International Journal of Heat and Fluid Flow*, 25(5), 721-728. <https://www.sciencedirect.com/science/article/pii/S0142727X04000815>
- Kawabata, H., Nishiura, D., Sakaguchi, H., & Tatsumi, Y. (2013). Self-organized domain microstructures in a plate-like particle suspension subjected to rapid simple shear. *Rheologica Acta*, 52(1), 1-21. <https://doi.org/10.1007/s00397-012-0657-3>
- Klemetti, E. W. (2016). Melts, mush, and more: Evidence for the state of intermediate-to-silicic arc magmatic systems. *American Mineralogist*, 101(11), 2365-2366.
- Kriegsman, L. M. (2001). Partial melting, partial melt extraction and partial back reaction in anatectic migmatites. *Lithos*, 56(1), 75-96. <Go to ISI>://WOS:000166973400006
- Kruyt, N. P. (2016). On weak and strong contact force networks in granular materials. *International Journal of Solids and Structures*, 92-93, 135-140. <https://www.sciencedirect.com/science/article/pii/S0020768316001074>
- Lavorel, G., & Le Bars, M. (2009). Sedimentation of particles in a vigorously convecting fluid. *Physical Review E*, 80(4), 046324. <https://link.aps.org/doi/10.1103/PhysRevE.80.046324>
- Li, J., & Kuipers, J. A. M. (2007). Effect of competition between particle–particle and gas–particle interactions on flow patterns in dense gas-fluidized beds. *Chemical Engineering Science*, 62(13), 3429-3442. <https://www.sciencedirect.com/science/article/pii/S0009250907002667>

- Li, T., & Guenther, C. (2012). MFIx-DEM simulations of change of volumetric flow in fluidized beds due to chemical reactions. *Powder Technology*, 220(0), 70-78. <http://www.sciencedirect.com/science/article/pii/S0032591011005080>
- Li, T. W., Garg, R., Galvin, J., & Pannala, S. (2012). Open-source MFIx-DEM software for gas-solids flows: Part II - Validation studies. *Powder Technology*, 220, 138-150. <Go to ISI>://WOS:000302338900016
- Lissenberg, C. J., MacLeod, C. J., & Bennett, E. N. (2019). Consequences of a crystal mush-dominated magma plumbing system: a mid-ocean ridge perspective. *Philos Trans A Math Phys Eng Sci*, 377(2139), 20180014. <https://www.ncbi.nlm.nih.gov/pubmed/30966931>
- Lowenstern, J. B. (1994). Dissolved Volatile Concentrations in an Ore-Forming Magma. *Geology*, 22(10), 893-896. <Go to ISI>://WOS:A1994PJ58100007
- Lowenstern, J. B. (2001). Carbon dioxide in magmas and implications for hydrothermal systems. *Mineralium Deposita*, 36(6), 490-502. <Go to ISI>://WOS:000171251800002
- Majmudar, T. S., & Behringer, R. P. (2005). Contact force measurements and stress-induced anisotropy in granular materials. *Nature*, 435(7045), 1079-1082. <https://www.ncbi.nlm.nih.gov/pubmed/15973358>
- Marsh, B. D. (1981). On the Crystallinity, Probability of Occurrence, and Rheology of Lava and Magma. *Contributions to Mineralogy and Petrology*, 78(1), 85-98. <Go to ISI>://WOS:A1981MN06300009
- Marsh, B. D. (1988). Crystal capture, sorting, and retention in convecting magma. *GSA Bulletin*, 100(11), 1720-1737. [https://doi.org/10.1130/0016-7606\(1988\)100<1720:CCSARI>2.3.CO;2](https://doi.org/10.1130/0016-7606(1988)100<1720:CCSARI>2.3.CO;2)
- Marsh, B. D., & Maxey, M. R. (1985). On the distribution and separation of crystals in convecting magma. *Journal of Volcanology and Geothermal Research*, 24(1), 95-150. <https://www.sciencedirect.com/science/article/pii/0377027385900307>
- Martin, D., & Nokes, R. (1988). Crystal settling in a vigorously convecting magma chamber. *Nature*, 332, 534-536.
- Martin, J. E., & Meiburg, E. (1994). The accumulation and dispersion of heavy particles in forced two-dimensional mixing layers. I. The fundamental and subharmonic cases. *Physics of Fluids*, 6(3), 1116-1132. <https://aip.scitation.org/doi/abs/10.1063/1.868283>
- Martini, A., Bitencourt, M. D., Weinberg, R. F., & De Toni, G. B. (2019). Melt-collecting structures and the formation of extraction dykes during syntectonic anatexis of the Camboriu Complex, south Brazil. *Journal of Structural Geology*, 127. <Go to ISI>://WOS:000488676300006
- Mckenzie, D. (1984). The Generation and Compaction of Partially Molten Rock. *Journal of Petrology*, 25(3), 713-765. <Go to ISI>://WOS:A1984TJ46600006
- McKenzie, D. (2011). Compaction and Crystallization in Magma Chambers: Towards a Model of the Skaergaard Intrusion. *Journal of Petrology*, 52(5), 905-930. <Go to ISI>://WOS:000289840500004
- Michaelides, E., Crowe, C. T., & Schwarzkopf, J. D. (2017). *Multiphase flow handbook* (2'd ed.). Boca Raton: CRC Press.
- Monchaux, R., Bourgoin, M., & Cartellier, A. (2012). Analyzing preferential concentration and clustering of inertial particles in turbulence. *International Journal of Multiphase Flow*, 40, 1-18. <http://www.sciencedirect.com/science/article/pii/S030193221100245X>

- Moore, G. (2008). Interpreting H₂O and CO₂ Contents in Melt Inclusions: Constraints from Solubility Experiments and Modeling. *Minerals, Inclusions and Volcanic Processes*, 69(1), 333-361. <Go to ISI>://WOS:000263064200010
- Morse, S. A. (1976). The lever rule with fractional crystallization and fusion. *American Journal of Science*, 276, 330-346.
- Müntener, O., & Ulmer, P. (2018). Arc crust formation and differentiation constrained by experimental petrology. *American Journal of Science*, 318(1), 64-89. <http://www.ajsonline.org/content/318/1/64.abstract>
- Mutabaruka, P., Delenne, J. Y., Soga, K., & Radjai, F. (2014). Initiation of immersed granular avalanches. *Phys Rev E Stat Nonlin Soft Matter Phys*, 89(5), 052203. <https://www.ncbi.nlm.nih.gov/pubmed/25353783>
- Muthuswamy, M., & Tordesillas, A. (2006). How do interparticle contact friction, packing density and degree of polydispersity affect force propagation in particulate assemblies? *Journal of Statistical Mechanics: Theory and Experiment*, 2006(09), P09003. <http://stacks.iop.org/1742-5468/2006/i=09/a=P09003>
- Neave, D. A., Passmore, E., MacLennan, J., Fitton, G., & Thordarson, T. (2013). Crystal-Melt Relationships and the Record of Deep Mixing and Crystallization in the ad 1783 Laki Eruption, Iceland. *Journal of Petrology*, 54(8), 1661-1690. <Go to ISI>://WOS:000322403300009
- Nicolas, A. (1992). Kinematics in Magmatic Rocks with Special Reference to Gabbros. *Journal of Petrology*, 33(4), 891-915. <Go to ISI>://WOS:A1992JJ92800007
- Nie, D., Lin, J., & Zheng, M. (2015). Direct numerical simulation of multiple particles sedimentation at an intermediate Reynolds number. *Communications in Computational Physics*, 16(3), 675-698. <https://www.cambridge.org/core/article/direct-numerical-simulation-of-multiple-particles-sedimentation-at-an-intermediate-reynolds-number/AACEA63340509B704626151BE8DBAF74>
- Otamendi, J. E., Cristofolini, E. A., Morosini, A., Armas, P., Tibaldi, A. M., & Camilletti, G. C. (2020). The geodynamic history of the Famatinian arc, Argentina: A record of exposed geology over the type section (latitudes 27 degrees-33 degrees south). *Journal of South American Earth Sciences*, 100. <Go to ISI>://WOS:000532794900022
- Otamendi, J. E., Cristofolini, E. A., Tibaldi, A. M., Quevedo, F. I., & Baliani, I. (2010). Petrology of mafic and ultramafic layered rocks from the Jaboncillo Valley, Sierra de Valle Fertil, Argentina: Implications for the evolution of magmas in the lower crust of the Famatinian arc. *Journal of South American Earth Sciences*, 29(3), 685-704. <Go to ISI>://WOS:000278417300012
- Otamendi, J. E., Ducea, M. N., Tibaldi, A. M., Bergantz, G. W., de la Rosa, J. D., & Vujovich, G. I. (2009). Generation of Tonalitic and Dioritic Magmas by Coupled Partial Melting of Gabbroic and Metasedimentary Rocks within the Deep Crust of the Famatinian Magmatic Arc, Argentina. *Journal of Petrology*, 50(5), 841-873. <Go to ISI>://WOS:000266967000003
- Otamendi, J. E., Vujovich, G. I., de la Rosa, J. D., Tibaldi, A. M., Castro, A., Martino, R. D., & Pinotti, L. P. (2009). Geology and petrology of a deep crustal zone from the Famatinian paleo-arc, Sierras de Valle Fertil and La Huerta, San Juan, Argentina. *Journal of South American Earth Sciences*, 27(4), 258-279. <Go to ISI>://WOS:000266672900003

- Paiement-Paradis, G., Buffin-Bélanger, T., & Roy, A. G. (2003). Scalings for large turbulent flow structures in gravel-bed rivers. *Geophysical Research Letters*, 30(14). <https://agupubs.onlinelibrary.wiley.com/doi/abs/10.1029/2003GL017553>
- Pailha, M., Nicolas, M., & Pouliquen, O. (2008). Initiation of underwater granular avalanches: Influence of the initial volume fraction. *Physics of Fluids (1994-present)*, 20(11), 111701. <http://scitation.aip.org/content/aip/journal/pof2/20/11/10.1063/1.3013896>
- Parthasarathy, R. N., & Faeth, G. M. (2006). Turbulent dispersion of particles in self-generated homogeneous turbulence. *Journal of Fluid Mechanics*, 220, 515-537. <https://www.cambridge.org/core/article/turbulent-dispersion-of-particles-in-selfgenerated-homogeneous-turbulence/7C6DCE48EE12CC877DBDA5EBB287328A>
- Passmore, E., Maclennan, J., Fitton, G., & Thordarson, T. (2012). Mush Disaggregation in Basaltic Magma Chambers: Evidence from the ad 1783 Laki Eruption. *Journal of Petrology*, 53(12), 2593-2623. <Go to ISI>://WOS:000311670500007
- Paterson, S. R., Ardill, K., Vernon, R., & Zak, J. (2019). A review of mesoscopic magmatic structures and their potential for evaluating the hypersolidus evolution of intrusive complexes. *Journal of Structural Geology*, 125, 134-147. <Go to ISI>://WOS:000474501600014
- Paterson, S. R., Zak, J., & Janousek, V. (2008). Growth of complex sheeted zones during recycling of older magmatic units into younger: Sawmill Canyon area, Tuolumne batholith, Sierra Nevada, California. *Journal of Volcanology and Geothermal Research*, 177(2), 457-484. <Go to ISI>://WOS:000261120000012
- Peters, J. F., Muthuswamy, M., Wibowo, J., & Tordesillas, A. (2005). Characterization of force chains in granular material. *Physical Review E*, 72(4), 041307. <http://link.aps.org/doi/10.1103/PhysRevE.72.041307>
- Petford, N. (2009). Which effective viscosity? *Mineralogical magazine*, 73(2), 167-191.
- Petford, N., & Koenders, M. A. (1998). Granular flow and viscous fluctuations in low Bagnold number granitic magmas. *Journal of the Geological Society*, 155(5), 873-881. <https://jgs.lyellcollection.org/content/jgs/155/5/873.full.pdf>
- Petford, N., Koenders, M. A., & Clemens, J. D. (2020). Igneous differentiation by deformation. *Contributions to Mineralogy and Petrology*, 175(5). <Go to ISI>://WOS:000530139900002
- Philpotts, A. R., Shi, J., & Brustman, C. (1998). Role of plagioclase crystal chains in the differentiation of partly crystallized basaltic magma. *Nature*, 395(6700), 343-346. <https://doi.org/10.1038/26404>
- Picard, D., Arbaret, L., Pichavant, M., Champallier, R., & Launeau, P. (2013). The rheological transition in plagioclase-bearing magmas. *Journal of Geophysical Research: Solid Earth*, 118(4), 1363-1377. <https://agupubs.onlinelibrary.wiley.com/doi/abs/10.1002/jgrb.50091>
- Pistone, M., Arzilli, F., Dobson, K. J., Cordonnier, B., Reusser, E., Ulmer, P., et al. (2015). Gas-driven filter pressing in magmas: Insights into in-situ melt segregation from crystal mushes. *Geology*, 43(8), 699-702. <Go to ISI>://WOS:000359014600011
- Qin, Z., & Suckale, J. (2020). Flow-to-Sliding Transition in Crystal-Bearing Magma. *Journal of Geophysical Research: Solid Earth*, 125(2), e2019JB018549. <https://agupubs.onlinelibrary.wiley.com/doi/abs/10.1029/2019JB018549>
- Raju, N., & Meiburg, E. (1995). The accumulation and dispersion of heavy particles in forced two-dimensional mixing layers. Part 2. The effect of gravity. *Physics Fluids*, 7, 1241-1264.

- Reddy, S. M., & Buchan, C. (2005). Constraining kinematic rotation axes in high-strain zones: a potential microstructural method? *Geological Society, London, Special Publication*, 24.(1), 1-10.
- Reynolds, O. (1885). LVII. On the dilatancy of media composed of rigid particles in contact. With experimental illustrations. *The London, Edinburgh, and Dublin Philosophical Magazine and Journal of Science*, 20(127), 469-481.
<https://doi.org/10.1080/14786448508627791>
- Ripley, B. D. (1976). The second-order analysis of stationary point processes. *Journal of Applied Probability*, 13(2), 255-266. <https://www.cambridge.org/core/article/secondorder-analysis-of-stationary-point-processes/63ECBD08B25F19C844C8FEC5B88C5266>
- Ripley, B. D. (1977). Modelling spatial patterns. *Journal of the Royal Statistical Society. Series B (Methodological)*, 39(2), 172-212. <http://www.jstor.org/stable/2984796>
- Roelofse, F., & Ashwal, L. D. (2012). The Lower Main Zone in the Northern Limb of the Bushveld Complex—a >1·3 km Thick Sequence of Intruded and Variably Contaminated Crystal Mushes. *Journal of Petrology*, 53(7), 1449-1476.
<https://doi.org/10.1093/petrology/egs022>
- Roggensack, K., Hervig, R. L., McKnight, S. B., & Williams, S. N. (1997). Explosive basaltic volcanism from Cerro Negro volcano: Influence of volatiles on eruptive style. *Science*, 277(5332), 1639-1642. <Go to ISI>://WOS:A1997XV68400043
- Rothenburg, L., & Bathurst, R. J. (1989). ANALYTICAL STUDY OF INDUCED ANISOTROPY IN IDEALIZED GRANULAR-MATERIALS. *Géotechnique*, 39(4), 601-614.
- Rudge, J. F., Holness, M. n. B., & Smith, G. C. (2008). Quantitative textural analysis of packings of elongate crystals. *Contributions to Mineralogy and Petrology*, 156(4), 413-429. journal article. <http://dx.doi.org/10.1007/s00410-008-0293-1>
- Rudnick, R. L. (1995). Making Continental-Crust. *Nature*, 378(6557), 571-578. <Go to ISI>://WOS:A1995TJ22100065
- Rudnick, R. L., & Gao, S. (2014). Composition of the Continental Crust. In *Treatise on Geochemistry* (pp. 1-51).
- Ruprecht, P., Bergantz, G. W., & Dufek, J. (2008). Modeling of Gas-Driven Magmatic Overturn: Tracking of Phenocryst Dispersal and Gathering During Magma Mixing. *Geophys. Geosyst.*, 9(7), Q07017.
- Sanders, I. S. (1986). Gas Filter-Pressing Origin for Segregation Vesicles in Dykes. *Geological Magazine*, 123(1), 67-72. <Go to ISI>://WOS:A1986A235400006
- Satsukawa, T., Ildfonse, B., Mainprice, D., Morales, L. F. G., Michibayashi, K., & Barou, F. (2013). A database of plagioclase crystal preferred orientations (CPO) and microstructures - implications for CPO origin, strength, symmetry and seismic anisotropy in gabbroic rocks. *Solid Earth*, 4(2), 511-542. <Go to ISI>://WOS:000330830100001
- Sawyer, E. W. (1994). Melt Segregation in the Continental-Crust. *Geology*, 22(11), 1019-1022. <Go to ISI>://WOS:A1994PP79000015
- Sawyer, E. W. (1996). Melt segregation and magma flow in migmatites: Implications for the generation of granite magmas. *Transactions Of The Royal Society Of Edinburgh-Earth Sciences*, 87(1-2), 85-94. <Go to ISI>://WOS:A1996VH75900010
- Sawyer, E. W. (1998). Formation and evolution of granite magmas during crustal reworking: the significance of diatexites. *Journal of Petrology*, 39(6), 1147-1167. <Go to ISI>://WOS:000074276000003

- Sawyer, E. W. (2014). The inception and growth of leucosomes: microstructure at the start of melt segregation in migmatites. *Journal of Metamorphic Geology*, 32(7), 695-712. <https://doi.org/10.1111/jmg.12088>. <Go to ISI>://WOS:000340475300002
- Schaen, A. J., Singer, B. S., Cottle, J. M., Garibaldi, N., Schoene, B., Satkoski, A. M., & Fournelle, J. (2018). Textural and Mineralogical Record of Low-pressure Melt Extraction and Silicic Cumulate Formation in the Late Miocene Risco Bayo-Huemul Plutonic Complex, Southern Andes. *Journal of Petrology*, 59(10), 1991-2016. <Go to ISI>://WOS:000452560300006
- Schleicher, J. M., & Bergantz, G. W. (2017). The Mechanics and Temporal Evolution of an Open-system Magmatic Intrusion into a Crystal-rich Magma. *Journal of Petrology*, 58(6), 1059-1072. <Go to ISI>://WOS:000412822200002
- Schleicher, J. M., Bergantz, G. W., Breidenthal, R. E., & Burgisser, A. (2016). Time scales of crystal mixing in magma mushes. *Geophysical Research Letters*, 43(4), 1543-1550. <Go to ISI>://WOS:000373109000019
- Schwindinger, K. R. (1999). Particle dynamics and aggregation of crystals in a magma chamber with application to Kilauea Iki olivines. *Journal of Volcanology and Geothermal Research*, 88(4), 209-238. <https://www.sciencedirect.com/science/article/pii/S0377027399000098>
- Schwindinger, K. R., & Anderson, A. T. (1989). Synneusis of Kilauea Iki olivines. *Contributions to Mineralogy and Petrology*, 103(2), 187-198. <https://doi.org/10.1007/BF00378504>
- Seaman, S. J. (2000). Crystal clusters, feldspar glomerocrysts, and magma envelopes in the Atascosa Lookout lava flow, southern Arizona, USA: Recorders of magmatic events. *Journal of Petrology*, 41(5), 693-716. <Go to ISI>://WOS:000086721800005
- Shirley, D. N. (1986). Compaction of Igneous Cumulates. *Journal of Geology*, 94(6), 795-809. <Go to ISI>://WOS:A1986E778800002
- Sisson, T. W., & Bacon, C. R. (1999). Gas-driven filter pressing in magmas. *Geology*, 27(7), 613-616. <Go to ISI>://WOS:000081167900009
- Sliwinski, J. T., Bachmann, O., Ellis, B. S., Davila-Harris, P., & Dufek, J. (2015). Eruption of Shallow Crystal Cumulates during Explosive Phonolitic Eruptions on Tenerife, Canary Islands. *Journal of Petrology*, 56(11), 2173-2194. <Go to ISI>://WOS:000368432300004
- Stunitz, H. (1998). Syndeformational recrystallization - dynamic or compositionally induced? *Contributions to Mineralogy and Petrology*, 131(2-3), 219-236. <Go to ISI>://WOS:000073805400009
- Suckale, J., Sethian, J. A., Yu, J.-d., & Elkins-Tanton, L. T. (2012). Crystals stirred up: 1. Direct numerical simulations of crystal settling in nondilute magmatic suspensions. *Journal of Geophysical Research: Planets*, 117(E8), E08004. <http://dx.doi.org/10.1029/2012JE004066>
- Svahnberg, H., & Piazzolo, S. (2012). Interaction of chemical and physical processes during deformation at fluid-present conditions: a case study from an anorthosite–leucogabbro deformed at amphibolite facies conditions. *Contributions to Mineralogy and Petrology*, 165(3), 543-562.
- Taira, A., Saito, S., Aoike, K., Morita, S., Tokuyama, H., Suyehiro, K., et al. (1998). Nature and growth rate of the northern Izu-Bonin (Ogasawara) arc crust and their implications for continental crust formation. *Island Arc*, 7(3), 395-407. <Go to ISI>://WOS:000076058200009

- Tanaka, T., Noma, K., Ide, Y., & Tsuji, Y. a. (2002). *Particle clusters formed in dispersed gas–solid flows: Simulation and experiment*. Paper presented at the Proc. of World Congress on Particle Technology, Sydney, Australia.
- Tang, L., Wen, F., Yang, Y., Crowe, C. T., Chung, J. N., & Troutt, T. R. (1992). Self-organizing particle dispersion mechanism in free shear flows. *Phys. Fluids, A* 4, 2244-2249.
- Tapster, S., Condon, D. J., Naden, J., Noble, S. R., Petterson, M. G., Roberts, N. M. W., et al. (2016). Rapid thermal rejuvenation of high-crystallinity magma linked to porphyry copper deposit formation; evidence from the Koloula Porphyry Prospect, Solomon Islands. *Earth and Planetary Science Letters*, 442, 206-217. <Go to ISI>://WOS:000375348700020
- Taylor, S. R. (1967). The Origin and growth of continents. *Tectonophysics*, 4(1), 17-34.
- Thøgersen, K., Dabrowski, M., & Malthe-Sørensen, A. (2016). Transient cluster formation in sheared non-Brownian suspensions. *Physical Review E*, 93(2), 022611. <https://link.aps.org/doi/10.1103/PhysRevE.93.022611>
- Tibaldi, A. M., Otarnendi, J. E., Cristofolini, E. A., Baliani, I., Walker, B. A., & Bergantz, G. W. (2013). Reconstruction of the Early Ordovician Famatinian arc through thermobarometry in lower and middle crustal exposures, Sierra de Valle Fertil, Argentina. *Tectonophysics*, 589, 151-166. <Go to ISI>://WOS:000317878000012
- Topin, V., Monerie, Y., Perales, F., & Radjaï, F. (2012). Collapse Dynamics and Runout of Dense Granular Materials in a Fluid. *Physical Review Letters*, 109(18), 188001. <https://link.aps.org/doi/10.1103/PhysRevLett.109.188001>
- Troch, J., Ellis, B. S., Mark, D. F., Bindeman, I. N., Kent, A. J. R., Guillong, M., & Bachmann, O. (2017). Rhyolite Generation prior to a Yellowstone Supereruption: Insights from the Island Park–Mount Jackson Rhyolite Series. *Journal of Petrology*, 58(1), 29-52. <https://doi.org/10.1093/petrology/egw071>
- Tsuji, T., Ito, A., & Tanaka, T. (2008). Multi-scale structure of clustering particles. *Powder Technology*, 179(3), 115-125. <Go to ISI>://WOS:000251925200003
- Tsukada, M., Ito, M., Kamiya, H., & Horio, M. (1997). Three-Dimension imaging of particle clusters in dilute gas—solid suspension flow. *The Canadian Journal of Chemical Engineering*, 75(2), 466-470. <https://onlinelibrary.wiley.com/doi/abs/10.1002/cjce.5450750222>
- Uhlmann, M., & Doychev, T. (2014). Sedimentation of a dilute suspension of rigid spheres at intermediate Galileo numbers: the effect of clustering upon the particle motion. *Journal of Fluid Mechanics*, 752, 310-348. <Go to ISI>://WOS:000339273300019
- Utter, B., & Behringer, R. P. (2004). Transients in sheared granular matter. *Eur Phys J E Soft Matter*, 14(4), 373-380. <https://www.ncbi.nlm.nih.gov/pubmed/15338433>
- Vance, J. A. (1969). On synneusis. *Contributions to Mineralogy and Petrology*, 24(1), 7-29. <https://doi.org/10.1007/BF00398750>
- VanTongeren, J. A., Hirth, G., & Kelemen, P. B. (2015). Constraints on the accretion of the gabbroic lower oceanic crust from plagioclase lattice preferred orientation in the Samail ophiolite. *Earth and Planetary Science Letters*, 427, 249-261. <Go to ISI>://WOS:000359330800025
- Verhoeven, J., & Schmalzl, J. (2009). A numerical method for investigating crystal settling in convecting magma chambers. *Geochemistry, Geophysics, Geosystems*, 10(12). <https://agupubs.onlinelibrary.wiley.com/doi/abs/10.1029/2009GC002509>

- Vigneresse, J. L., Barbey, P., & Cuney, M. (1996). Rheological transitions during partial melting and crystallization with application to felsic magma segregation and transfer. *Journal of Petrology*, 37(6), 1579-1600. <Go to ISI>://WOS:A1996WB04400014
- Vigneresse, J. L., & Tikoff, B. (1999). Strain partitioning during partial melting and crystallizing felsic magmas. *Tectonophysics*, 312(2-4), 117-132. <Go to ISI>://WOS:000084396600002
- Vogt, J. H. L. (1923). The Physical Chemistry of the Crystallization and Magmatic Differentiation of Igneous Rocks. *The Journal of Geology*, 31(5), 407-419. <https://www.journals.uchicago.edu/doi/abs/10.1086/623032>
- Vukmanovic, Z., Holness, M. B., Monks, K., & Andersen, J. C. O. (2018). The Skaergaard trough layering: sedimentation in a convecting magma chamber. *Contrib Mineral Petrol*, 173(5), 43. <https://www.ncbi.nlm.nih.gov/pubmed/31258174>
- Vukmanovic, Z., Holness, M. B., Stock, M. J., & Roberts, R. J. (2019). The Creation and Evolution of Crystal Mush in the Upper Zone of the Rustenburg Layered Suite, Bushveld Complex, South Africa. *Journal of Petrology*, 60(8), 1523-1541. <Go to ISI>://WOS:000509550500002
- Wager, L. R., Brown, G. M., & Wadsworth, W. J. (1960). Types of Igneous Cumulates. *Journal of Petrology*, 1(1), 73-85. <Go to ISI>://WOS:A1960WT81500004
- Walker, B. A., Bergantz, G. W., Otamendi, J. E., Ducea, M. N., & Cristofolini, E. A. (2015). A MASH Zone Revealed: the Mafic Complex of the Sierra Valle Fertil. *Journal of Petrology*, 56(9), 1863-1896. <Go to ISI>://WOS:000365416600007
- Wallace, P. J. (2005). Volatiles in subduction zone magmas: concentrations and fluxes based on melt inclusion and volcanic gas data. *Journal of Volcanology and Geothermal Research*, 140(1-3), 217-240. <Go to ISI>://WOS:000226429900012
- Wambaugh, J. F. (2010). Simple models for granular force networks. *Physica D: Nonlinear Phenomena*, 239(18), 1818-1826. <http://www.sciencedirect.com/science/article/pii/S0167278910001715>
- Wang, L., Guo, Z. L., & Mi, J. C. (2014). Drafting, kissing and tumbling process of two particles with different sizes. *Computers & Fluids*, 96, 20-34. <https://www.sciencedirect.com/science/article/pii/S0045793014001042>
- Wang, L., Marchisio, D. L., Vigil, R. D., & Fox, R. O. (2005). CFD simulation of aggregation and breakage processes in laminar Taylor–Couette flow. *Journal of Colloid and Interface Science*, 282(2), 380-396. <https://www.sciencedirect.com/science/article/pii/S0021979704008409>
- Ward, K. M., Zandt, G., Beck, S. L., Christensen, D. H., & McFarlin, H. (2014). Seismic imaging of the magmatic underpinnings beneath the Altiplano-Puna volcanic complex from the joint inversion of surface wave dispersion and receiver functions. *Earth and Planetary Science Letters*, 404, 43-53. <Go to ISI>://WOS:000343352100005
- Webber, J. R., Klepeis, K. A., Webb, L. E., Cembrano, J., Morata, D., Mora-Klepeis, G., & Arancibia, G. (2015). Deformation and magma transport in a crystallizing plutonic complex, Coastal Batholith, central Chile. *Geosphere*, 11(5), 1401-1426. <Go to ISI>://WOS:000365042300009
- Weinberg, R. F., & Mark, G. (2008). Magma migration, folding, and disaggregation of migmatites in the Karakoram Shear Zone, Ladakh, NW India. *Geological Society of America Bulletin*, 120(7-8), 994-1009. <Go to ISI>://WOS:000257423200012

- Weinstein, S. A., Yuen, D. A., & Olson, P. L. (1988). Evolution of crystal-settling in magma-chamber convection. *Earth and Planetary Science Letters*, 87(1), 237-248.
<https://www.sciencedirect.com/science/article/pii/0012821X88900787>
- Wiebe, R. A., Jellinek, A. M., & Hodge, K. F. (2017). New insights into the origin of ladder dikes: Implications for punctuated growth and crystal accumulation in the Cathedral Peak granodiorite. *Lithos*, 277(Supplement C), 241-258.
<http://www.sciencedirect.com/science/article/pii/S0024493716303036>
- Wilhelm, R. H. (1948). Fluidization of Solid Particles. *Chem. Eng. Prog.*, 44, 201-218.
<https://ci.nii.ac.jp/naid/10003393837/en/>
- Wolff, J. A., Forni, F., Ellis, B. S., & Szymanowski, D. (2020). Europium and barium enrichments in compositionally zoned felsic tuffs: A smoking gun for the origin of chemical and physical gradients by cumulate melting. *Earth and Planetary Science Letters*, 540, 116251.
<https://www.sciencedirect.com/science/article/pii/S0012821X20301941>
- Wright, S. I., Nowell, M. M., & Field, D. P. (2011). A review of strain analysis using electron backscatter diffraction. *Microsc Microanal*, 17(3), 316-329.
<https://www.ncbi.nlm.nih.gov/pubmed/21418731>
- Wu, J., & Manasseh, R. (1998). Dynamics of dual-particles settling under gravity. *International Journal of Multiphase Flow*, 24(8), 1343-1358.
<https://www.sciencedirect.com/science/article/pii/S0301932298000299>
- Wylie, J. J., & Koch, D. L. (2000). Particle clustering due to hydrodynamic interactions. *Physics of Fluids*, 12(5), 964-970. <https://aip.scitation.org/doi/abs/10.1063/1.870351>
- Yamamoto, S., & Matsuoka, T. (1996). Dynamic simulation of microstructure and rheology of fiber suspensions. *Polymer Engineering and Science*, 36(19), 2396-2403. <Go to ISI>://WOS:A1996VM13000002
- Závada, P., Schulmann, K., Racek, M., Hasalová, P., Jeřábek, P., Weinberg, R. F., et al. (2018). Role of strain localization and melt flow on exhumation of deeply subducted continental crust. *Lithosphere*, 10(2), 217-238.
- Zhao, S. W., Evans, T. M., & Zhou, X. W. (2018). Shear-induced anisotropy of granular materials with rolling resistance and particle shape effects. *International Journal of Solids and Structures*, 150, 268-281. <Go to ISI>://WOS:000444790200020

CURRICULUM VITAE

Michael Zackery McIntire

Department of Earth and Space Sciences
University of Washington,
Johnson Hall Rm 70
Box 351310, 4000 15th Ave. NE
Seattle, Wa. 98195
Phone: (206) 799-9955
Email: zackmc@uw.edu

Education

- 2021 PhD Earth and Space Science, University of Washington
Thesis advisor: George Bergantz: On the kinematic and dynamic evolution of a magma mush: from liquidus to solidus
- 2014 B.S Geosciences, Mathematics, University of Arizona
Thesis advisors: Mark Barton, Jibamitra Ganguluy; Diffusion of Fe-Mg in hydrothermal actinolite from the Santos deposit in Punta del Cobre, Chile.
Cum Laude with Honors
- 2012 A.S Arts and Science, Illinois Central College

Professional Experience

- 2015 – 2021 Teaching Assistant, Department of Earth and Space Sciences, University of Washington
- 2015 Teaching Assistant: (Geos 400) Field Camp, University of Arizona
- 2014 Preceptor: (Geos 356) Petrology, University of Arizona
- 2013 Preceptor: (Geos 302) Principles of Sedimentology and Stratigraphy, University of Arizona
- 2012 – 2015 Research Assistant: Economic Geology, Department of Geosciences, University of Arizona
- 2011 Bridging the Diversity Gap Summer Research Program for Community College Students: Iowa State University Department of Agriculture and Biosystems
Engineering Quantifying submerged aquatic vegetation in man-made wetlands using a portable echosounder.

Publications

McIntire, M.Z., Bergantz, G.W., and Schleicher, J.M., (2019). On the hydrodynamics of crystal clustering. *Philosophical Transactions of the Royal Society A: Mathematical, Physical and Engineering Sciences*, 377(2139).

McIntire, M. Z. (2014). Time Scales of a Geothermal System From Actinolite Fe-Mg Zoning.
University of Arizona Honors College

Awards / Scholarships

2019 Geological Science Unrestricted Fund Fellowship
 2018 Howard A. Coombs Endowed Fellowship in Geological Sciences
 2018 Inquisitive Graduate Student Support Fund
 2018 Richard E. Fuller Endowment Fund
 2017 Best Overall Poster ESS Research Gala
 2016 Jody Bourgeois Graduate Student Support Fund
 2016 ESS Distinguished Graduate Student Research Fellowship
 2016 Honorable Mention National Science Foundation Graduate Research Fellowship Program
 2015 Honorable Mention for Outstanding Senior in Geoscience at University of Arizona
 2015 E. V. Mayo Fellowship

2012-2014 Phi Theta Kappa Tuition Scholarship

Workshops

2017 Deep Continental Drilling into the Moho (DCD Moho) in the Ivrea-Verbano Zone, ICDP, Baveno, Lago Maggiore, Southern Alps, Italy
 2018 Evolution of Arc Crust, ExTerra, AGU Fall Meeting, Washington, District of Columbia
 2019 Cooperative Institute for Dynamic Earth Research: Volcanoes, NSF, University of California, Berkeley

Leadership and Outreach

2019 Geoclub Spring Break trip instructor
 2017-2020 ESS Curriculum Committee member
 2015-2018 University of Washington Earth and Space Sciences Rockin' Out Outreach program
 2017, 18 Science Judge National Ocean Sciences Bowl, Orca Bowl
 2017 Geological Society of America Fall 2017 Annual Meeting Student Committee Member
 2016, 17 Department of Earth and Space Sciences Research Gala Committee member
 2013-2015 Field assistant to Ph.D. Student J.D. Mizer

Professional Memberships

Geological Society of America, 2012 - present
 Society of Economic Geologists, 2013 - present
 Mineralogical Society of America, 2012 - present
 American Geophysical Union, 2015 - present

Presentations

McIntire, M. Z., Vukmanovic, Z., Bergantz, G. W., Microstructural Constraints on Tonalitic Melt Extraction from Gabbroic Mushes. Oral session at: AGU Fall Meeting: December 2019: San Francisco, California.
 McIntire, M. Z., Bergantz, G. W., Schleicher, J. M., On the hydrodynamics of crystal clustering. Poster session at: AGU Fall Meeting: December 2018: Washington, District of Columbia.
 McIntire, M. Z., Bergantz, G. W., Schleicher, J., Burgisser, A., On the Hydrogranular Dynamics

of Magmatic Gravity Currents. Poster session at: AGU Fall Meeting: December 2016: San Francisco, California.

McIntire, M. Z., Barton, M., Time Scales of a Geothermal System From Actinolite Fe-Mg Zoning. Oral session at: University of Arizona GeoDaze: March 2015: Tucson, Arizona.